Title

Energy-Optimal Motion Control and Mission Planning for Multirotor Unmanned Aerial Vehicles Based on Modeling of Integrated System Dynamics

Author

Michel, Nicolas

Publication Date

2024

Peer reviewed|Thesis/dissertation

Energy-Optimal Motion Control and Mission Planning for Multirotor Unmanned Aerial Vehicles Based on Modeling of Integrated System Dynamics

By

Nicolas Michel
Dissertation

Submitted in partial satisfaction of the requirements for the degree of

Doctor of Philosophy

in

Mechanical and Aerospace Engineering

in the

Office of Graduate Studies

of the

University of California

Davis

Approved:

Xinfan Lin, Chair

Zhaodan Kong

Seongkyu Lee

Committee in Charge

2024

Abstract

Electric multirotor aerial vehicles are an emerging technology with extensive potential applications across a wide range of fields, but flight time and range limitations currently impose significant constraints on the use of such vehicles. Improving the vehicle energy performance is therefore a critical research topic, and one promising strategy is to optimize operational energy efficiency through model-based motion planning and control. While there has been extensive research on the topic and important progress has been made, existing works generally oversimplify or disregard key vehicle subsystem behaviors, and therefore fail to capture the complete energy dynamics and exploit the full energy saving potential. To address this gap in the state of the art, a complete system-level vehicle model is developed and applied to planning and control, aiming at achieving significant energy performance improvements in this dissertation.

The model captures all relevant subsystem dynamics related to the vehicle energy performance, including propeller aerodynamics, motor assembly electro-mechanical dynamics, battery electrical dynamics, and airframe rigid-body dynamics. Through experimental validation, the model demonstrates a high degree of fidelity over a wide range of operating conditions. The model is then used to demonstrate the importance and necessity of incorporating individual dynamics into model-based planning and control, highlighting the impact of battery dynamics on the propulsion limits, the influence of propeller (inflow) aerodynamics on the energy performance, and the breakdown of vehicle energy efficiency to each subsystem dynamics. An energy-optimal trajectory generation and feedback control framework is then developed based on this model, and is shown to reduce energy usage significantly rela-

tive to a baseline controller in both simulations and experimental validation over a range of waypoint-to-waypoint flight operations. Polynomial approximations of the optimized trajectories are then developed to enable rapid and computationally efficient trajectory generation. Relative to the true energy-optimal trajectories, these approximations significantly reduce computational complexity with only a slight increase in energy consumption. Finally, the framework is extended to mission planning, in which the minimum-energy order for traversing a series of waypoints in 3D space is identified. Of particular interest is to compare with the minimum-distance order, which is often assumed to be energy optimal according to conventional wisdom and frequently adopted in practice. Over a large number of missions with randomized waypoint locations, it is found that the minimum energy order differs from the minimum-distance order in a majority of the cases, and the difference in energy consumption between the two orders can be substantial among missions of varying ranges and number of waypoints.

To my family, my friends, and my colleagues,

whose support made this work possible.

Contents

List of Figures

List of Tables

Acknowledgments

First, I wish to thank my advisor, Professor Xinfan Lin, for his outstanding guidance and support. His focus, insight, and dedication have made working with him an exceptional experience, and I am certain the lessons I've learned from his mentorship will guide me well throughout my career. I would also like to express my gratitude to Professor Zhaodan Kong and Professor Seongkyu Lee, whose contributions to my work and feedback on this dissertation have been invaluable.

I would next like to thank all of my past and present colleagues in Professor Lin's lab, including Ayush Patnaik, Yashdeep Sidana, Anish Kumar Sinha, Vincent Chung, Jamoghan Fanshal, Jackson Fogelquist, Mengzhu Gao, Russel Hawkins, Rui Huang, Sidharth Jangra, Simon Kuang, Qingzhi Lai, and Xuchang Tang. You all helped make my time at UC Davis a wonderful experience, and one I will never forget. I particularly wish to acknowledge Ayush Patnaik, Yashdeep Sidana, and Anish Kumar Sinha for their direct involvement in this work, especially regarding their vital contributions to developing the model and in performing the flight tests for this work. Similarly, I would like to thank Peng Wei, whose work developing the test vehicle, as well as his continuing guidance and assistance with our experiments, has immensely accelerated my research.

Finally, I wish to thank my parents, Paul Michel and Sylvie Morissette, on whose unending support and encouragement I have always been able to depend, and Claude Michel, my brother and best friend.

This work was supported by funding from the Office of Naval Research NEPTUNE program [award number N00014-21-1-2080].

Chapter 1

Introduction

1.1 Introduction

Multirotor aerial vehicles with electric-Vertical-Take-Off-and-Landing (eVTOL) capability are a technology with significant potential for a wide range of applications, with main advantages including superior maneuverability [1] and zero emission potential as an electrified transportation mode [2] compared with the conventional aircraft. Nowadays unmanned aerial vehicles (UAV)/drones are already seeing increasing military applications including Intelligence, Surveillance, and Reconnaissance (ISR) missions, and civilian use cases such as aerial photographing, wireless communication, and monitoring of environmental conditions [3, 4, 5]. Furthermore, they have also been envisioned as a critical part of the future logistic and transportation networks to supplement the traditional ground transportation mode [6, 7]. For example, decimeter-scale drones are under development for package delivery over air [8, 9], and larger eVTOL aircraft are being considered to enable "flying cars" for urban air mobility (UAM) [10, 11].

Despite the potential of revolutionizing the transportation and logistics networks, the UAV and UAM technologies also face critical obstacles, including a significant one in energy

performance. Currently, small scale multirotor drones are subject to major constraints on flight time (up to approximately 30 minutes for many typical models [12]) and limited payload [4]. For prospective UAM, the estimated flight time needs to be up to 1 hour with range over 70 miles. Such performance specification requires the energy system to have an energy density of 350-400Wh/kg (based on the current multirotor system efficiency), while that of the lithium ion battery technology, which is currently the predominant choice for electrical energy systems, is only around 150Wh/kg at the system level [11]. Meanwhile, high power is also required during the vertical take-off and landing periods [11]. These challenges necessitate the research on promoting the energy performance of multirotors, which can be achieved by either improving the energy source, e.g. inventing new high-energy-density battery materials, or enhancing the energy efficiency, e.g. through architecture design and optimization [13, 14], or motion planning and control [15, 16, 17]. While improvements in battery technology and vehicle design are expected to mitigate these challenges (with some projections estimating that batteries with sufficient energy densities may be available in the next decade [18]), there is a significant need to minimize energy consumption and improve energy performance through model-based planning, optimization, and control of flight operations and missions.

1.1.1 State of Art: Model-Based Multirotor Trajectory/Mission Planning and Control

Operational planning and control are widely studied topics in UAV literature [16, 19, 20]. Existing works include both model-free and model-based approaches. The former explores energy performance optimization without a physical model to maximize flight time and distance. For example, some works, such as [21, 22, 23], use extreme-seeking to find the

energy-optimal vehicle velocity and attitude based on real-time measurement of energy consumption in experimental flight. While such approaches are effective for optimizing specific flight conditions, e.g. the steady-state level flight with varying payload considered in the aforementioned works, they are not easy to extend to generic operating conditions, such as dynamic flights involving trajectories and waypoints. Therefore, in this work and the subsequent literature review, we focus on the model-based approaches, as a detailed physics-based understanding of system-level energy performance could enable parametric study of performance and design, and more importantly all levels of operation optimization from motion control, trajectory generation, to mission planning. Many relevant works address the modeling, testing, and design optimization of vehicle subsystems and components individually or as a group. For example, in [24], a UAV ESC is experimentally modeled and tested, and in [25], a similar approach is used to model and test the efficiency of the combined ESC, motor, and propeller powertrain. ESC efficiency is mapped experimentally in [26] by measuring the phase outputs over a range of input voltages and PWM settings. In [13], existing motor, battery, and propeller designs are examined to evaluate the impact of their parameters on key vehicle performance metrics, such as the vehicle's maximum loiter time. The impact of horizontal wind speed on thrust generation for an octorotor UAV is investigated in [27] using both wind tunnel testing and computational fluid dynamics, and demonstrating increased propeller thrust at low wind speeds.

1.1.1.1 Model-Based Operational Planning and Control

Building on modeling of vehicle and subsystem dynamics, many works optimize multirotor motion to enhance energy efficiency through model-based approaches which exploit some of

the underlying system dynamics [16, 28, 29]. In particular, some papers focused on planning and control considering propeller aerodynamics, which govern the thrust and torque generation for propulsion. For example, the power consumption of a UAV was modeled based on the propeller blade element momentum (BEM) theory in [30], which was then combined with optimization algorithms to generate energy-optimal two-dimensional flight trajectories to reach a destination in [31]. The same model was also used in [28] for optimizing flight plans to avoid obstacles and minimize energy consumption in a simulated two-dimensional wind field. Another model, which takes into account the inflow momentum theory and rigid body dynamics of the UAV airframe, was described in [19] and used to evaluate and compare the energy performance of a UAV in level forward flight operations under various existing control approaches, including minimum acceleration, minimum jerk, and minimum snap control. In [32], a vehicle model including dynamic propeller inflow was used to calculate minimum-time and minimum-energy trajectories for a proposed air-taxi design as it transitions between hover and cruise conditions, while also taking into account pitch angle and acoustic constraints necessary for practical UAM applications. Some other works investigated the dynamics of the motor and motor controller and exploited them for energy-efficient planning and control. In [16], a model was formulated to calculate the vehicle power consumption based on the motor and airframe rigid body dynamics, and was then applied to generate trajectories for quadrotor hover-to-hover flight operation, minimizing either the energy consumption under a fix time budget, or flight time under a fix energy budget. This model has also been used to optimize energy consumption with either free or fixed end time in [33], and calculate the minimum-energy trajectory for a hexarotor operation in [34]. Another quadrotor model which similarly considers motor and airframe dynamics was introduced and

used to generate energy-optimal trajectories in [35]. This approach was further expanded to incorporate wind effect and predict the change in battery voltage in [36] and [37]. In a similar work [3], rigid-body and motor dynamics were considered for trajectory optimization of a drone used for wireless communication, where communication performance was also included in optimization. There have also been efforts on accommodating the dynamics of the power source. For example, a UAV altitude controller has been designed in [38], which takes into account the battery state of charge (SOC). Additionally, energy-optimal paths for waypoint-to-waypoint operations were studied in [39, 40] considering vehicle rigid body and motor dynamics, and battery state-of-health.

1.1.1.2 Energy-Efficient Mission Planning

On top of trajectory and motion control, planning of complete vehicle missions (i.e., the optimal order of visiting waypoints in a mission) has also been considered as an opportunity for further improving energy performance [41, 42]. Existing research on this topic dates back to the classic Traveling Salesman Problem (TSP), which aims at minimizing the total distance of covering a series of waypoints [43, 44]. Many works have explored the problem of minimizing distance in UAV missions, often with the intuitive assumption that the energy cost is simply proportional to the distance. For example, in [42, 45, 41], the waypoint coverage plan is optimized for a single UAV with the goal of finding the shortest path. In [46, 47, 48], similar works are performed for multiple UAVs or UAV swarms. In addition, [49] and others study the optimal route planning for the joint operation of a UAV and a ground vehicle for environment coverage. Other works take energy dynamics into consideration, but typically predict energy consumption in a given operating condition based on empirical data

rather than physics-based system-level modeling. For example, a black-box approach based on empirical measurements of energy use in specific operating conditions is used in [50] to predict mission energy cost. In [51], minimum-time paths are calculated for a UAV to visit a set of waypoints. The vehicle in this work takes off from and returns to a moving ground vehicle for multiple flights, with flight duration limited by energy consumption dynamics predicted as a function of vehicle velocity. Quadrotor mission trajectories are planned in [52] using heuristic-based acceleration objectives to reduce flight time as well as a defined effort metric, which is based on thrust but does not directly capture vehicle energy dynamics. In [15, 53], energy-efficient paths are planned for a UAV to cover a defined area, with power consumption predicted based on experimental measurements. Power is specifically modeled as a function of speed in cruise, acceleration, and deceleration, with the constraint that acceleration and deceleration rates are maximized. The energy modeling and path planning approach used in these papers is further applied to irregularly-shaped areas in [54], and to spiraling trajectories in [55].

1.1.2 Gaps in Current Research

While existing works have made important contributions towards improving the multirotor energy performance, a major deficiency is that they only consider part of the governing multi-physical dynamics of the full vehicle. The complete dynamics include the subsystem dynamics of all related components, i.e. the aerodynamics of the propeller assembly, electro-mechanical dynamics of the motor and the electronic speed controller (ESC), electrical dynamics of the battery, and rigid body dynamics of the airframe, and more importantly,

their mutual impact and coupling effect on energy performance. Negligence or oversimplification of the complete dynamics would cause incorrect projection of system behavior, and lead to motion planning and control that is non-optimal in performance or even unachievable/unsafe, as to be discussed in detail in Chapter 4 of this dissertation. For example, we will show that when propeller aerodynamics are neglected, the energy-optimal velocity for steady forward flight, which is the target to control in various UAV research literature [22, 15, 23], will be significantly overestimated. Specifically, the optimum of the energy cost per meter travelled, which is a key energy efficiency index determined by four tradeoff factors involving multiple subsystem dynamics, is off by 67.8% when the propeller aerodynamics are not considered. Meanwhile, battery dynamics can significantly affect the vehicle propulsion performance [56, 57]. Specifically, the propeller thrust and torque production will decrease when the battery voltage drops due to energy depletion, and the amount can be as much as 26% over the battery operation range [58, 59] (to be discussed in details in Chapter 4). This reduction in the available thrust can reduce the vehicle operation limits (e.g., maximum velocity and acceleration), potentially making it unsafe to perform the planned maneuvers if the impact of battery dynamics is not considered in planning and control beforehand [60]. These facts demonstrate the critical need for multirotor planning and control research based on integrated full system dynamics. It is also noted that individual subsystem dynamics do not affect the vehicle performance independently, but rather through the coupling with each other. For example, the propeller inflow aerodynamics are coupled with the airframe rigid body dynamics as vehicle motion will result in relative velocity that affects inflow, while the impact of battery voltage on propulsion could only be captured through the dynamics of the motor and motor controller [59].

On the other hand, at the mission level, an open question remains to be answered - is it really true that minimum distance always means minimum energy consumption? Especially, what if the waypoints are in the more complicated 3D environment, which involves both horizontal and vertical motion? In reality, energy consumption is more complicated than just distance, as UAV motion could have major impacts on the aerodynamic efficiency of the propeller due to change in inflow [59, 61]. Therefore, different combinations of motion to cover the same set of waypoints could result in different energy consumption. There have been some works in literature aiming at minimizing the energy consumption instead of just the distance for path and/or mission planning [62, 16, 39]. However, they are subject to major oversimplications of the critical UAV energy dynamics, including assuming power consumption among hovering, horizontal, and vertical flights as equal, or a constant propeller thrust/torque and angular velocity relationship (hence neglecting the impact of motion on propeller efficiency).

1.1.3 Research Objectives

To address the gaps in the state of the art, this research work first proposes a complete system-level multirotor dynamic model, which is then applied to the development of a framework for energy-optimal trajectory generation, feedback control, and mission-planning. This work is the first to consider fully-integrated subsystem dynamics for multirotor motion planning and control, with results validated by simulation and experimental testing and interpreted by correlating to the underlying multi-physical dynamics.

The overall model captures the propeller aerodynamics, motor and electronic speed con-

troller (ESC) electro-mechanical dynamics, battery electrical dynamics, and vehicle frame rigid-body dynamics, with each subsystem parameterized using experimental data. Incorporating each of these subsystem dynamics, as well as their coupling, allows for comprehensive modeling of the complete energy performance of the vehicle. The model is used to enable detailed analysis of key system characteristics governing the energy performance, including (1) the relationship between propeller angular velocity and efficiency, (2) the relationship between vehicle cruising velocity and energy cost per meter, and (3) the effect of wind on vehicle energy efficiency in forward flight among others.

The model is then used for energy-optimal trajectory generation over a range of waypoint-to-waypoint flight operations, and a feedback control architecture is developed for real-time trajectory following. The developed planning and control framework is first tested in simulation, showing significant improvement in energy consumption over the baseline controllers commonly used for UAV control. Leveraging the model-based energy dynamics analysis, numerous features of the trajectory and maneuver are identified, which explain the substantial reduction in energy consumption achieved by the model-based optimization. Experimental validation of the developed framework is also performed using an octorotor platform under real-world operating conditions, showing similar significant energy saving over the baseline observed in simulation. Nevertheless, trajectory optimization based on the full physical model is computationally intensive and not tractable for online mission planning and flight control, which may require fast trajectory generation and re-generation. To facilitate the computation, polynomial approximations of energy-optimal trajectories were further investigated [59, 61]. The approximations are fitted and calibrated based on the optimized trajectories, and capture key energy-saving features. The simple polynomial representations

would enable efficient trajectory generation in real time with great flexibility and minimal loss of energy performance.

Finally, the optimization of UAV energy performance is extended to the mission level, with the goal of finding the optimal ordering of multiple waypoints in 3D space yielding the minimum total energy consumption. The waypoint-based mission planning problem is first formulated, where the (optimal) energy consumption between any two waypoints can be computed using the previous modeling and trajectory generation works. Optimization is then performed over a large number of missions with randomized waypoint locations. The energy consumption of the minimum-energy order is evaluated and compared with that of the minimum-distance order. Detailed analysis of two sample missions are performed to identify and explain the features of the minimum-energy order by correlating to the underlying energy dynamics, giving valuable insights on the heuristics of energy-optimal mission planning.

1.1.4 Dissertation Organization

The remainder of this dissertation is organized as follows. The system-level vehicle model is described in Chapter 2, which includes the modeling of each subsystem as well as their integration into the complete vehicle model. In Chapter 3, a method for parameterizing the model based on laboratory test bench experiments is formulated, and the parameterized model is validated in real-world flight testing. In Chapter 4, key flight behaviors and features which impact the energy performance are analyzed and discussed based on the model and test results. The model is then applied to the development of an energy-optimal trajectory generation and feedback control framework in Chapter 5, with simulation testing and

experimental validation of the energy performance compared to a baseline. To reduce the computational complexity of the framework, a set of polynomial approximations are designed in Chapter 6, which capture the features of the energy-optimal trajectories while allowing fast and efficient trajectory generation. Based on these foundational works, the waypoint-based mission planning is studied in Chapter 7. Finally, Chapter 8 gives a summary of this work, followed by references and an appendix (Chapter 9) containing supplemental equations and results.

For reference purpose, the modeling, parameterization, and validation parts of the works in Chapters 2-4 have been published in [58, 59]; the energy-optimal trajectory generation and control works in Chapter 5 have been published in [60, 63, 61]; the polynomial approximation of the energy-optimal trajectory generation in Chapter 6 has been published in [63]; and the mission planning part in Chapter 7 has been submitted and is now under review.

Chapter 2

Modeling of Integrated Multirotor System Dynamics

A system-level model is first developed in this work to properly capture the complete physical dynamics of the multirotor UAV. This model considers the dynamics of all critical subsystems, including the aerodynamics of the propeller [64], the electro-mechanical dynamics of the motor and the Electronic Speed Controller (ESC) [13, 65], electrical dynamics of the battery [66, 67], and the rigid body dynamics of the vehicle airframe [68]. This chapter first presents each of these subsystem models, and then describes their integration into the full vehicle model.

2.1 Modeling of Subsystem Dynamics

2.1.1 Propeller Aerodynamics

A model of the propeller aerodynamics is needed to calculate the forces generated for propulsion. Using the blade element momentum theory [64], this model can be established in two parts. First, to calculate the thrust T and torque Q generated by the propeller, the blade element theory is adopted using inputs including the propeller angular velocity ω, horizontal

and vertical velocities v_x and v_z (with respect to the multirotor body frame), and induced air velocity v_i. Meanwhile, the momentum theory is used to capture the propeller inflow dynamics and calculate the induced air velocity based on the (looped-back) thrust and aircraft velocities.

Fig. 2.1, shows a cross section of the propeller and defines the velocities, forces, and angles involved in the model. Specifically, the cross section is inclined at a twist angle θ relative to the propeller disk plane, which is equivalent to the element pitch angle of the blade section per design. Air flows onto the propeller section at an inflow velocity u with components u_x in the disk plane direction and u_z perpendicular to it, which define the inflow angle ϕ. This inflow generates a lift force perpendicular to the inflow and a drag force parallel to it, and these forces produce the thrust and torque perpendicular and parallel to the plane of rotation. Based on the blade element theory, for an infinitesimal segment of the propeller blade at a distance r from the motor hub (perpendicular to the cross-section plane shown in Fig. 2.1), the lift and drag forces are

$$\begin{aligned} dL &= 0.5\rho u^2 c c_l dr \\ dD &= 0.5\rho u^2 c c_d dr \\ dT &= N(dL\cos\phi - dD\sin\phi) \\ dQ &= Nr(dL\sin\phi + dD\cos\phi). \end{aligned} \tag{2.1}$$

where ρ is the air density, c is the chord length, and c_l and c_d are the lift and drag coefficients [64]. While c_d is often treated as a constant over the typical range of operation, c_l is usually modeled as proportional to the aerodynamic angle of attack α, which is the angle between

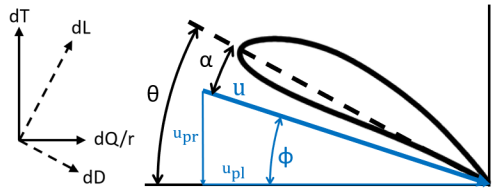

Figure 2.1: Geometries of a Blade Cross-section

the blade section zero-lift line and the inflow as shown in Fig. 2.1,

$$c_l(r) = a\alpha(r) = a(\theta(r) - \phi(r)), \tag{2.2}$$

where a is the linear coefficient. Here, the measured chord line is treated as matching the zero-lift line. Since both the twist angle θ and inflow angle ϕ vary with r, α and c_l are denoted as functions of r. The inflow angle and velocity can be computed from the planar and perpendicular inflow components as

$$\begin{aligned} u_{pl}(r,\psi) &= \omega r + v_x sin(\psi) \\ u_{pr}(r) &= v_i + v_z \\ u(r,\psi) &= \sqrt{{u_{pl}}^2 + {u_{pr}}^2} \\ \phi(r,\psi) &= tan^{-1}(u_{pr}/u_{pl}). \end{aligned} \tag{2.3}$$

Here, ω represents the angular velocity of the propeller, v_x and v_z are the planar and perpendicular airspeed components relative to the vehicle (including wind and aircraft motion), v_i is the induced velocity of the propeller disk (which will be determined by the momentum theory subsequently), and ψ represents the angular position of the blade along its rotating direction. The thrust and torque can be obtained based on dL and dD and the geometry shown in Fig. 2.1 as

$$\begin{aligned} dT(r,\psi) &= N(dL\cos\phi - dD\sin\phi) \\ dQ(r,\psi) &= Nr(dL\sin\phi + dD\cos\phi) \end{aligned} \tag{2.4}$$

where N is the number of blades in the propeller. The total thrust and torque of the blade are then computed as the integral of dT and dQ over r from the base of the blade R_0 and averaged over one rotation cycle,

$$\begin{aligned} T &= \int_{R_0}^{.97R} \int_0^{2\pi} 0.5N\rho cu(a\alpha u_{pl} - c_d u_{pr}) d\psi dr/(2\pi) \\ Q &= \int_{R_0}^{R} \int_0^{2\pi} 0.5N\rho cur(a\alpha u_{pr} + c_d u_{pl}) d\psi dr/(2\pi). \end{aligned} \tag{2.5}$$

It is noted that the element thrust is only integrated to 97% of the blade tip R to approximate the tip loss [64].

Since u_{pl} is typically much larger than u_{pr}, the small angle approximation

$$\begin{aligned} & u \approx u_{pl} \\ & \sin\phi \approx \phi \\ & \cos\phi \approx 1 \\ & \phi = tan^{-1}(u_{pr}/u_{pl}) \approx u_{pr}/u_{pl} \\ & dD\sin\phi \ll dL\cos\phi \end{aligned} \tag{2.6}$$

is often introduced to simplify the computation. Consequently, the drag component of dT in Eqn. 2.4 is also typically disregarded, as drag is generally significantly smaller than lift, and, at small ϕ, is nearly perpendicular to the direction of thrust. With these approximations, Eqn. 2.5 simplifies to

$$\begin{aligned} T &= \int_{R_0}^{.97R} \int_0^{2\pi} 0.5N\rho {u_{pl}}^2 ca(\theta - u_{pr}/u_{pl}) d\psi dr/2\pi \\ Q &= \int_{R_0}^{R} \int_0^{2\pi} 0.5Nr\rho {u_{pl}}^2 c(\phi a(\theta - u_{pr}/u_{pl}) + c_d) d\psi dr/2\pi. \end{aligned} \tag{2.7}$$

For calculating u_{pr} in Eqn. 2.3, the induced air velocity v_i needs to be obtained from the momentum theory. As shown in Fig. 2.2, air flows into the propeller air stream at point 1

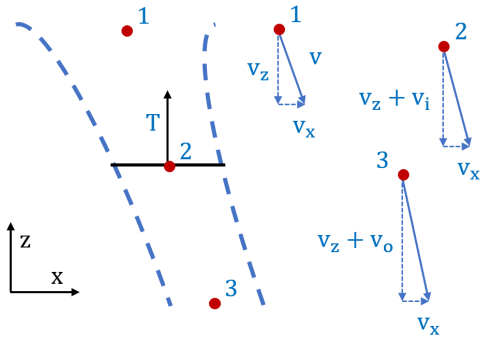

Figure 2.2: Schematic of a Propeller Flow Stream for Momentum Theory

with a relative velocity v equal to the total aircraft airspeed

$$v = \sqrt{{v_x}^2 + {v_z}^2}. \tag{2.8}$$

Note that this figure represents a propeller moving both parallel with (v_x) and perpendicular to (v_z) its plane of rotation, but is also valid for axial ($v_x = 0$), edgewise ($v_z = 0$), and hovering ($v_x = v_z = 0$) flight conditions. The air flow is then accelerated along the direction perpendicular to the propeller disk plane, giving an induced velocity v_o at the stream outlet (point 3) and v_i at the disk (point 2), which are both assumed to be uniform over the appropriate cross sections. By combining the conservation of momentum and kinetic energy, v_o is found to be twice v_i. Next, the relationship between the air mass flow rate $\dot{m}$ at the propeller, thrust T, and induced velocities can be established based on the conservation of momentum as

$$\begin{aligned} \dot{m} &= \rho\pi R^2 \sqrt{{v_x}^2 + (v_z + v_i)^2} \\ T &= \dot{m} v_o = 2\dot{m} v_i = 2\rho\pi R^2 v_i \sqrt{{v_x}^2 + (v_z + v_i)^2}. \end{aligned} \tag{2.9}$$

Rearranging Eqn. 2.9 gives

$${v_i}^4 + 2v_z {v_i}^3 + v^2 {v_i}^2 = (T/2\rho\pi R^2)^2, \tag{2.10}$$

which can then be solved to obtain v_i [64].

It should also be noted that when integrating the propeller aerodynamics to the vehicle system model, it was found based on vehicle testing data that the effect of propeller inflow modeled in this section, based on a single propeller, would be slightly overestimated. This discrepancy is likely due to the inflow interference between propellers, as well as the obstruction of air flow by the vehicle airframe. It was determined that a scaling factor can be applied to the inflow velocities to correct for these effects with sufficient accuracy. Specifically, for the octorotor considered in this work, v_x is corrected with a 80% scaling factor, while a factor of 70% is used for v_z. As described in Appendix 9.3, these values were empirically selected based on the data collected and discussed in Chapter 3.2.2, and found to compensate for a significant portion of the error between the predicted and measured thrust at varying vehicle velocities and pitch angles.

2.1.2 Motor Assembly Electro-Mechanical Dynamics

A model of the motor-ESC (electronic speed controller) subsystem is needed to capture the electro-mechanical dynamics of the rotating machinery. The ESC regulates the voltage supply to the brushless DC (BLDC) motor based on the PWM control command and the voltage supply from the battery. The BLDC motor responds with the angular velocity of the propeller ω and current I_{in} under the influence of the torque load Q. It is noted that a DC-DC power converter module could also be added to improve the quality and stability of the battery voltage supply. Such a module is not used for the considered multirotor but could be adopted for larger systems with higher payload requirement. The motor-ESC subsystem is modeled based on the circuit diagram shown in Fig. 2.3. The ESC is considered

as transmitting a certain percentage of the battery voltage V_b to the motor circuit according to the PWM command,

$$V_{in} = V_b F_{ESC\%}(PWM), \tag{2.11}$$

where $F_{ESC\%}(PWM)$ is a function relating PWM to the proportion of voltage transmitted. The BLDC motor is then modeled based on the commonly used 3-parameter model [13, 69, 70]. In this model, the three phases of the motor are modeled as one equivalent circuit, and transient effects are not considered due to the rapid response time of the motor used. The motor current I_m is determined based on the torque load Q (which is calculated in the

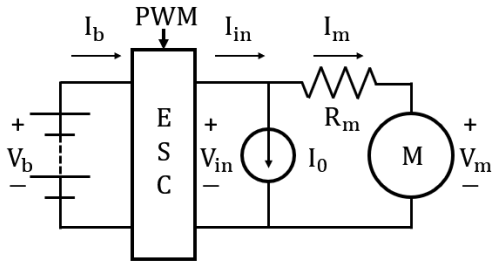

Figure 2.3: Circuit Diagram of Motor-ESC Model

propeller model) as

$$I_m = \frac{Q}{K_T} = QK_V, \tag{2.12}$$

where the motor torque constant K_T is equal to the inverse of the motor velocity constant K_V. The motor voltage (back-emf) is hence

$$V_m = V_{in} - I_m R_m \tag{2.13}$$

where R_m is the resistance of the motor (winding). Finally, the motor speed ω, which is also the angular velocity of the propeller, can be calculated as

$$\omega = V_m K_V. \tag{2.14}$$

Meanwhile, the battery current I_b is determined based on the power balance of the ESC,

$$V_b I_b \eta_{ESC} = V_{in} I_{in}, \tag{2.15}$$

which gives

$$I_b = V_{in}(I_m + I_0)/\big(V_b \eta_{ESC}\big), \tag{2.16}$$

where η_{ESC} is the ESC efficiency as a function of V_b and PWM. In this model, other motor losses, such as friction and magnetic losses, are included in the motor zero-load current I_0, which is defined as the current drawn when the torque load is zero [70].

2.1.3 Battery Electrical Dynamics

A battery model is needed to capture the evolution of battery voltage and internal states over time driven by the current (power) load. Battery voltage serves as an input to the ESC, affecting the ESC output voltage to the motor and eventually the propulsion performance including thrust, torque, and propeller speed. In this work, the battery is modeled using an equivalent circuit model (ECM) [56] as shown in Fig. 2.4, which is one of the most popular approaches for modeling macroscopic battery behavior [57].

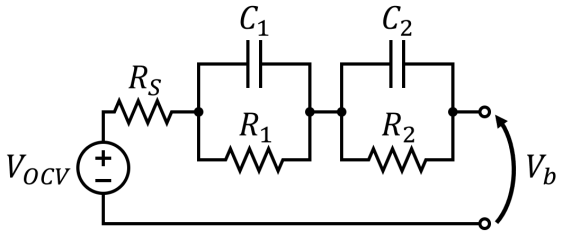

Figure 2.4: Schematic of Battery Equivalent Circuit Model

Based on the circuit diagram, the total current load of the battery, $\Sigma I_{b,j}$, which is the sum of the current drawn by each of the N_p motor ESCs (indexed by subscript $_j$), affects

the battery terminal voltage V_b according to

$$V_b = V_{OCV}(\text{SOC}) - \sum_{j=1}^{N_p} I_{b,j} R_s - \sum_{k=1}^{n} V_{RC,k}. \tag{2.17}$$

The first term on the right hand side of the equation is the open circuit voltage (OCV), which is the electrochemical equilibrium voltage of the battery under no current. The value of OCV is a function of the energy stored in the battery, which is usually measured by the state of charge (SOC). The SOC is defined as the ratio of the remaining charge (measured in Ah) in the battery and the capacity of the battery C_{bat}, and hence its dynamics can be calculated by integrating the current over time,

$$\frac{d\text{SOC}}{dt} = -\frac{1}{C_{bat}} \sum_{j=1}^{N_p} I_{b,j}. \tag{2.18}$$

It is noted that SOC is one of the most important battery internal states [57, 66], as it directly correlates to the remaining flight time/range of the electric aircraft. The second term $\Sigma I_{b,j} R_s$ accounts for the ohmic voltage drop due to the internal resistance of the battery R_s. The last term of the equation captures the transient dynamics of the battery, e.g., lithium ion diffusion and charge transfer, using equivalent resistor-capacitor (RC) pairs [67]. The voltage of each RC pair is characterized by the following equation,

$$\frac{dV_{RC,k}}{dt} = -\frac{1}{R_k C_k} V_{RC,k} + \frac{1}{C_k} \sum_{j=1}^{N_p} I_{b,j}. \tag{2.19}$$

The resistance R_k and capacitance C_k of the RC pairs often vary with SOC and temperature [56]. The optimal number of RC pairs, n, are typically determined by balancing the model fidelity and complexity. A thermal sub-model can be conveniently integrated with the equivalent circuit model to capture the battery temperature variation during operation, and the effects on battery behavior if necessary [71, 72]. The resultant electro-thermal model

could enable battery thermal management, which is expected to be of significant interest to passenger-scale eVTOL aircraft due to the high power requirement [11].

2.1.4 Airframe Rigid Body Dynamics

Finally, a model of the rigid body dynamics of the airframe is needed to predict the translational and rotational motion of the multirotor. This subsystem uses the thrusts and torques calculated by the propeller model as inputs, and in return computes the vehicle velocities, which are needed to calculate the propeller velocities as inputs of the propeller model. Two-dimensional dynamics are described here, which is adequate for simulating the vehicle in forward and vertical flight without lateral motion. Standard equations for three-dimensional dynamics are given in Appendix 9.1, and were used for the analysis of the vehicle's performance in real-world operation discussed in Chapter 3.2.2.

Using the Newton's second law, the linear and angular accelerations of the multirotor are calculated as

$$\begin{aligned} \ddot{X} &= \sum_{j=1}^{N_p} T_j sin(-\Theta)/m - C_{BD}\dot{X}|\dot{X}|/m \\ \ddot{Z} &= \sum_{j=1}^{N_p} T_j cos(\Theta)/m - g \\ \ddot{\Theta} &= \tau_\Theta / J_\Theta = \sum_{j=1}^{N_p} L_{\Theta,j} T_j / J_\Theta \end{aligned} \tag{2.20}$$

which are then solved over time to obtain the velocity, position, and orientation of the UAV. Specifically, X and Z are the horizontal and vertical positions of the vehicle center of mass in the global frame, and Θ is the vehicle pitch angle. In addition, ΣT_j is the sum of thrusts of all propellers computed by the propeller model (with each propeller indexed by subscript $_j$, and total number of propellers N_p), $C_{BD}\dot{X}|\dot{X}|$ is the body drag force with C_{BD} as the body

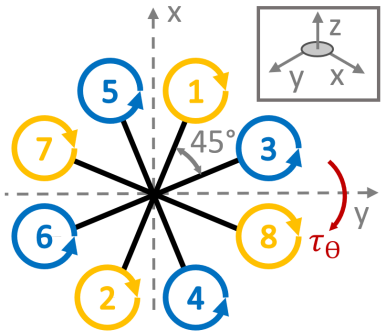

Figure 2.5: Layout of Propellers, Axes, and Torques (Inset: Axis Orientations)

drag coefficient, J_Θ is the moment of inertia about the pitch axis, τ_Θ is the total pitch-axis torque on the multirotor, and $L_{\Theta,j}$ is the arm length of each propeller thrust to the pitch axis. Notably, as the body drag is proportional to the velocity squared and the forward velocity tends to be significantly larger than the vertical velocity, vertical drag is not considered. The inflow velocities can then be calculated for each propeller as

$$\begin{aligned} v_{x,j} =& \dot{X}\cos\Theta + \dot{Z}\sin\Theta \\ v_{z,j} =& -\dot{X}\sin\Theta + \dot{Z}\cos\Theta + \dot{\Theta}x_j \end{aligned} \tag{2.21}$$

where x_j is the x position of the propeller relative to the vehicle center of mass.

The configuration of the specific multirotor airframe used in this work is shown in Fig. 2.5, which includes propeller numbering and positions. For this octorotor ($N_p = 8$) vehicle configuration, τ_Θ can be calculated based on the thrust of each propeller (for an octorotor) as

$$\tau_\Theta = L_{arm}((T_5 + T_1 - T_2 - T_4)\cos(\pi/8) + (T_7 + T_3 - T_6 - T_8)\sin(\pi/8)). \tag{2.22}$$

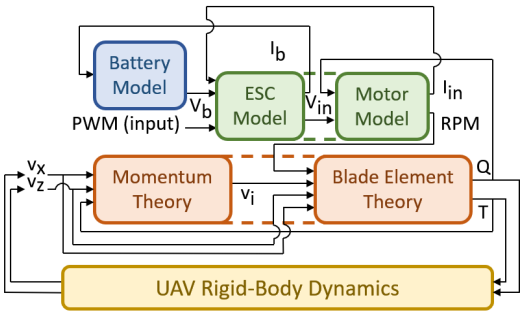

Figure 2.6: Block Diagram of Integrated System Model

2.2 Integration of System-level Model

With the dynamics of each subsystem defined, the overall system-level model can be integrated as shown in Fig. 2.6. The control inputs are the PWM commands for each motor, which instruct each ESC to regulate the corresponding motor's input voltage as a fraction of the battery voltage. The motor responds with a current draw and a rotational speed, which also depends on the torque load from the propeller. The motor rotation drives the propeller to generate the thrust and torque per blade element theory. Thrust and torque are then used in the rigid body dynamics model to calculate the motion of the UAV, which affects the horizontal and vertical velocities of each propeller for both blade element and momentum theories. The torque is looped back to the motor to determine the motor speed and current, which is further looped back to ESC to determine the current drawn from the battery. Finally, the voltage output by the battery varies in response to the total current load, which influences the voltage output from each ESC to the corresponding motor, completing the loop of coupled dynamics. It should also be noted that this model can be easily augmented by modifying or expanding individual subsystem models. For instance, as noted in Chapter 2.1.3, the battery model could be augmented to further incorporate thermal dynamics. Such modifications would not require changes to the other subsystems, and could enable future

work on battery thermal management, which is more relevant and significant for applications such as passenger-scale eVTOL vehicle [11].

Chapter 3

Model Parameterization and Validation

This chapter discusses the methodology and experimental results for parameterization and validation of the vehicle model. Each of the subsystems is parameterized individually, while laboratory test bench data is used to validate the combined ESC, motor, and propeller models, and vehicle test flights are used to validate the complete integrated model.

3.1 Model Parameterization

In this section, the processes used to parameterize the propeller, motor and ESC, and battery subsystem models are described. Most of the identified parameters are listed in Table 3.1, while the ones that are state-dependent and subject to variation, e.g. the ESC $F_{ESC\%}$ and η_{ESC}, and battery R_s, R_i, and C_i, are described in the corresponding subsections. The results are given in this section for the specific octorotor used as a test vehicle, which is described in more detail in Chapter 3.2.2. Without loss of generality, the same methodology can be applied to other multirotor designs and components.

Parameter	Value	Unit
$c(r)$	$0.056 - 0.23r$	m
$\theta(r)$	$0.42 - 1.7r$	rad
R_0	0.051	m
R	0.19	m
a	7.12	rad^{-1}
c_d	0.0334	
R_m	0.10	Ω
I_0	1.19	A
K_v	406.5	RPM/V
C_{bat}	15.66	Ah

Table 3.1: Identified Propeller, Motor, and Battery Parameters

3.1.1 Propeller Model

For the propeller model discussed in Chapter 2.1.1, the parameters that need to be determined can be categorized as geometric parameters and aerodynamic parameters. The geometric parameters include the chord length c, the blade twist angle θ, and the blade base and tip positions R_0 and R shown in Fig. 3.1, which are directly measured and listed in Table. 3.1. The aerodynamic parameters, which are used to resolve the equations for blade

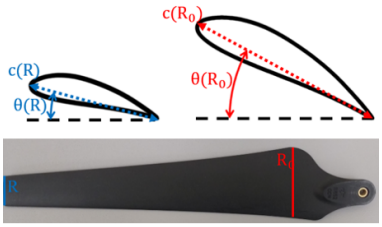

Figure 3.1: Blade Geometries

element theory, include the lift (slope) coefficient a and drag coefficient c_d, which need to be determined by system identification based on experiment data. The basic idea is to fit for the coefficients so that the model prediction could match the thrust and torque data measured from experiments. An RCbenchmark 1580 dynamometer, shown in Fig. 3.2, which can measure the motor/propeller angular velocity (RPM) with an optical sensor and the propeller torque and thrust with load cells [73], is used for testing in this work. One set of ESC, motor, and propeller assembly of the multirotor is mounted in the vertical orientation, as shown in Fig. 3.2. Because the dynamometer is stationary, the propeller operates as if under the hovering condition. Under such circumstance, the thrust and torque at each blade element remain constant as the propeller rotates, and the integration over the rotational angle in Eqn. 2.7 can be easily performed to compute the total thrust and torque measured by the dynamometer. The equations can then be rearranged to calculate or fit for a and c_d using the measurement data. In such setup, we have airspeed $v = v_x = v_z = 0$, and hence

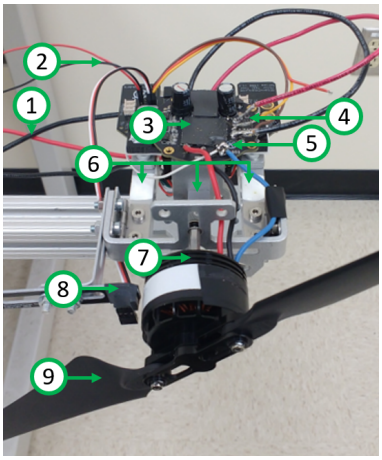

Figure 3.2: Dynamometer used for propeller, motor, and ESC testing. Labels: (1) DC voltage supply, (2) optical RPM probe 5V input, (3) ESC, (4) ESC power and PWM input, (5) motor power input, (6) load cells, (7) motor, (8) optical RPM probe, and (9) propeller

the u_{pr} and u_{pl} in Eqn. 2.3 and the induced velocity v_i in Eqn. 2.10 are reduced to

$$u_{pr,h} = v_{i,h} = \sqrt{T/(2\rho\pi R^2)}, \quad u_{pl,h} = \omega r. \tag{3.1}$$

As a result, the thrust equation in (2.7) can be simplified to

$$T = \rho a(\omega^2 \int_{R_0}^{0.97R} cr^2\theta dr - \omega\sqrt{T} \int_{R_0}^{0.97R} \sqrt{1/(2\rho\pi R^2)} cr dr), \tag{3.2}$$

which can be rearranged to calculate a from T and ω as

$$\begin{aligned} a &= (C_1\frac{\omega^2}{T} + C_2\sqrt{\frac{\omega^2}{T}})^{-1} \\ C_1 &= \int_{R_0}^{0.97R} \rho cr^2\theta dr, \quad C_2 = -\int_{R_0}^{0.97R} \frac{\rho^{0.5} cr}{2^{0.5}\pi^{0.5}R} dr. \end{aligned} \tag{3.3}$$

Similarly, the torque equation in (2.7) can be simplified to

$$Q = a\int_{R_0}^{R} (c\theta r^2\sqrt{\rho/(2\pi R^2)} \cdot \omega\sqrt{T} - (cr/(2\pi R^2)) \cdot T) dr + c_d \int_{R_0}^{R} \rho cr^3 dr\omega^2. \tag{3.4}$$

Rearranging Eqn. 3.4 gives the equation for calculating c_d,

$$\begin{aligned} c_d &= \frac{1}{C_5}\frac{Q}{\omega^2} + \frac{C_3}{C_5}\frac{T}{\omega^2} + \frac{C_4}{C_5}\sqrt{\frac{T}{\omega^2}} \\ C_3 &= \int_{R_0}^{R} \frac{acr}{2\pi R^2} dr, \quad C_4 = -\int_{R_0}^{R} \frac{a\rho^{0.5} c\theta r^2}{2^{0.5}\pi^{0.5}R} dr, \quad C_5 = \int_{R_0}^{R} \rho cr^3 dr. \end{aligned} \tag{3.5}$$

The dynamometer is used to generate the thrust, torque, and propeller angular velocity data under a series of PWM commands and input voltage V_b, which are then used to fit for the lift and drag parameters. As shown in Fig. 3.3, the obtained two coefficients are fairly constant over the PWM range, with average values of 7.12 rad^{-1} for a and 0.0334 for c_d, and standard deviations of 0.13 rad^{-1} and 0.0015 respectively. Based on the consistency of these results, it can be concluded that the assumptions made to simplify the equations above are valid, and the coefficients a and c_d are appropriately modeled as constants, particularly with respect to the propeller angular velocity.

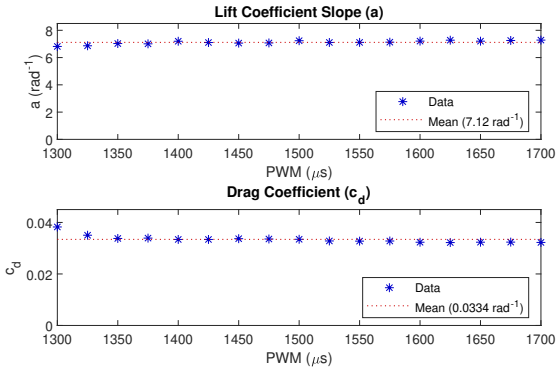

Figure 3.3: Identified Values of a and c_d under Different PWM Inputs

3.1.2 Motor and ESC Model

The motor parameters that need to be identified include the motor resistance R_m, motor zero-load current I_0, and motor constant K_v, and the ESC parameters are the voltage transmitting ratio function $F_{ESC\%}(PWM)$ and the efficiency η_{ESC}. The motor resistance R_m is measured as half of the phase-to-phase resistance of the motor at 0.10 Ω. The motor constant, $K_v = \omega/V_m$, can be obtained from the motor voltage and speed measurement. When no propeller is attached, the motor torque (and therefore current) is close to zero, giving $V_m = V_{in}$ according to Eqn. 2.13. If the PWM is set to maximum, the full input DC voltage will be transmitted to the motor, yielding $V_{in} = V_b = V_m$. In the test bench, the battery voltage V_b is emulated by an adjustable constant voltage source. The V_b and ω measured under this condition are then used to calculate the value of $K_v = 406.5\ RPM/V$. This value is very close to the nominal value of 400 RPM/V given by the manufacturer. The data collected with no propeller attached is also used to determine I_0, under the assumption that the current output from ESC is equal to the input current at full PWM (or close to 100% ESC efficiency at full PWM as reported in [69, 26]). Under this condition, the zero-load current can be found as

$$I_0 = I_b - QK_v. \tag{3.6}$$

Over the range of voltage tested, the value was found to be approximately constant at $I_0 = 1.19\ A$.

With known motor parameters, the ESC voltage ratio function $F_{ESC\%}(PWM)$ can be determined accordingly. Using the torque and propeller angular velocity data generated by the dynamometer, the motor circuit input voltage V_{in} can be computed under each pair of known PWM and V_b as

$$V_{in} = V_m + I_m R_m = \omega / K_v + Q K_v R_m, \tag{3.7}$$

and $F_{ESC\%}(PWM)$ can then be determined as

$$F_{ESC\%}(PWM) = V_{in}/V_b. \tag{3.8}$$

The obtained $F_{ESC\%}$ is plotted in Fig. 3.4 (a), showing a nonlinear relation with PWM that is approximately invariant under different V_b.

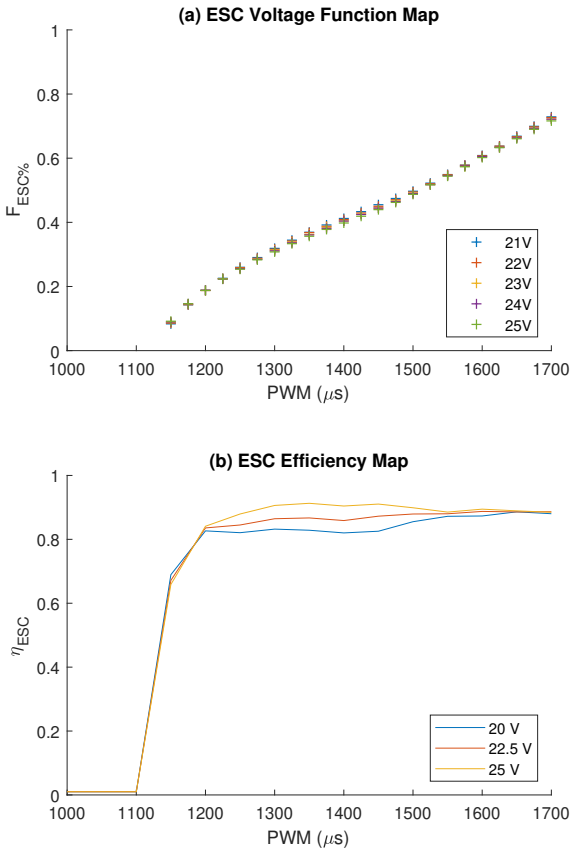

Figure 3.4: Identification of ESC Parameters: (a) Identified ESC Voltage Function and (b) ESC Efficiency Map

Finally, the ESC efficiency η_{ESC} can be computed under different PWM and V_b as

$$\begin{aligned} \eta_{ESC}(V_b, PWM) &= V_{in} I_{in} / V_b I_b \\ &= F_{ESC}(PWM)(QK_v + I_0)/I_b, \end{aligned} \tag{3.9}$$

where the DC input current I_b is measured on the test bench. The obtained η_{ESC} map is presented in Fig. 3.4 (b), showing significant variation, i.e. 82% to 91%, over the operating range of PWM and input voltage. These results are generally in agreement with those found in literature for comparable ESC hardware [26], [24].

3.1.3 Battery Model

Battery parameters that need to be identified include the open circuit voltage (OCV) as a function of SOC, battery capacity C_{bat}, series resistance R_s, and R_i and C_i of the RC pairs. The methodology developed in [56] is adopted to perform the parameter identification. The battery considered is a Tattu Lithium Cobalt Oxide Polymer battery pack with a nominal capacity of 16 Ah consisting of 6 cells in series. The focus here is to parameterize a single cell with a nominal voltage of 3.7 V, which can be scaled up to represent the whole pack. The maximum continuous discharge rate of the battery is 15 C, where C-rate is defined as the ratio between the current and the battery capacity i.e. $1C = 16A$. An Arbin LBT 21084 battery cycler with single channel specifications of 10 V and 30 A (max) is used for testing.

To identify the OCV and C_{bat}, the battery cell is discharged with a low constant current rate (C/10), under which the measured terminal voltage is close to V_{OCV}. The results are shown in Fig. 3.5 (a), where the x-axis denotes the charge throughput in Ah, which is the integration of the discharge current over time. The battery capacity is measured as the amount of charge between 3.5 V and 4.2 V, which is found to be 15.67 Ah. This value is slightly lower (-2.1%) than the nominal value given by the manufacturer. A number of possible causes, including manufacturer variability and battery degradation, could contribute to this discrepancy. The $V_{OCV}(SOC)$ function can then be obtained by normalizing the x-axis of the OCV curve in Fig. 3.5 (a) with the capacity.

For the remaining parameters, a series of pulse tests have been conducted for identification as shown in Fig. 3.5 (b). The battery was first charged to 100% SOC under 1 C current using the Constant Current-Constant Voltage (CC-CV) protocol, and relaxed under zero

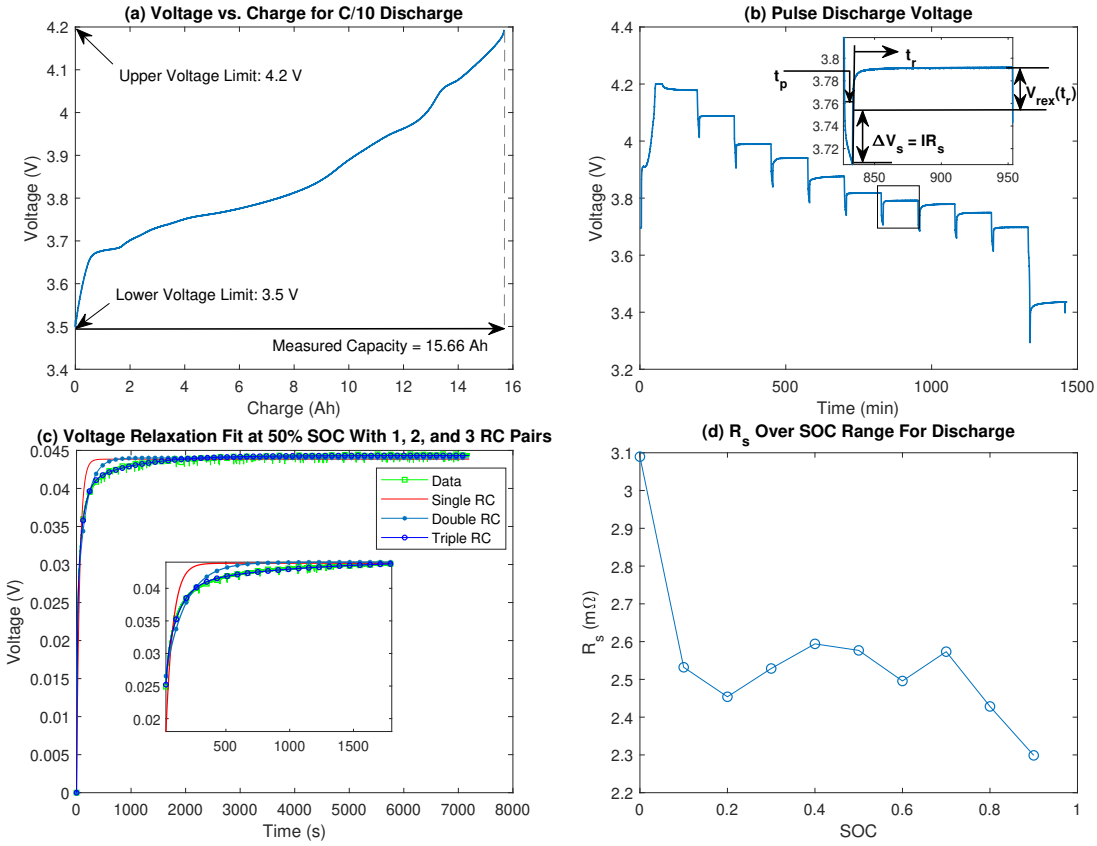

Figure 3.5: Identification of Battery Parameters: (a) Battery Voltage versus Charge Measured Under C/10 Constant Current for Identifying Capacity and OCV, (b) Voltage Profile During Pulse Discharge Test for Identifying R_s, R_i, and C_i, (c) Comparison of Fitted V_{rex} with 1, 2 and 3 RC Pairs, (d) Identified R_s versus SOC

current for 2 hours to reach voltage equilibrium. It was then discharged to 90% SOC using 1 C current, after which the current was cutoff for 2 hours. This process was repeated until the battery reached 0% SOC. The obtained voltage data are used to identify the series resistance and the RC circuit parameters at the respective SOC. Specifically, the series resistance R_s is correlated with the instantaneous voltage jump after the current cutoff, and can be calculated as

$$R_s = \frac{\Delta V_s}{I}, \tag{3.10}$$

where I is the current applied during the pulse. It is noted that the R_s identified here is

the ohmic resistance of a single cell. When scaling up to the battery module consisting of multiple cells connected in series, the total resistance needs to be adjusted to include the wiring/connection resistance and potential variability among cells based on module testing data. For example, for the UAV testing data shown in Fig. 3.8, an additional 17.6 $m\Omega$ is added to account for the extra resistance of the battery pack. The voltage profile V_{rex} during the ensuing relaxation period t_r (shown in the inset of Fig. 3.5 (b)) is dictated by the dynamics of RC pair and are hence used to identify R_i and C_i. Specifically, V_{rex} can be solved based on Eqn. 2.19 as [56],

$$V_{rex}(t_r) = \sum_{i=1}^{n} IR_i(1 - e^{-t_p/(R_iC_i)})(1 - e^{-t_r/(R_iC_i)}) \tag{3.11}$$

where t_p is the pulse duration preceding the current cutoff. The values of R_i and C_i are then fitted to minimize the sum of square errors between the model prediction and the measurement data over the discrete time instant k's,

$$J = min_{R_i,C_i} \sum_{k} (V_{rex}(k) - V_{rex,data}(k))^2. \tag{3.12}$$

To determine the optimal number of RC pairs n, V_{rex} fitting has been performed with $n = 1$, 2 and 3 as shown in Fig. 3.5 (c) (at 50% SOC). It was found that for this battery, 3 RC pairs yield acceptable accuracy. The identified series resistance R_s at various SOCs are shown in Fig. 3.5 (d), and the results for other parameters are shown in Appendix 9.2 as Fig. 9.1.

3.2 Experimental Validation of Model

In this section, in order to evaluate the model fidelity under various operating conditions, the developed multirotor system model is validated using both the dynamometer and a retrofitted UAV platform.

3.2.1 Validation on Dynamometer

By using the aforementioned dynamometer shown in Fig. 3.2, a major portion of the system model, including the coupled motor, ESC, and propeller dynamics, can be validated under the ideal hovering condition for a single propeller. Specifically, the PWM command and battery voltage V_b (emulated by a voltage source) are varied over the normal operation range to measure the resultant thrust, torque, and propeller/motor angular velocity. The tolerances of measurement are 0.5%±0.05 N for thrust and 0.5%±0.005 Nm for torque, according to the manufacturer datasheet. The results are compared against the values predicted by our model, as shown in Fig. 3.6. It is seen that the model matches the experimental results with high accuracy over the complete range of PWM settings and input voltage tested, with statistics given in table 3.2. The relationship between motor speed and PWM is modelled properly, which appears to be composed of two piece-wise linear segments. Meanwhile, thrust and torque show more prominent nonlinear dependency since they are proportional to the square of the propeller angular velocity as shown in our previous derivation. Furthermore, all three quantities decrease significantly at low battery voltage, which will be analyzed in detail in Chapter 4.1.

Error	Thrust (N)	Torque (mNm)	Angular Velocity (RPM)
Maximum	0.57 (6.4%)	8.8 (8.6%)	71 (1.9%)
Mean	0.075 (0.29%)	1.6 (1.2%)	-4.8 (-0.080%)
RMS	0.20 (2.4%)	3.9 (2.8%)	30 (0.80%)

Table 3.2: Maximum, Mean, and RMS Errors of Propeller Thrust, Torque, and Angular Velocity in Test Bench Validation

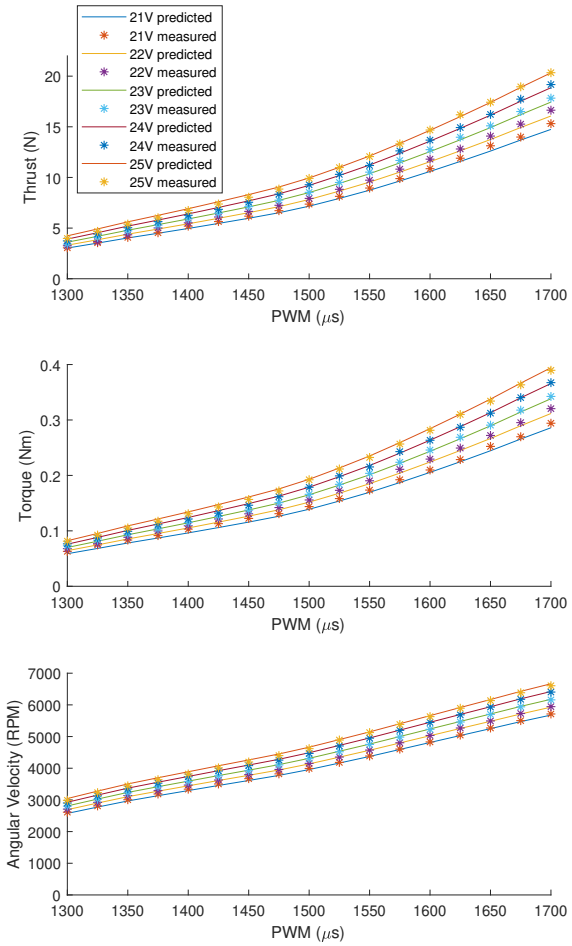

Figure 3.6: Comparison of Measured and Predicted T, Q, and ω using Dynamometer Data

3.2.2 Validation on Octorotor UAV Platform

In order to validate the complete system dynamics under actual flight conditions, a test vehicle, shown in Fig. 3.7, has been built by using the airframe and propulsion system (including propellers, motors, and ESC) of a DJI Spreading Wings S1000+ octorotor, and retrofitting the control and sensing systems with a Pixhawk 2.1 Flight Controller, a Piksi Multi GNSS receiver, a 3DR uBlox GPS with compass, a battery current transducer, and a voltage sensor. These components and the vehicle's physical parameters are listed in table

3.3.

Vehicle Components:	
Airframe	DJI Spreading Wings S1000+ (Incl. Propellers, Motors, and ESCs)
Battery	Tattu Lipo (22.2V, 6S, 16000 mAh)
GNSS Receiver	Piksi Multi
GPS	3DR UBlox
Vehicle Parameters:	
m	7.6 kg (incl. battery)
L_{arm}	0.5225 m
C_{BD}	0.16
J_{Φ}	0.4 kg m^2
J_{Θ}	0.4 kg m^2
J_{Ψ}	0.6 kg m^2

Table 3.3: List of Vehicle Components and Parameters

With this setup, the multirotor can be controlled to perform different flight maneuvers and operations with data measured and recorded for model validation. Specifically, the measured aircraft velocity, attitude, and angular velocity are used to compute the airspeed v_x and v_z, which along with the PWM commands constitute the inputs to the system model. The focus of vehicle testing is to validate the model prediction of system-level propulsion and energy performance, and hence the variables to be validated include the total thrust, which is derived from the measured aircraft acceleration and attitude, and battery current

Figure 3.7: Left: Octorotor Testing Vehicle; Right: UAV Testing at Woodland-Davis Aeromodelers Test Site

and voltage, which combine to give the system power consumption. The measured thrust is obtained from the measurement data by balancing the forces along the vehicle body z axis as

$$T_{meas} = mgcos(\Phi)cos(\Theta) - ma_z \tag{3.13}$$

where Φ and Θ are the measured Euler roll and pitch angles, and a_z is the measured acceleration along the body z direction. To identify the body drag coefficient C_{BD}, a similar force balance along the direction of motion in level forward flight gives

$$C_{BD} = (T_{meas}sin(-\Theta) - m\ddot{X})/(\dot{X}|\dot{X}|). \tag{3.14}$$

Based on test flight results, a value of 0.16 for C_{BD} was found to accurately match measured behavior over a range of forward velocities and accelerations. Regarding the measurement accuracy, according to the manufacturer datasheet, the current transducer has an error of $\pm 0.70\%$. The primary measurement error for the voltage comes from the voltage divider, which has a tolerance of 0.1%. The accelerometer has a listed RMS noise of 8 mg, which translates to a contribution of 0.6 N of noise to the thrust measurement error based on Eqn. 3.13. The measurement accuracy is adequate for experimental validation. The predicted thrust, current, and voltage are obtained from the integrated model, calculated at each time interval using the recorded PWM inputs and vehicle airspeed v_x and v_z derived from onboard

measurements of vehicle attitude and velocity. The model predicted thrust is the sum of the thrust of all propellers, which may differ from each other due to different PWM commands. The predicted current is obtained as the total current drawn by all ESCs, which feeds to the battery model to compute the single cell voltage, and the predicted total battery voltage is obtained as the single cell voltage multiplied by the number of cells.

Two sets of data are demonstrated for experimental validation. The first set includes a full flight from takeoff to landing as shown in Fig. 3.8. According to the model, the battery state of charge depletes from 83.5% to 28.8% over this duration, as plotted in Fig. 3.8 (c). The predicted voltage matches the measured voltage well over the flight duration as indicated by Fig. 3.8 (a), with an error mean of 0.02 V and standard deviation of 0.18 V, out of the total voltage range between 20.0 V and 24.2 V. This flight includes rapid maneuvers with relatively high vehicle pitch and roll angles, causing large and significantly varying power demand. Consequently, Fig. 3.8 (b) illustrates the highly variable discharge rates that occur in such maneuvers, with a measured current rate averaging 2.51 C, and peaking at 3.39 C during takeoff and 4.69 C over the flight. It is seen that the model predicts the current accurately, with an error mean of 0.06 C and standard deviation of 0.22 C, out of the total current range between 0 and 4.69 C. Noted that the current C rates in this section are calculated as the battery current I_b (in A) divided by the measured battery capacity (15.67 Ah) identified in Chapter 3.1.3 and used in the model.

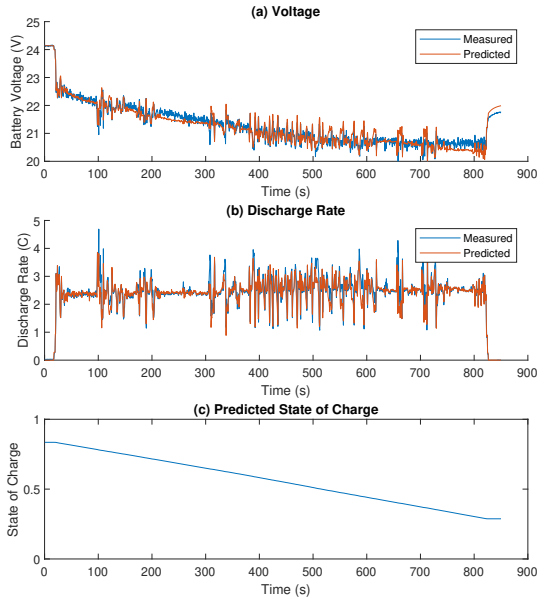

Figure 3.8: Experimental Validation of Model Over a Full Flight with Battery SOC variation from 83.5% to 28.8%: (a) Voltage, (b) Discharge Current Rate, and (c) State of Charge

To better examine the performance of the model under a range of typical operating conditions, a second set of data is presented in Fig. 3.9. This flight consists of clearly separated segments of typical operations, enabling the analysis of the performance of the model and the vehicle under different operating conditions in detail. Specifically, three segments of hovering, vertical, and horizontal flight are marked in Fig 3.9 (a) respectively and discussed in this section. The battery depletes from 95.5% to 54.0% SOC in this flight, and both the voltage and current predictions match well over the duration, with an error mean of 0.11 V and a standard deviation of 0.15 V for voltage (out of the total range between 21.5 V and 24.8 V), and an error mean of -0.009 C and a standard deviation of 0.039 C for current (out of the total range between 0 C and 3.00 C). It can be observed that the predicted voltage is slightly higher than the measured voltage early in the flight (during vertical and horizontal flight), but decreases slightly faster, and becomes lower than the measured value

during later part of the flight (e.g. hovering). One possible explanation for this discrepancy is that the capacity value used in the battery model may be slightly lower than the capacity of the actual battery used in this flight, causing the predicted voltage to drop more rapidly than the measured voltage. As the model parameterization data was obtained by testing a single cell, some variation in the results is expected due to manufacturing variability and varying levels of degradation between units. Finally, the thrust prediction for this flight, shown in Fig. 3.9 (d), also matches the measured results accurately, with an error mean of 2.0 N and a standard deviation of 2.4 N, out of the thrust range between 0 N and 87.7 N. It should also be noted that the current and power demand (with respect to the battery size) is consistent with that of the passenger-scale eVTOL aircraft, which is expected to have similar maximum current upwards of 3 C under certain operating conditions [11]. Therefore, the model developed in this work and the UAV platform could potentially be used for preliminary research on eVTOL aircraft design and control.

The second set of data is further analyzed in terms of the three flight segments. Fig. 3.10 shows the validation of battery voltage, battery discharge current rate, battery electrical power, and total thrust under the hovering condition. It is seen that the model prediction matches very well with the experiment measurement. Specifically, the current error has a mean of 0.011 C (0.41%) and a standard deviation (SD) of 0.018 C (0.66%); those of the voltage error are 0.13 V (0.56%) and 0.08 V (0.33%); and those of the thrust error are 1.71 N (2.27%) and 1.87 N (2.50%). All error statistics are summarized in Table 3.4. Although all errors are generally low, the thrust prediction is the least accurate compared with that of current and voltage. Higher thrust error is partially due to accelerometer noise, but also caused by disturbances, particularly wind. Specifically, the predicted thrust is

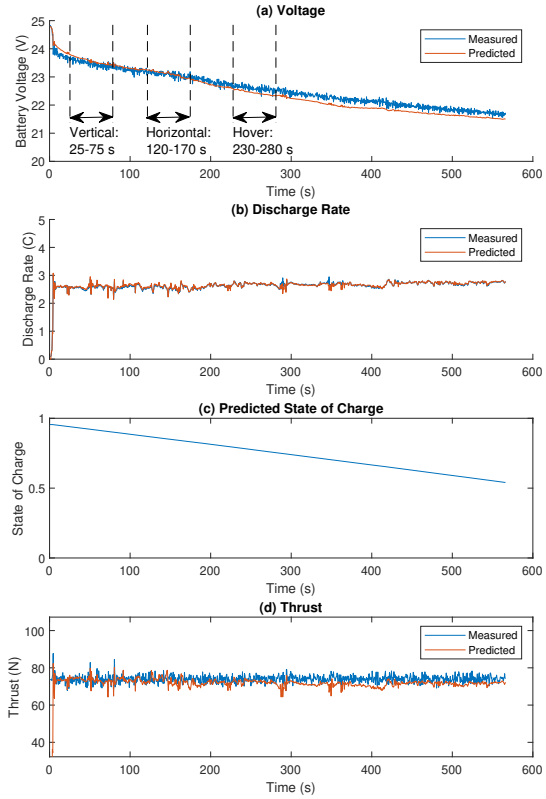

Figure 3.9: Experimental Validation of Model Over a Full Flight with Battery SOC variation from 95.5% to 54.0%: (a) Voltage, (b) Discharge Current Rate, (c) State of Charge, and (d) Thrust

computed based on the model without considering the wind, i.e. the airspeeds v_x and v_z fed to the propeller model only consider vehicle motion, but not the potential wind contribution. As described in Eqn. 2.3, these airspeed terms dictate the angle of attack α of each blade element, and therefore influence the lift coefficient c_l. The thrust and lift vectors are typically closely aligned, meaning such changes in c_l can significantly affect thrust in sufficiently strong wind. The current and voltage predictions, on the other hand, do capture the wind effect indirectly. During the flight, the vehicle on-board controller would adjust PWM commands to maintain steady thrust in the presence of wind disturbances. Therefore, by using PWM

as the inputs for current and voltage prediction, the effect of wind is implicitly included to a certain degree. Notably, the current drawn from the battery is primarily dictated by the mechanical power required for each motor to counter the propeller drag. Unlike c_l, the drag coefficient c_d is constant, so the current drawn can be more accurately predicted than thrust using only the battery voltage and the PWM command without precise values for v_x and v_z. A gradual decline in battery voltage is also observed due to the consumption of battery energy.

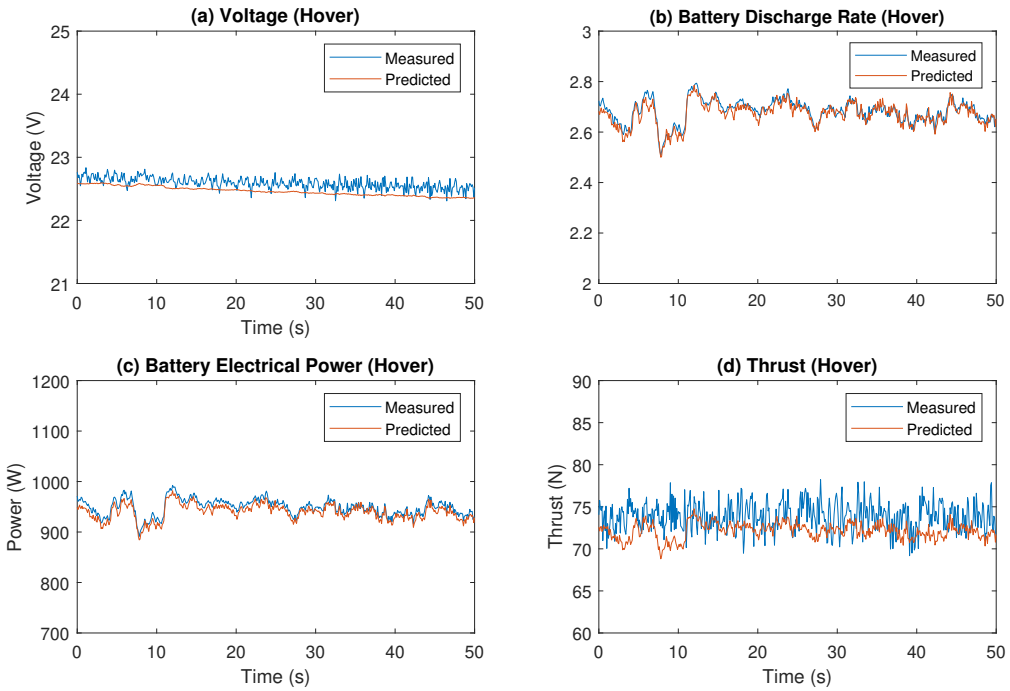

Figure 3.10: Experimental Validation of Model during Hovering: (a) Voltage, (b) Battery Discharge Rate, (c) Battery Electrical Power, and (d) Thrust

During vertical flight, the aircraft is subject to the velocity profile shown in Fig. 3.11 (a), which primarily consists of a slow descent followed by a more rapid climb. The validation results for battery voltage, battery discharge rate, battery electrical power, and thrust are also included in the figure to demonstrate the good model fidelity. Specifically, for discharge

	Discharge Rate (C)		Voltage (V)		Thrust (N)	
Error	Mean	SD	Mean	SD	Mean	SD
Hover	0.011 (0.41%)	0.018 (0.66%)	0.13 (0.56%)	0.08 (0.33%)	1.71 (2.27%)	1.87 (2.50%)
Vertical	0.021 (0.82%)	0.022 (0.89%)	-0.12 (-0.50%)	0.08 (0.32%)	2.16 (2.9%)	2.13 (2.82%)
Horizontal	0.016 (0.61%)	0.036 (1.34%)	-0.07 (-0.29%)	0.08 (0.36%)	2.78 (3.7%)	2.32 (3.07%)

Table 3.4: Error Means and Standard Deviations of Current, Voltage, and Thrust Prediction in Vehicle Testing of Each Flight Mode

rate prediction, the error has a mean of 0.021 C (0.82%) and a standard deviation of 0.022 C (0.89%); for voltage, the mean and SD are -0.12 V (-0.50%) and 0.08 V (0.32%); and for thrust, those are 2.16 N (2.9%) and 2.13 N (2.82%). It is also noted that the model not only predicts the aircraft behavior well during the steady descent and climb period, but also captures the instantaneous spikes in thrust and current at acceleration/deceleration, indicating good fidelity during transient as well.

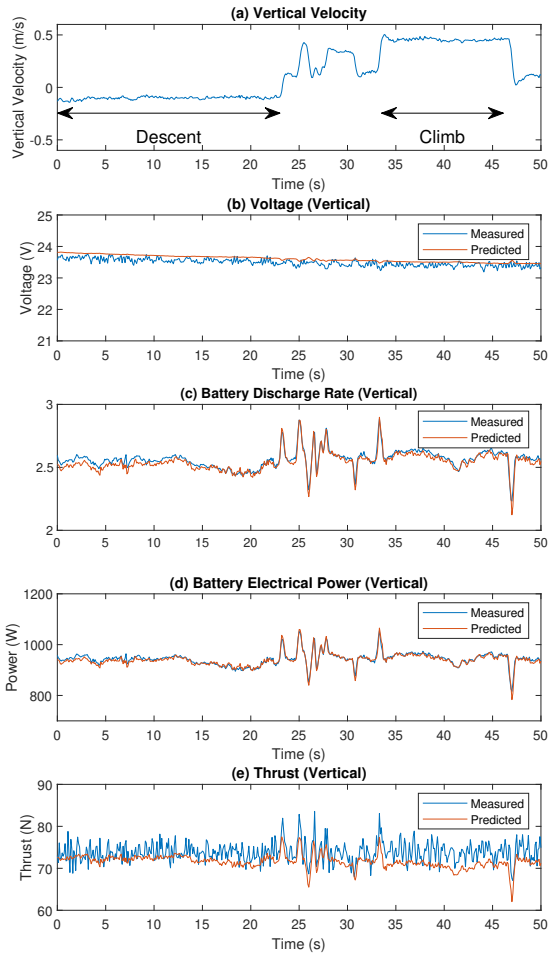

Figure 3.11: Experimental Validation of Model during Vertical Flight: (a) Velocity, (b) Voltage, (c) Battery Discharge Rate, (d) Battery Electrical Power, and (e) Thrust

During horizontal flight, the multirotor velocity profile is shown in Fig. 3.12 (a), which covers a range of velocity variation and includes various acceleration and deceleration segments, along with validation of battery voltage, battery discharge rate, battery electrical power, and total thrust presented in the rest of the figure. For current prediction, the error has a mean of 0.016 C (0.61%) and a standard deviation of 0.036 C (1.34%); for voltage, the mean and SD are -0.07 V (-0.29%) and 0.08 V (0.36%); and for thrust, those are 2.78

N (3.7%) and 2.32 N (3.07%). It is seen that the model still performs well in predicting all key system variables, while the accuracy degrades minimally compared to the hovering and vertical flights. This is primarily because of the disruptions to the propeller inflow and flow interference among propellers due to forward motion, which could make the momentum theory less accurate for horizontal flight.

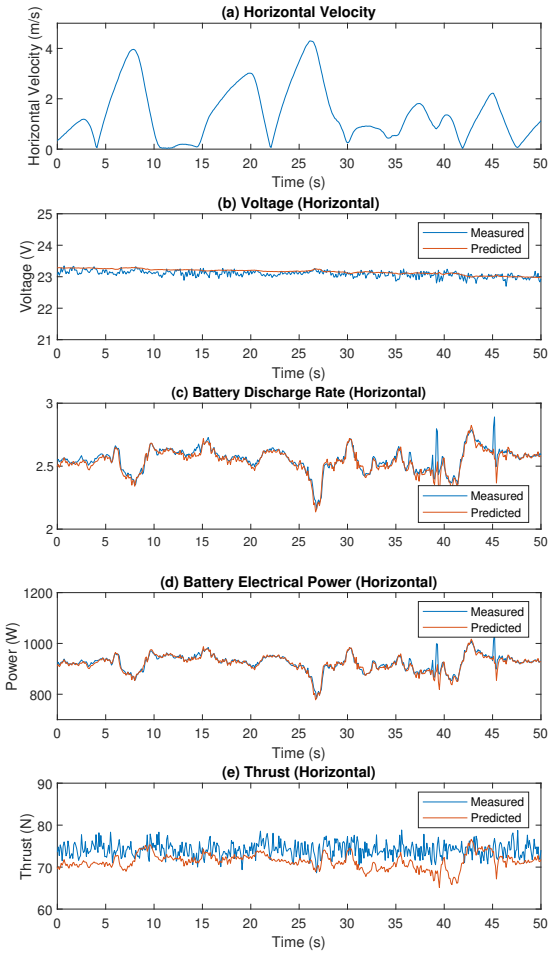

Figure 3.12: Experimental Validation of Model during Horizontal Flight: (a) Velocity, (b) Voltage, (c) Battery Discharge Rate, (d) Battery Electrical Power, and (e) Thrust

Chapter 4

Model-Based Multirotor Performance Analysis

In this chapter, the developed system-level model is used to demonstrate the impacts of individual dynamics on flight performance, including propulsion, power consumption, energy efficiency, and energy-optimal and maximum cruising velocities. The results and analysis highlight the importance and benefits of accommodating the integrated system dynamics in the efforts to improve the multirotor energy and flight performance.

4.1 Impact of Battery Dynamics on Propulsion

The model informs the impact of the battery dynamics on the multirotor propulsion performance. The relationship between battery voltage and key propulsion metrics, i.e. propeller thrust, torque, and angular velocity, under different PWM actuation commands are generated based on the model as in Fig. 4.1, which also shows the comparison with the dynamometer test data.

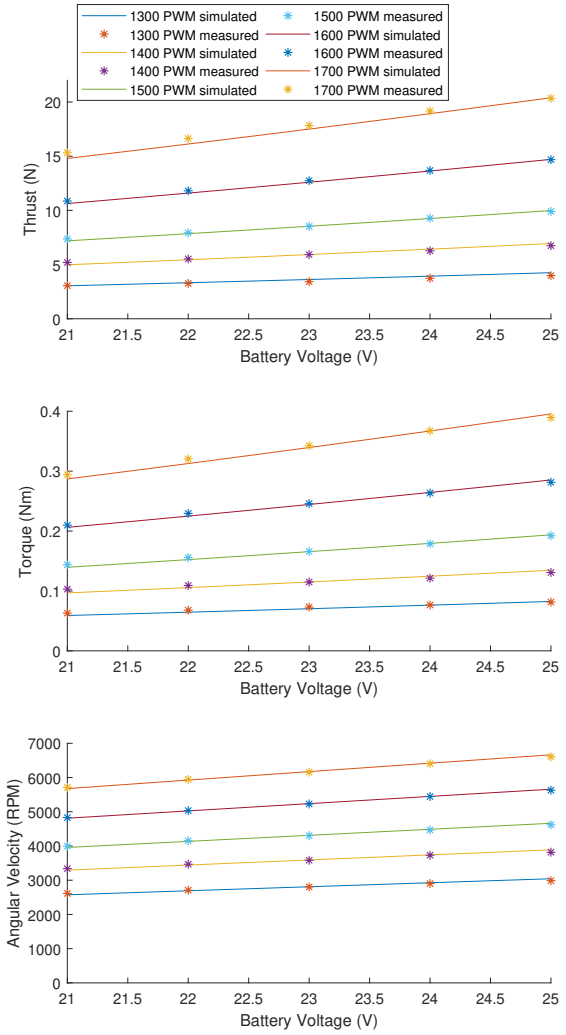

Figure 4.1: Propeller Thrust, Torque, and Angular Velocity versus Battery Voltage

It is seen that when the battery voltage drops across the operating range from 25 V to 21 V, the propulsion performance degrades considerably (under the same PWM). Specifically, over the whole PWM range, there is an average decrease of 24.8%, 23.5%, and 13.4% in propeller thrust, torque, and propeller angular velocity respectively, with maximum decreases of 26.5%, 26.2%, and 14.4% in each. This effect can be explained by the coupling between the dynamics of battery, ESC, motor, and propeller. Specifically, as the battery voltage V_b

drops, the ESC and motor voltages V_{in} and V_m will decrease accordingly based on Eqns. 2.11 and 2.13, which will further reduce the motor/propeller angular velocity ω according to the motor voltage-velocity relationship in Eqn. 2.14. The reduction of ω will lead to the decrease of propeller inflow velocity u based on Eqn. 2.3, and therefore decrease element lift dL and drag dD according to Eqn. 2.1. Subsequently, both element thrust dT and torque dQ decrease according to Eqn. 2.4, and the total decrease in propeller thrust and torque can be calculated from Eqn. 2.7.

These results indicate the significant impact of battery dynamics on the multirotor propulsion performance, which has not been adequately addressed in UAV control and planning literature. Most existing works propose to control the thrust/torque using the propeller angular velocities as inputs by assuming a constant coefficient between the former and (the square of) the latter, but disregard the effect of changing battery voltage on the propeller angular velocity through the motor dynamics [35, 16, 19]. However, over the course of a flight, battery voltage will drop as the energy depletes according to the nonlinear OCV-SOC relationship. As a result, the maximum attainable thrust for a stationary vehicle is reduced by 27.0% from 25 V to 21 V, which leads to roughly an equal amount of drop in the horizontal acceleration limit and a 36.0% drop in the vertical acceleration limit. Meanwhile, the maximum constant horizontal cruising velocity drops by 11.4%, which will be discussed further in Chapter 4.3. Consequently, the control and planning routine calibrated under the nominal condition without considering the impact of varying battery voltage could potentially lead to non-optimal/achievable performance when the battery energy is low, especially in ascending flight and high-speed forward flight.

4.2 Energy Efficiency Analysis of System and Components

Computation of the power consumption and energy efficiency of the components and the whole system can be performed based on the model as

$$
\begin{aligned}
&P_b = I_b V_b \\
&P_{ESC} = V_{in} I_{in} = Q\omega + K_v^2 Q^2 R_m + V_{in} I_0, \quad \eta_{ESC} = P_{ESC}/P_b \\
&P_m = Q\omega, \quad \eta_m = P_m/P_{ESC} = \frac{Q\omega}{Q\omega + K_v^2 Q^2 R_m + V_{in} I_0} = \frac{1}{1 + \frac{K_v^2 Q R_m}{\omega} + \frac{V_{in} I_0}{Q\omega}}.
\end{aligned} \tag{4.1}
$$

Specifically, the battery output electrical power P_b is computed based on the battery voltage V_b and current I_b, which is also the input electrical power to ESC; the ESC output electrical power P_{ESC} (which is also the motor input electrical power) is calculated based on the motor input voltage V_{in} and current I_{in}, and can be decomposed further to the motor output mechanical power, motor ohmic loss, and zero-load loss; and the motor output mechanical power P_m is the product of torque Q and angular velocity ω. The efficiency of the ESC and motor is obtained by dividing the input power by the output power, while that of the propeller is quantified as the thrust to power ratio in Newton per Watt (T/P_m) as a common practice [64], [74], [75]. The system efficiency is computed as the ratio between the total thrust and the battery output power (T/P_b).

The efficiencies have been computed under various conditions including hovering, vertical, and horizontal flights, for the components and the overall system. During the process, the model is used to simulate flights under a sequence of velocities, i.e. 0 m/s for hovering, 0 to 19 m/s forward for horizontal flight, and -5 to 14 m/s vertical for descending and ascending flights, at a constant battery voltage of 25 V. Table 4.1 summarizes the efficiency variation

across flight modes, and Fig. 4.2 shows the evolution of velocity, power consumption, and efficiency for the horizontal flight as an example.

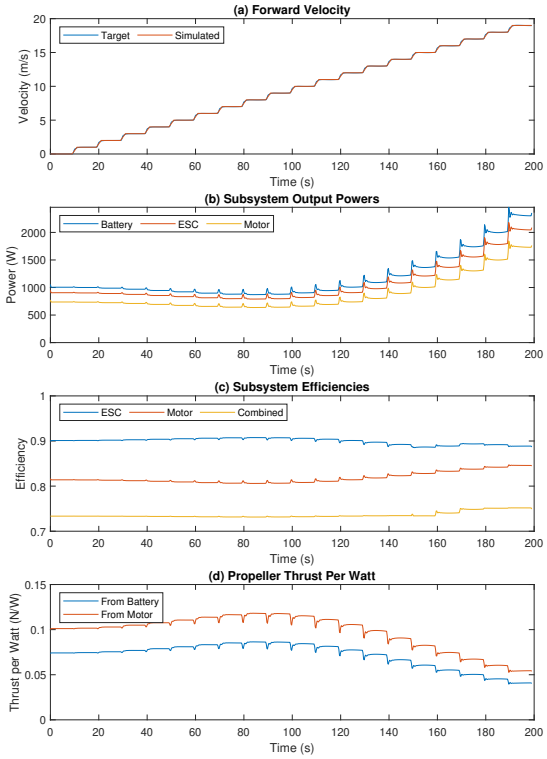

Figure 4.2: Evolution of (a) Velocity, (b) Subsystem Output Powers, (c) Subsystem Efficiencies, and (d) Propeller Thrust Per Watt in Forward Flight with Increasing Velocity

Mode	ESC	Motor	Combined	T/P_m (N/W)	T/P_b (N/W)
Hover	90.1%	81.4%	73.3%	0.101	0.074
Descent	90.1-90.9%	79.8-81.4%	72.5-73.3%	0.101-0.133	0.074-0.097
Climb	88.7-90.1%	81.4-84.9%	73.3-75.3%	0.042-0.101	0.031-0.074
Horizontal	88.9-90.7%	80.6-84.6%	73.1-75.2%	0.054-0.118	0.041-0.086

Table 4.1: Energy Efficiencies in Hover, Vertical (-5 to 14 m/s), and Horizontal (0 to 19 m/s) Flights

It is seen that the ESC efficiency remains relatively constant at 88.7-90.9% under all flight conditions. Even though it drops below 70% when the PWM command is under 1150 according to Fig. 3.4, the actual PWM during operation is typically in the high-efficiency range above. The motor efficiency undergoes more significant variation, namely at 81.4% under hovering and between 80.6-84.9% under forward and vertical flights. The efficiency increases with horizontal and ascending velocity, and decreases with descending velocity, which can be explained by the ratio between the motor output power and the two power loss terms in the denominator of the η_m formula in Eqn. 4.1. Specifically, the motor output power $P_m = Q\omega$ is approximately a cubic function of the PWM input, as the torque Q and the propeller angular velocity ω are roughly quadratic and linear with respect to PWM respectively, according to Fig. 3.6. Meanwhile, the motor zero-load loss $V_{in}I_0$ is linear w.r.t. PWM as the motor input voltage V_{in} is roughly proportional to ω and hence PWM, and the motor ohmic loss $K_v^2 Q^2 R_m$ is quadruple w.r.t. PWM due to the Q^2 factor. Therefore, for horizontal and ascending flights under which the PWM increases with velocity, the ratio between the zero-load loss and the motor output power will decrease, while that of the ohmic loss will increase. Since zero-load loss is the dominant loss term, the overall motor efficiency improves with higher velocity. For descending flight, the trend is opposite as PWM decreases with higher velocity. The propeller efficiency, in terms of thrust per power, is subject to much more significant fluctuations, namely at 0.101 N/W under hovering, between 0.054 and 0.118 N/W under horizontal flight, and between 0.042 and 0.133 N/W under vertical flight. It is also interesting to note that the propeller efficiency decreases with velocity for vertical flight, but is non-monotonic for horizontal flight as the maximum T/P is attained at around 7 m/s. Due to the major impact of propeller efficiency, the overall system efficiency (in

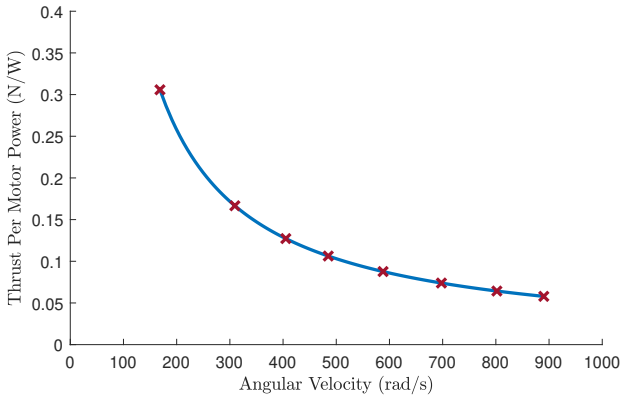

Figure 4.3: Propeller Efficiency (Output Thrust per Unit Input Power from Motor) versus Propeller Angular Velocity at $V_b = 25V$

terms of thrust per battery power) also takes a similar trend. To further clarify the variation in propeller efficiency, the relationship between thrust generated per unit input power and angular velocity ω for a stationary vehicle is shown in Fig. 4.3. According to Eqn. 2.3 and Eqn. 2.7, both T and Q are approximately proportional to the square of ω [58]. Consequently, the mechanical power output from the motor to the propeller, which is computed as $Q\omega$ and hence cubic of ω, increases with ω more rapidly than thrust, and propeller efficiency decreases as angular velocity increases. This effect is especially pronounced at high angular velocities, where a small increase in thrust demand can cause a disproportionately larger increase in power consumption, hence reducing the energy efficiency.

These results show that efficiency is dynamic at both the component and system level, varying considerably under different flight conditions. Our model provides physics-based accurate and detailed computation and analysis, and could greatly benefit the efforts on UAV energy consumption and efficiency evaluation. The current practice often needs to assume a constant lumped efficiency for certain components or even the whole system [19, 22], or disregard the effect of certain subsystem (such as the ESC) entirely [39, 16]. In addition,

the model could also enable system-level optimization of multirotor design (including structures, configuration, and components) and operation (e.g. motion planning and real-time control) to maximize the flight range and time. It is important to accommodate all relevant component dynamics and their interaction in an integrated manner for such practice, as we will demonstrate in the next section that overlooking the complete dynamics will lead to substantially degraded performance.

4.3 Energy-Optimal and Maximum Cruising Velocities

To demonstrate the benefit of using the proposed model for multirotor motion planning and control, the energy consumption per unit distance traveled is generated under different constant horizontal cruising velocities. This is an important metric of the UAV energy performance that has been investigated and optimized in literature through experiment-based techniques [15, 22], while we provide theoretic prediction and physical explanation of the trend and the underlying tradeoff factors based on the model.

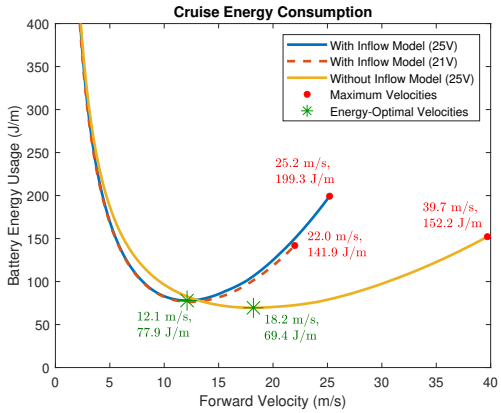

Figure 4.4: Energy Consumption per Meter Traveled versus Forward Cruising Velocity

Fig. 4.4 shows the relationship derived using the full model at 25 V battery voltage

(blue solid curve), at 21 V battery voltage (red dash curve), and that using a simplified model without considering the propeller inflow dynamics (yellow solid curve). It is seen that in general the energy consumed per meter is non-monotonic w.r.t. the forward velocity, starting from the maximum at low velocity, decreasing to the minimum at a certain optimal velocity, and increasing in the high velocity range. However, the detailed profiles and the optimal and/or maximum velocities are different when considering full multirotor dynamics compared with the cases when battery or inflow dynamics are neglected.

According to the full dynamics, there are four tradeoff factors that define the trend. First, as the forward velocity goes up, the increase of distance traveled over unit time reduces the per-meter energy consumption. Second, forward motion will induce an aerodynamic effect on the propeller inflow that improves energy efficiency. Specifically, the forward velocity creates a relative motion between the air and the propeller that increases the inflow velocity component in the rotation plane direction, i.e. u_x in Fig. 2.1, which according to Eqn. 2.7 will add to the thrust production. This effect is prominent under small multirotor pitch angle as the contribution of the horizontal velocity to the respective inflow component is large. Third, as velocity increases, the airframe body drag force will grow quadratically according to Eqn. 2.20, which negatively impacts the energy efficiency especially at high velocity. Finally, forward motion is also associated with another aerodynamic effect which would reduce the energy efficiency. This is because the forward velocity has a component that increases the inflow velocity perpendicular to the propeller rotation plane, i.e. u_z in Fig. 2.1, which according to Eqn. 2.7 will reduce the thrust production. This effect is prominent under large pitch angle. It is also interesting to note the coupling between these factors. Specifically, as the velocity goes up, the pitch angle of the multirotor needs to be

increased to balance the rising body drag. As a result, the positive aerodynamic effect will be suppressed while the negative effect will be enhanced. It is the interaction of these factors that determine the energy consumption-velocity profile and the resultant optimal cruising velocity.

If the model is simplified to not include the full dynamics, the multirotor performance versus velocity relationship will change considerably. For example, when the inflow dynamics are not considered, as shown by the yellow solid curve in Fig. 4.4, the profile becomes significantly flattened, with the energy consumption overestimated in the low velocity range and substantially underestimated at high velocity. More importantly, the predicted energy-optimal velocity of 18.2 m/s deviates remarkably from the 12.1 m/s predicted by the full model, and the actual energy consumption per meter travelled is 36.6% higher than that at the true optimal velocity (106.4 J/m vs. 77.9 J/m). In addition, the simplified model also overpredicts the maximum attainable velocity, which is constrained by the thrust limit, by 57.5% (39.7 m/s vs. 25.2 m/s). The main reason for the large prediction discrepancy is the negligence of the aforementioned two aerodynamic effects related to the inflow dynamics, which are critical tradeoff factors at low and high velocity respectively. Meanwhile, battery dynamics also have a significant impact on the propulsion performance. By comparing the profiles under 25 V and 21 V in Fig. 4.4, it is seen that while the shape of the curve does not change notably, the maximum attainable velocity decreases by 14% from 25.2 m/s to 22 m/s due to the reduction of thrust caused by the lowered motor voltage.

These results demonstrate the importance of accommodating the multiple physical dynamics in multirotor planning and control. First, it is shown that the optimal energy performance is achieved by striking a delicate balance between various trade-off factors underlying

different dynamics. Negligence of certain factors will lead to substantially degraded energy performance in the shown example of identifying the optimal constant cruising velocity. Second, the operation range of the multirotor is defined by different dynamics. As discussed, neglecting inflow or battery dynamics would yield incorrect upper limit of cruising velocity. Using such limit for planning and control could lead to unachievable performance or even safety issues in practice. It is also noted that individual dynamics do not affect the flight performance independently, but rather through the coupling with each other. For example, regarding the pitch-angle dependent effects of the inflow dynamics on thrust generation, the airframe rigid body dynamics need to be considered to accurately compute the pitch angle, and the impact of battery voltage could only be captured through the dynamics of the motor and ESC. Therefore, all relevant dynamics need to be accommodated and integrated in order to correctly represent the system behavior.

Finally, the effect of wind on energy performance can be analyzed, which is shown in Fig. 4.5. Although in this work wind speed is not assumed as known for trajectory generation and UAV control, understanding of wind effect could help explain the experimental results, which are inevitably affected by wind. Considering only the horizontal wind, a hypothetical or measured wind speed can be easily incorporated into the model as an input. This is achieved by including the wind speed in $\dot{X}$ to calculate the body drag in Eqn. 2.20 as well as $v_{x,j}$ and $v_{z,j}$ in Eqn. 2.21. With this correction, results are re-calculated using the airspeed instead of the ground speed. The blue dashed curve in Fig. 4.5 shows the adjusted efficiency-velocity relationship under 5 m/s of wind opposite vehicle motion (headwind), and the yellow dashed curve shows that under wind along vehicle motion (tailwind). Based on the tradeoff factors previously described, the effect of wind is intuitive at high velocities, where

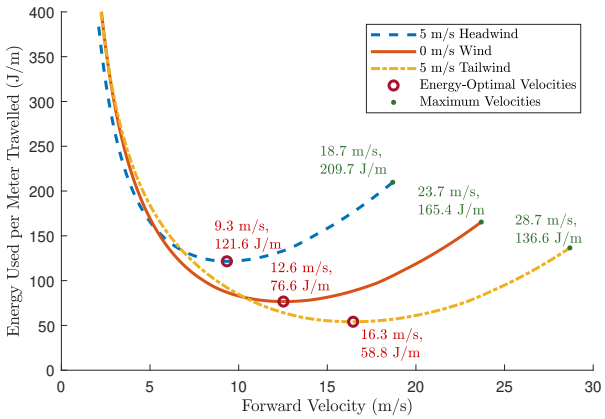

Figure 4.5: Energy Used per Meter Over a Range of Cruise Velocities with and without Wind at $V_b = 23V$

wind opposing the direction of vehicle motion increases energy consumption by increasing the drag resistance, forward pitch angle, and v_z. Similarly, wind in the direction of vehicle motion has the opposite effect. Consequently, the energy-optimal velocity and energy cost per meter vary significantly under wind as shown in the figure. With a headwind of 5 m/s, the minimum energy consumption increases 59% to 121.6 J/m at 9.3 m/s, while a tailwind reduces this energy cost 29.4% to 58.8 J/m at 16.3 m/s. It should also be noted that at low velocities, headwind could actually reduce energy consumption, as it increases v_x and hence thrust production while the growth in drag resistance is minimal. Again, the opposite effect is observed for the tailwind, as the wind in this case reduces v_x. However, low-velocity effects are generally less significant, particularly as the energy-optimal velocities are primarily at the high-velocity region previously discussed.

Chapter 5

Trajectory Optimization and Feedback Control

In this chapter, the system-level dynamic model of the UAV presented in the previous chapters is used to develop an energy-optimal trajectory planning and feedback control framework. Optimization is first performed to generate minimum-energy trajectories for waypoint-to-waypoint flight operations, and PID feedback controllers are then designed for trajectory following in implementation. The performance of the framework is evaluated in simulation and in real-world test flights, and the results are used to discuss key features and behaviors of energy-optimal UAV performance and behaviors.

5.1 Energy-Optimal Trajectory Generation

To generate the energy-optimal trajectories, an optimization problem is formulated with an objective function

$$E_c = \int_0^{t_f} (V_b I_b) dt = \int_0^{t_f} (V_b \sum_{j=1}^{8} I_{b,j}) dt \tag{5.1}$$

to minimize the total energy cost of the operation E_c. To calculate this value, the total electrical power drawn from the battery is calculated as battery voltage V_b times the battery current I_b, which is the sum of all ESC input currents $I_{b,j}$. The power is then integrated from $t = 0$ to the operation end time $t = t_f$ to obtain the total energy consumption. Additionally, due to the relatively short duration of each operation considered in this work, the battery voltage is treated as a constant for trajectory generation. The system is defined in the form of state-space equations, with the state vector considered for control as $\mathbf{q} = [X, \dot{X}, Z, \dot{Z}, \Theta, \dot{\Theta}]^\intercal$. The operation begins with the vehicle in stationary hover at the origin, and ends in hovering at the targeted endpoint with final horizontal position X_f and vertical position Z_f,

$$\begin{aligned} &X(t_f) = X_f, \quad Z(t_f) = Z_f, \quad \Theta(t_f) = 0, \\ &\dot{X}(t_f) = 0, \quad \dot{Z}(t_f) = 0, \quad \dot{\Theta}(t_f) = 0. \end{aligned} \tag{5.2}$$

The control inputs u_1 through u_4 are defined as

$$\begin{aligned} u_1 =& \ddot{Z} = \sum_{j=1}^{8} T_j \cos(\Theta)/m - g, \quad u_2 = \ddot{\Theta} = \tau_\Theta / J_\Theta \\ u_3 =& T_{3/7} - \sum_{j=1}^{8} T_j/8, \quad u_4 = T_{6/8} - \sum_{j=1}^{8} T_j/8. \end{aligned} \tag{5.3}$$

Noted that the control design is presented here using the octorotor architecture shown in Fig. 2.5 as an example, and $T_{3/7}$ and $T_{6/8}$ are the thrusts of the middle-front and middle-rear propellers, respectively. Without loss of generality, the methodology can be applied to other multirotor configurations. The first two inputs emulate a typical piloted flight control mode, where the accelerations of vertical and pitching motion are set explicitly. The third and fourth inputs are used to balance the thrust across the propellers. For two-dimensional operations (along x and z), the propeller thrusts are paired to be symmetric across the x-axis,

as

$$T_{1/5} = T_1 = T_5, \quad T_{2/4} = T_2 = T_4$$
$$T_{3/7} = T_3 = T_7, \quad T_{6/8} = T_6 = T_8 \tag{5.4}$$

with zero total torque along the vehicle y- and z-axis. Under this simplification, any arbitrary combination of four input values corresponds to a unique set of thrust values for each of the four propeller pairs. This configuration also allows us to directly impose constraints on the inputs, e.g.

$$-2m/s^2 \leq u_1 \leq 2m/s^2, \quad -9rad/s^2 \leq u_2 \leq 9rad/s^2,$$
$$-1.5N \leq u_3 \leq 1.5N, \quad -1.5N \leq u_4 \leq 1.5N, \tag{5.5}$$

in order to ensure safe and achievable trajectories. Specifically, the constraints on u_1 and u_2 are calibrated to ensure that the optimized trajectories do not require excessive/unsafe thrust from any propeller, particularly at extreme pitch angles and high climb rates. The constraints on u_2 are relatively loose, as the vehicle is capable of fast rotational adjustments. At the limit of $\pm 9rad/s^2$, this allows the vehicle to rotate from $\Theta = 0$ to $\pm 0.6\ rad$ and stop rotating within $0.52\ s$. Next, the constraints for u_3 and u_4 are set to allow efficient PWM combinations. In optimal solutions, $T_{3/7}$ and $T_{6/8}$ were found to remain fairly close to the average thrust, as they are closer to the center of the vehicle and therefore can provide less angular acceleration than the outer propellers. With these inputs, the derivative of the state vector can be calculated from Eqns. 2.20 and 5.3 as

$$\dot{\mathbf{q}} = [\dot{X}, (u_1 + g)\tan(\Theta) - C_{BD}\dot{X}|\dot{X}|/m, \dot{Z}, u_1, \dot{\Theta}, u_2]^\intercal, \tag{5.6}$$

for projecting the state evolution.

Finally, in order to calculate the current of each propeller, the thrust required from each propeller pair must be found. From Eqn. 5.3, ΣT_j is dictated by u_1 and Θ, meaning $T_{3/7}$

and $T_{6/8}$ can be determined for any combination of state (Θ) and control inputs within the defined constraints. Then, based on Eqn. 2.20, a unique pair of values for $T_{1/5}$ and $T_{2/4}$ exists which corresponds to ΣT_j set by u_1 and τ_Θ set by u_2. To facilitate the solution of the optimization problem, tables of propeller T_j and $I_{b,j}$ as dependent on PWM_j, V_b, $v_{x,j}$, and $v_{z,j}$

$$\begin{aligned} T_j &= T_{table}(PWM_j, V_b, v_{x,j}, v_{z,j}) \\ I_{b,j} &= I_{table}(PWM_j, V_b, v_{x,j}, v_{z,j}), \end{aligned} \tag{5.7}$$

are first obtained by resolving the equations in Section 2.1 that are related to the propeller, motor, and ESC dynamics. By using the tables, optimized solutions can be found without repeatedly resolving the loop in Fig. 2.6 at each time step of the iterative optimization process, significantly reducing the computational intensity of the problem while still providing accurate results.

In this chapter, solutions are examined for a variety of operations. These operations include forward flights with distance of 50 m, 70 m, and 100 m, as well as diagonal climbing flights with the endpoints set at 50 m, 70 m, and 100 m ahead of and 10 m and 20 m above the starting position. Due to the computational load of solving the optimization problem, generating optimized trajectories on demand for real-time vehicle operation may not be feasible, especially if using a vehicle flight controller with limited processing power. Consequently, optimized solutions are determined off-board for the selected operations prior to testing, and the target states are interpolated from these solutions each time the control signal is updated during operation, providing accurate trajectories with minimal real-time computational load. To facilitate the computation, a more flexible and efficient approach for trajectory generation using polynomial approximations has been developed, and will be

discussed in Chapter 6

5.2 Feedback Controller for Trajectory Following

In order to implement the generated target trajectories for real-world UAV operation, a PID control architecture is used for trajectory following as shown in Fig. 5.1. This control architecture consists of a high-level PID controller and a low-level one.

The high-level controller emulates a common manual flight control mode by using a set of PID controllers to generate commands (denoted with the subscript $_C$) for the pitch angle Θ, roll angle Φ, yaw rate $\dot{\Psi}$, and vertical velocity $\dot{Z}$. The commands are generated based on the error between the optimized target trajectories for these vehicle rigid-body states, denoted with the subscript t, and the real-time feedback of the corresponding states. For instance, forward motion is controlled using the pitch angle command Θ_C generated based on the target values for X, $\dot{X}$, and Θ. The trajectories of Θ and $\dot{X}$ are needed due to their significant impact on energy performance, and are supplemented with the X trajectory to ensure that the vehicle reaches and stabilizes at the correct end state. The roll angle command Φ_C is similarly regulated using the target Φ, Y, and $\dot{Y}$ to control horizontal movement perpendicular to the forward axis. As vertical and angular accelerations can be controlled more directly than horizontal motion, the vertical velocity command $\dot{Z}_C$ is regulated based on only Z and $\dot{Z}$, while the yaw rate command is regulated based on Ψ and $\dot{\Psi}$.

The low-level controller contains another set of PID controllers, which receive the commands from the high-level controller and regulate based on the feedback of the corresponding

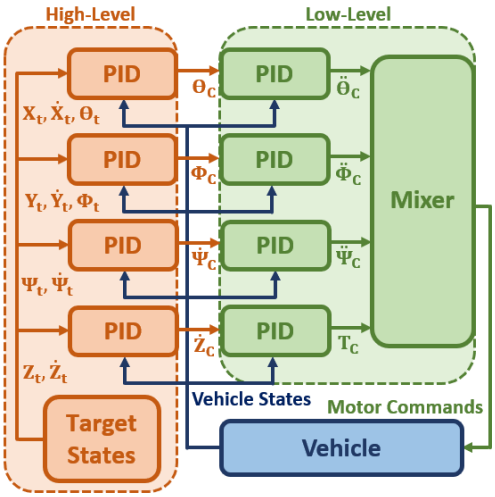

Figure 5.1: Two-level Feedback Control Architecture, including High-Level PID Control to Generate Intermediate commands, and Low-Level PID Control to Generate Throttle and Angular Acceleration Commands

vehicle states. These controllers regulate the acceleration of the pitch, roll, and yaw as well as the throttle command T_C. Based on these commands, a mixer equation is used to calculate the PWM for each propeller ESC, which are the lowest-level actuation inputs applied to the UAV. The throttle command dictates the average PWM across all propellers, which is then modified for each motor to provide the desired angular accelerations of each propeller. Each PID controller in this architecture is calibrated to closely follow the optimized state trajectories with good disturbance rejection.

As benchmark for quantifying the improvement in energy performance, commonly used way-point based controllers are also designed and implemented for comparison. These baseline controllers are constructed using the Auto Mode of the ArduPilot Mission Planner software. In this flight mode, the target horizontal and vertical velocities are set to be linearly proportional to the remaining distance along each direction. The yaw angle is controlled to orient the vehicle towards the waypoint, while the pitch and roll angles are regulated to provide the horizontal acceleration required to match the desired velocity. To ensure that

the vehicle remains stable and the commands are within the operational range of the vehicle, user-defined constraints are imposed on the velocity and acceleration. Specifically, the vertical velocity, vertical acceleration, and horizontal acceleration constraints were set at 5.0 m/s, 1.0 m/s^2, and 4.5 m/s^2 respectively, and two horizontal velocity constraints, namely 18.0 and 12.5 m/s, were tested. The higher velocity limit ($18m/s$) of the first controller, which is referred to as the high-velocity baseline (HVB) controller, allows the vehicle to reach the endpoint as quickly as possible, while avoiding the risk of failing to maintain altitude at higher velocities under adverse wind conditions. The velocity limit ($12.5m/s$) of the second controller, which is referred to as the low-velocity baseline (LVB) controller, is the energy-optimal cruising velocity identified previously from Fig. 4.5 under no wind condition. With this limit, the slower baseline controller is expected to complete operation with lower energy consumption than the faster baseline controller, which operates at more aggressive but less energy-efficient velocity.

5.3 Simulation Testing and Result Analysis

In order to evaluate the performance of the proposed control framework under nominal conditions, the optimal trajectory following and baseline controllers are first implemented and tested in simulation based on the developed multirotor system model. The time and energy required for each controller to complete a series of operations, with target final horizontal position X_f ranging from 50 to 100 m and vertical position Z_f from 0 to 20 m, are obtained and summarized in Table 5.1. It should be noted that it could take a long time for the vehicle to come to a complete stop at the exact end position, due to overshoot and oscillation.

	HVB		LVB		OTF	
X_f, Z_f (m)	Time (s)	Energy (kJ)	Time (s)	Energy (kJ)	Time (s)	Energy (kJ)
(50, 0)	6.8	6.7	6.8 (+0.0%)	6.6 (-1.5%)	5.8 (-14.7%)	5.8 (-13.4%)
(70, 0)	8.2	8.4	8.5 (+3.7%)	8.2 (-2.4%)	7.5 (-8.5%)	7.4 (-11.9%)
(100, 0)	10.3	10.9	11.0 (+6.8%)	10.6 (-2.8%)	10.5 (+1.9%)	9.9 (-9.2%)
(50, 10)	6.9	7.7	6.8 (-1.4%)	7.6 (-1.3%)	5.7 (-17.4%)	6.7 (-13.0%)
(70, 10)	8.2	9.4	8.5 (+3.7%)	9.3 (-1.1%)	7.3 (-11.0%)	8.4 (-10.6%)
(100, 10)	10.3	12.0	11.0 (+6.8%)	11.7 (-2.5%)	9.8 (-4.9%)	10.8 (-10.0%)
(50, 20)	6.9	8.6	6.9 (+0.0%)	8.5 (-1.2%)	5.6 (-18.8%)	7.8 (-9.3%)
(70, 20)	8.2	10.4	8.5 (+3.7%)	10.3 (-1.0%)	7.4 (-9.8%)	9.4 (-9.6%)
(100, 20)	10.3	13.1	11.0 (+6.8%)	12.7 (-3.1%)	9.5 (-7.8%)	11.9 (-9.2%)
Mean			+3.3%	-1.9%	-10.1%	-10.7%

Table 5.1: Evaluation of Energy Performance in Simulation for 3 Controllers, namely Optimized-Trajectory-Following (OTF), High-Velocity Baseline (HVB), and Low-Velocity Baseline (LVB) over a series of Operations

Therefore, the results are calculated at the moment the vehicle moves within a 3 m radius of the target end position. Since the cutoff radius is relatively small and applied equally to each controller, the effect of truncating the operations is minimal and similar, allowing for a fair comparison.

As shown in Table 5.1, the optimized-trajectory-following (OTF) controller reduces the energy consumption significantly over the baseline controllers in all cases, while the low-velocity baseline consistently provides a slight improvement over the high-velocity baseline. Specifically, the OTF controller use an average of around 10.7% and 8.8% less energy than the HVB and LVB controllers, respectively. The optimized trajectories demonstrate distinct patterns from those under the baseline controllers, as shown in Fig. 5.2, which compares the evolution of key vehicle states under each controller and in two sample operations.

Specifically, the first column of the subplots, i.e. Fig. 5.2 (a)-(e), shows the trajectories of X (horizontal) position, X velocity, pitch angle, Z (vertical position), and cumulative energy consumption for the 100 m forward flight, and the second column, i.e. Fig. 5.2 (f)-(j), shows those for the diagonal flight with 50 m horizontal and 20 m vertical motion. In general, the optimized trajectories can be approximately divided based on the forward velocity profile into 3 segments as shown in Fig. 5.2 (b), including an initial period of acceleration to the peak forward velocity, a middle period of cruise and gradual deceleration, and a final braking period when the vehicle rapidly decelerates to stop at the endpoint. The optimized trajectories are shown to include behaviors that improve energy performance in each of these flight segments, as well as effectively balancing the simultaneous horizontal and vertical motion.

First, the improvements in the initial acceleration period are achieved by reaching a steep (negative) pitch angle at the start of the operation to provide high forward thrust. Note that from Eqn. 2.20, a negative pitch angle will result in positive forward acceleration due to the orientation of the body-frame axes as shown in Fig. 2.5. As a result, the forward velocity peaks early, reducing the total time required to reach the endpoint. This peak velocity is lower in operations with a small horizontal component, where high forward velocity is not required or cannot be reached. By comparison, the baseline controllers pitch forward much slower, as they cannot be well-calibrated considering the vehicle system dynamics. Consequently, in relatively short flights, the vehicle will often decelerate sharply immediately after reaching the peak forward velocity, indicating inefficient energy use.

In the middle portion of each operation following the initial acceleration, the OTF controller tends to cruise while gradually pitching backwards and decelerating slightly, whereas

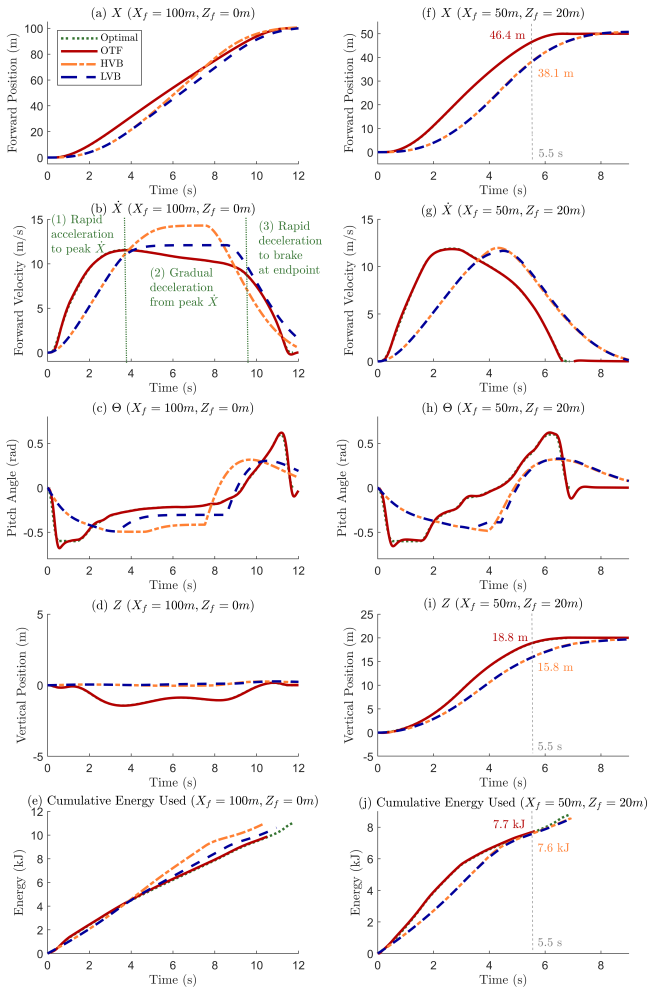

Figure 5.2: Trajectories of Key UAV States under Each Controller in Simulation for Forward ($X_f = 100m, Z_f = 0m$) and Diagonal ($X_f = 50m, Z_f = 20m$) Flights: (a) X Position of Forward Flight, (b) X Velocity of Forward Flight, (c) Pitch Angle of Forward Flight, (d) Z Position of Forward Flight, (e) Cumulative Energy Used of Forward Flight, (f) X Position of Diagonal Flight, (g) X Velocity of Diagonal Flight, (h) Pitch Angle of Diagonal Flight, (i) Z Position of Diagonal Flight, (j) Cumulative Energy Used of Diagonal Flight

the baseline controllers maintain high pitch angle and forward acceleration later into the operation. In this way, the peak forward velocities of the optimized trajectories avoid exceeding the energy-optimal forward cruise velocity shown in Fig. 4.5. This behavior also allows for less extreme pitch angles at high forward velocities, improving energy efficiency by increasing the lift-to-drag ratio as discussed in Section 4.3. The baseline controllers instead maintain a steeper pitch angle, causing increased power requirements over the middle portion of the

operation. This effect can be clearly observed from roughly 4 to 7.5 s in Fig. 5.2 (e), during which time the total energy used by the baseline controllers, especially HVB, is shown to increase much more rapidly than the energy used by the OTF controller.

The optimized deceleration behaviors also demonstrate significant energy saving over the those of the baseline controller. The improvements are in part related to the previous cruise portion of the operation, during which the OTF controller allows the vehicle to start deceleration gradually. Consequently, body drag supplements active braking, reducing both the time and energy costs of the final deceleration portion, compared to the baseline controllers which must actively brake from a higher velocity. Additionally, the optimized trajectories are able to brake more precisely by considering the full vehicle dynamics. For the baseline controllers, the target velocity is directly proportional to the remaining distance to the endpoint. This approach causes the vehicle to gradually slow down as it approaches the endpoint, requiring significant time spent at low and energy-inefficient velocities. As a result, the baseline controllers are less precise than the OTF controller optimized based on the full vehicle dynamics, which allows the vehicle to stop more promptly and efficiently.

Across all flight segments, the OTF controller is also able to balance the forward and horizontal motion of the vehicle more efficiently than the baseline controllers. An example can be observed in the second column of Fig. 5.2, i.e. subplots (f)-(j), showing the trajectories for a diagonal flight with simultaneous horizontal and vertical motion. In subplot (h), it is seen that the optimized trajectory reaches and maintains the steepest forward pitch angle Θ early in the motion from approximately 0.5 to 2 s, during which time the vertical position Z increases slowly as shown in subplot (i). Meanwhile, the baseline controllers are at their steepest forward pitch angles from approximately 2.5 to 4.5 s, when $\dot{Z}$ is also around its peak.

According to the previous analysis in Section 4.3, high pitch angle, when coupled with large perpendicular inflow velocity v_z (which increases with vehicle vertical velocity $\dot{Z}$), would decrease the propeller energy efficiency by reducing the lift-to-drag ratio. Consequently, the baseline controllers will suffer lower energy efficiency compared to the OTF controller, due to the coupling of high pitch angle with high vertical velocity during the course of the motion. The effects of these behaviors can be observed in subplot (j), which shows that, although the power used by the OTF controller is initially higher than that of either baseline controller, the latter increased much faster during the middle portion of the operation, and the total energy used is roughly equal at around 5.5 s. At that point, according to subplots (f) and (i), the OTF controller has almost reached the endpoint, while the baseline controllers still have significant forward and upward distance to cover. Specifically, at this time, the vehicle is 3.8 m from the endpoint (3.6 m horizontal, 1.2 m vertical) under the OTF controller, compared to 12.6 m (11.9 m horizontal, 4.2 m vertical) under the HVB controller. The comparison demonstrates the advantage of the OTF controller in energy efficiency (per distance).

It should also be noted that the calibration and constraint settings generally need to be more conservative for the baseline controllers than for the optimized trajectory-following controller, reducing the operation range as well as the potential of energy saving. This is because the achievable operating limits of the UAV, governed by the underlying fundamental physics, could change under different vehicle conditions. For example, as shown in [58], battery energy depletion over the course of a flight can cause significant reduction in the maximum attainable thrust by the propeller, due to the impacts of battery voltage on propulsion through the motor and ESC dynamics. Therefore, assuming that the vehicle is appropriately modeled, the optimized trajectories could exploit the full energy saving poten-

tial while following the (varying) limits accurately by taking into account the vehicle physical dynamics. By contrast, it would be difficult for the baseline controllers to accommodate both aspects of the performance. On one hand, if the controller is calibrated under the full battery condition, it is likely to request unattainable thrust under low battery, e.g. near the end of the flight, potentially resulting in unsafe operating conditions. On the other, if the controller parameters and constraints are set conservatively to accommodate all operating conditions, the energy performance would be sacrificed.

Finally, based on Table 5.1, the performance of the low-velocity baseline controller can also be evaluated. While this controller does generally have improved energy efficiency over the high-velocity baseline controller, it is only able to achieve a small fraction of the improvement by the optimized trajectory following controller. For example, for the 100 m horizontal flight, the LVB controller reduces the energy consumption over HVB by 2.8%, while the OTF controller achieves a much higher reduction of 9.2%. It is seen from Fig. 5.2 (b) that the improvement by the LVB controller is mainly achieved by keeping the vehicle at the energy-optimal horizontal velocity (which is 12.6 m/s as identified from Fig. 4.5) during the middle cruising portion of the operation, while the velocity under the HVB controller is higher and less energy efficient. Such improvement is more significant in flights with a longer horizontal component as seen across Table 5.1. Nevertheless, the minimal improvement in comparison with the OTF controller demonstrates the importance of optimizing not only the steady-state behavior of the UAV, e.g. cruising velocity, but also the dynamic maneuver, e.g. acceleration, deceleration, and pitching, based on the holistic vehicle system-level dynamics.

5.4 Experimental Validation

In this section, experimental testing results are presented to validate the performance of the optimized trajectories and feedback control. The testing platform and control implementation is described first in this section, followed by the experimental procedures and result analysis.

5.4.1 Testing Platform

The test vehicle previously described in Chapter 3.2.2 is used for testing, which can be controlled to perform different flight operations with data measured and recorded for analysis and validation. Regarding the control software, as described in Chapter 5.2, the feedback controllers of the developed framework are implemented using the custom script of the ArduPilot Mission Planner in a two-layer PID control architecture. The high-level control runs in a ground station computer, which communicates with the low-level control in the onboard flight controller for exchange of command and sensor information as well as data logging. Each of the vehicle states required for feedback control as shown in Fig. 5.1 are calculated from a combination of measurements from the vehicle's GPS, accelerometer, and gyroscope hardware. The sensor measurements are processed and filtered by the onboard flight controller, providing accurate measurements of the required vehicle rigid-body states which can be accessed in real time for feedback control. As the benchmark for comparison, the aforementioned two baseline controllers are also implemented for testing using the waypoint-based Auto Mode navigation function of the Mission Planner.

5.4.2 Experimental Procedure

Four vehicle operations previously shown in Chapter 5.1 were performed for experimental validation. These operations included horizontal flights, with distance of 50 m, 70 m, and 100 m, and diagonal forward climbing flight, with the endpoint set at 50 m ahead of and 20 m above the starting position. The experiments were conducted at the Woodland-Davis Aeromodelers field, which is an open-air flat grass UAV test ground in Davis, CA, shown in Fig. 3.7. It is noted that wind can have significant impact on vehicle performance, as discussed in Chapter 4.3. This impact is demonstrated in Fig. 4.5, as a moderate 5 m/s wind speed is shown to affect both the optimal energy-efficiency and respective cruising velocity substantially. To comprehensively evaluate the vehicle energy performance under the inevitable wind, each operation was repeated in multiple directions, including towards, opposite, and perpendicular to the wind heading. The wind speed and heading were obtained based on the trim condition under stationary hovering test. Specifically, when the vehicle is hovering, the body drag caused by horizontal wind is equal in magnitude and opposite in direction to the horizontal component of the total thrust,

$$C_{BD}\dot{V}_{wind}^2 = |\sum_{j=1}^{8} T_{j,horiz}|. \tag{5.8}$$

The total thrust ΣT_j, and the magnitude and direction of its horizontal component $\Sigma T_{j,horiz}$, can be calculated using the equations in Chapter 2.1.4 and the measured orientation of the vehicle. Using this approach, the wind was measured multiple times over the course of testing to account for the changing wind conditions. For each measurement, the trim condition was recorded at multiple yaw angles to improve accuracy and compensate for potential sensor bias. The overall average wind speed was found to be approximately 5 m/s heading South

at the day of testing, which agreed with weather reports. Specific wind measurements for each operation are provided in Chapter 5.4.3.

5.4.3 Validation Results and Analysis

The experimental testing results are presented in Table 5.2. This table summarizes the total energy consumption under each controller for each operation and vehicle heading, as well as the improvement over the HVB controller. The wind conditions for each group of operations are also specified, including wind velocity and direction (vehicle heading) measured by angle clockwise from North. It is noted that, due to time and battery energy constraint during testing, results for the LVB controller are only available for 50 m and 100 m forward flights. As mentioned in Chapter 5.3, to consistently compare each controller, the cumulative energy consumption for each operation was calculated at the time when the vehicle entered a certain radius around the endpoint (increased to 4 m to accommodate greater variance due to wind disturbances and sensor noise under experimental conditions).

Based on these results, the developed trajectory optimization and feedback control framework is shown to achieve a significant reduction in energy use relative to both baseline controllers. Averaged across all operations, the proposed OTF controller based on the optimized trajectories uses 10.2% less energy than the high-velocity baseline controller, and 8.3% less than the low-velocity baseline. The observed improvements are in good match with those from simulation testing in Chapter 5.3, which show average improvement of 10.7% and 9.0% respectively. To examine individual operations in more detail, Fig. 5.3 shows the trajectories of key vehicle states for $50m$ forward flights under different headings using the OTF

X_f, Z_f (m)	(50, 0)			(70, 0)	
Controller	HVB	OTF	LVB	HVB	OTF
Wind (m/s, °)	5.4, 167	6.4, 200	5.3, 180	6.4, 200	3.9, 163
0°	6.8 kJ	5.3 kJ (-22.1%)	6.5 kJ (-4.4%)	8.7 kJ	7.4 kJ (-14.9%)
45°	5.8 kJ	5.2 kJ (-10.3%)	5.6 kJ (-3.4%)	7.9 kJ	7.2 kJ (-8.9%)
90°	5.4 kJ	4.8 kJ (-11.1%)	5.3 kJ (-1.9%)	6.7 kJ	6.4 kJ (-4.5%)
180°	5.2 kJ	4.6 kJ (-11.5%)	5.3 kJ (+1.9%)	5.9 kJ	5.7 kJ (-3.4%)
225°	5.0 kJ	4.1 kJ (-18.0%)	5.2 kJ (+4.0%)	6.3 kJ	5.9 kJ (-6.3%)
270°	5.4 kJ	5.5 kJ (+1.9%)	5.3 kJ (-1.9%)	7.0 kJ	6.6 kJ (-5.7%)
Mean	5.6 kJ	4.6 kJ (-11.9%)	5.5 kJ (-0.9%)	7.1 kJ	6.5 kJ (-7.3%)
X_f, Z_f (m)	(100, 0)			(50, 20)	
Controller	HVB	OTF	LVB	HVB	OTF
Wind (m/s, °)	3.9, 163	5.3, 180	5.3, 180	6.4, 200	3.9, 163
0°	10.5 kJ	10.6 kJ (+1.0%)	10.5 kJ (+0.0%)	-	-
90°	9.1 kJ	8.5 kJ (-6.6%)	8.7 kJ (-4.4%)	8.6 kJ	6.8 kJ (-20.9%)
180°	8.3 kJ	7.4 kJ (-10.8%)	8.3 kJ (+0.0%)	8.5 kJ	6.5 kJ (-23.5%)
270°	8.8 kJ	8.4 kJ (-4.5%)	8.9 kJ (+1.1%)	8.6 kJ	7.5 kJ (-14.0%)
Mean	9.0 kJ	8.7 kJ (-5.3%)	9.1 kJ (-0.9%)	8.6 kJ	6.9 kJ (-19.5%)

Table 5.2: Energy Consumption under 4 Experimental Flight Operations in Different Directions for 3 Feedback Controllers including High-Velocity Baseline (HVB), Optimized-Trajectory-Following (OTF), and Low-Velocity Baseline (LVB)

and HVB controllers. These experimental results demonstrate that the energy performance improvements achieved in simulation are largely captured in real-world operation, and that the overall behaviors of each controller are similar. Meanwhile, the improvements achieved by the OTF controller is slightly worse than those in simulation due to the uncertainties and disturbances under real-world experimental conditions. In particular, wind has been shown

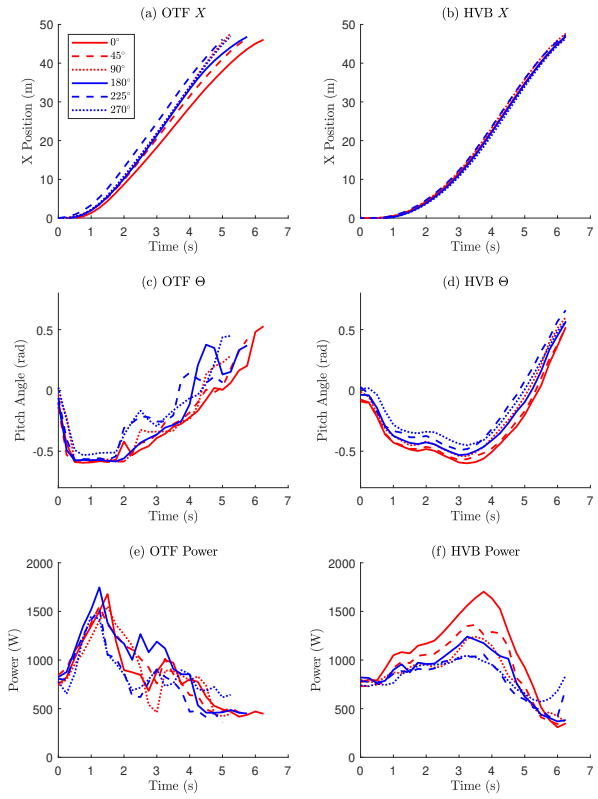

Figure 5.3: Evolution of Vehicle States in 50 m Forward Flight Using Optimized-Trajectory-Following and High-Velocity Baseline Controllers: X-Axis (forward) Position for (a) OTF and (b) HVB, Pitch Angle for (c) OTF and (d) HVB, and Power Consumption for (e) OTF and (f) HVB

to significantly affect the vehicle, and several specific behaviors are observed, which explain the discrepancy between simulated and real-world performance.

One behavior beneficial to the energy performance of the OTF controller relative to the baseline controllers is the larger variation of the forward velocity with respect to wind. As described in Chapter 5.2, the baseline control architecture sets the pitch angle command to follow a forward velocity target, which is dependent on the remaining distance to the end-point. Consequently, under the baseline controller, the only rigid-body state with significant variation is the pitch angle, allowing the vehicle to track the forward velocity target closely

under whatever wind conditions. By contrast, the OTF controller calculates the pitch angle command using the errors of three states relative to the target trajectories, i.e. forward position, forward velocity, and pitch angle, each with an assigned weight. Under wind disturbance, the controller would not be able to track all three states exactly, and this effect actually helps improve the energy efficiency over the baseline controllers. Specifically, the maximum forward velocity reached by the OTF controller is generally lower when travelling against the wind, and higher when travelling with the wind. This variation, which can be observed in the OTF forward position trajectories shown in 5.3 (a), coincides with the trend of the energy-optimal cruising velocity with respect to wind, as shown in Fig. 4.5. Consequently, the vehicle velocity under the OTF controller remains closer to the wind-adjusted optimal forward velocity near the middle of the operation, while the baseline controllers reach approximately the same maximum forward velocity regardless of wind. This difference is particularly notable due to the high forward velocity target of the HVB controller, at which the energy cost per meter can increase significantly with headwind. As a result, despite the consistency of the forward position and velocity profiles over different wind conditions, the power used by the baseline controller, shown in Fig. 5.3 (f), is observed to increase considerably near the middle of the operation when travelling against the wind.

Meanwhile, there are some other behaviors of the OTF controller that could lead to degraded energy performance under real-world experimental conditions. First, the OTF controller tends to be more sensitive to disturbances, as demonstrated in Fig. 5.3 by the larger variation of the vehicle state trajectories compared to those of the baseline controller. This is in part due to the PID gains of the OTF controller, which are calibrated to be more aggressive and responsive compared to the baseline controllers, enabled by the underlying

physical model. While the responsiveness improves the energy performance as discussed in Chapter 5.3, it would also make the OTF controller more sensitive to wind disturbances. Second, the vehicle trajectories are currently optimized as time sequences, which also makes trajectory following more susceptible to wind disturbances. For example, the braking portion of the trajectory occurs at a fixed time regardless of the position of the vehicle, and hence the vehicle may sometimes slow down earlier than expected when traveling against the wind. This would result in undershoot in trajectory following, which requires the vehicle to accelerate again after braking, leading to waste of energy. This effect tends to be more significant in longer flights, due to the accumulation of position errors caused by wind disturbances. While this effect does not cause substantial degradation in energy efficiency, the vehicle energy performance can be further improved by parameterizing the trajectory in terms of vehicle states, e.g. forward position and velocity, instead of time. One approach is to formulate trajectory optimization as an optimal control problem and derive control policies, which could perform trajectory generation in real time based on feedback of the actual vehicle states.

It is also noted that there were some fluctuations in wind conditions across flights that could affect the comparisons. For instance, in the 100 m forward flight case, the wind speed was higher for operations under the OTF controller (5.3 m/s) than those under the HVB controller (3.9 m/s). This had a particularly significant impact on the performance of the northbound operations (i.e. against the wind), where the baseline slightly outperformed the OTF controller, in part due to the wind speed favoring the former. Although the opposite effect occurs when travelling with the wind, the impact is less substantial, as it can be observed in Fig. 4.5 that the effect of wind opposite vehicle motion is generally greater in

magnitude than that of the same wind assisting vehicle motion. In the 70 m forward flight case, the performance improvement of the OTF controller (over HVB) is instead the best when travelling North and worst when travelling South, while the opposite is true in the 100 m case, as wind speed during the OTF controller operation is lower than that during the HVB operation in the 70 m case but higher in the 100 m case. This effect does not generally favor either the HVB or OTF controllers, but introduces uncertainty and fluctuations in the results, which is the main reason why experiments were repeated multiple times in various directions to ensure more fair comparison of controller performance.

The OTF controller achieves the largest improvement over the baseline controllers in the diagonal flight case ($X_f = 50$, $Z_f = 20$) in experiments (-19.8% on average), which is significantly higher than in simulation (-9.3%). In both cases, the improvement is largely due to the ability of the optimized trajectories to balance both horizontal and vertical motion efficiently, as described in Chapter 5.3. However, the more prominent performance improvement observed in the experimental data is also caused by a baseline controller behavior not seen in simulation. Specifically, the HVB controller was observed to decelerate horizontally earlier than expected in diagonal flight, requiring the vehicle to take additional time and energy regaining forward velocity to reach the endpoint. This behavior appears to be a result of the real-world implementation of the controller, which tries to avoid overshoot by attempting to reach the vertical and horizontal end states simultaneously. This issue demonstrates the difficulty of calibrating a robust and efficient baseline controller capable of balancing motion along multiple axes, due to the total reliance on feedback with no knowledge of underlying system physics.

Finally, it can be observed that the energy consumption for each controller and operation

group in experiments is generally lower than that in simulation. One possible cause is the larger radius about the target point used in experimental testing to identify the end of operation, which was necessary to accommodate the greater variance introduced by wind effects. As another possible explanation, there may be slight discrepancies between the UAV model and the real-world test vehicle. For example, the body drag coefficient was identified using data from previous experiments, by fitting the model prediction of forward acceleration to measurement under horizontal vehicle motion. Although multiple trials were used to minimize variance, there are potential uncertainties, such as those introduced by wind effects, which would induce errors in the result. However, despite these discrepancies, the OTF controller achieves significant reduction in energy consumption in all cases of flights, and the improvement over the baseline controllers is similar in experiments and simulation, demonstrating the effectiveness of the developed planning and control framework to improve vehicle energy performance in real-world applications.

Chapter 6

Polynomial Approximation for Efficient Trajectory Generation

While the optimized trajectory generation approach developed in the previous chapter minimizes the energy cost of vehicle operations, the significant computational requirements of the approach make it impractical for real-time trajectory generation, particularly for hardware with limited processing power such as a vehicle onboard controller. To address this limitation, we propose to use polynomial equations to characterize the energy-optimal trajectories in this chapter, which can be used for efficient trajectory generation for a wide range of vehicle operations. These approximations, which substantially reduce the computational complexity of planning and control, capture key energy-efficient behaviors identified from the optimized trajectories, and are shown to achieve similar energy performance as the optimized trajectories in both simulation and real-world test flights.

6.1 Trajectory Fitting

In order to characterize the polynomial approximations, a reference set of optimized trajectories was generated for operations with destination $[X_f, Z_f]$ over the range of $0m \leq X_f \leq 70m$

and $-30m \leq Z_f \leq 50m$, as shown in Fig. 6.1 (a). Specifically, the optimized trajectories are generated at 10 m increments along the X-axis and 5 m increments along the Z-axis over most of the range, except at 10 m increments along both axes over the range of $15m \leq X_f \leq 65m$ and $-25m \leq Z_f \leq 25m$. From these results, key patterns were identified and used to categorize operations into 3 groups, which are then fitted with polynomial approximations capturing the energy-efficient behaviors.

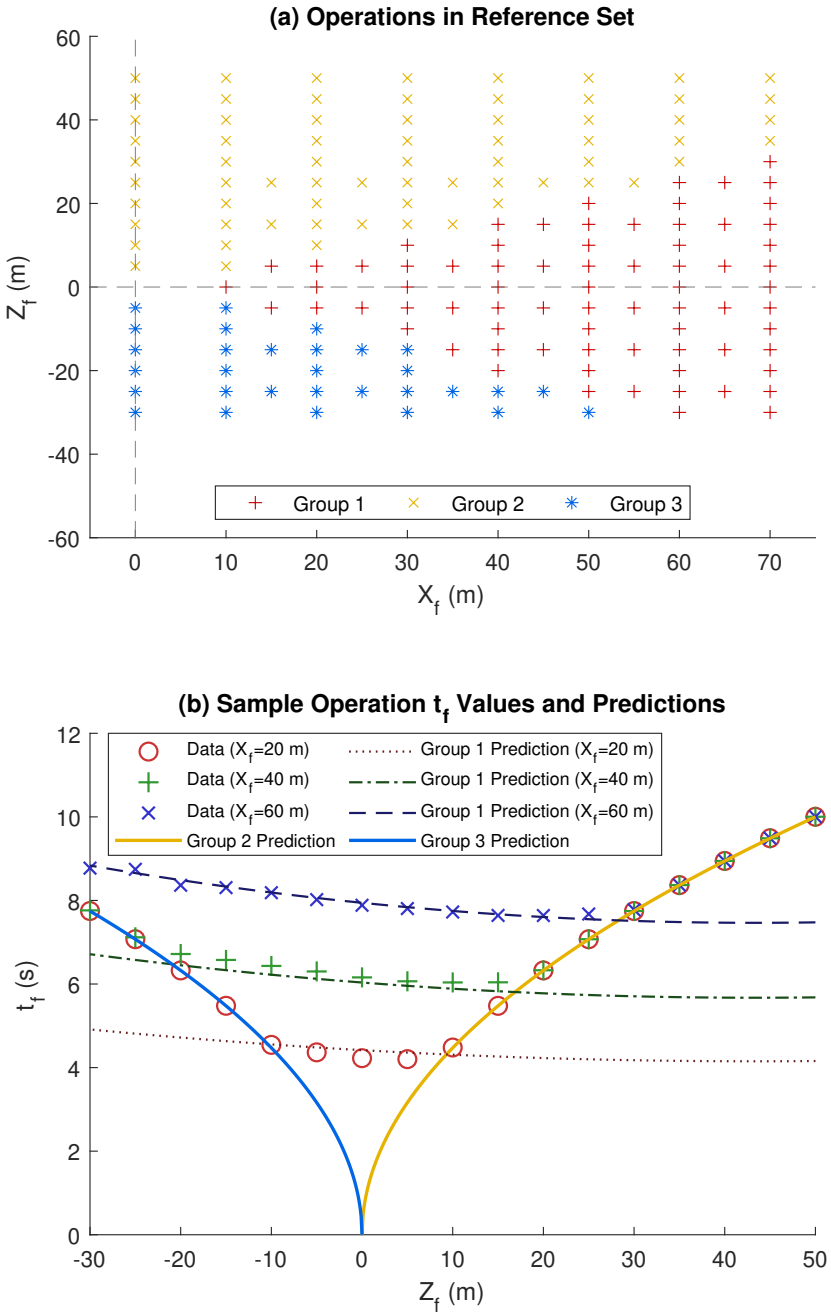

Figure 6.1: (a) Categorization of Operation Endpoints for Optimized Trajectories in Reference Set into 3 Groups; (b) End Time (t_f) for Sample Operations and Predicted Values for Different Groups

6.1.1 Operation Groups

Based on the relationship between the operation end time t_f and the destination (X_f and Z_f) shown in Fig. 6.1 (b), operations can be divided into three groups within the reference range. As is visible in Fig. 6.1 (a), operations in group 1 have relatively longer forward flight components, and so t_f is primarily influenced by X_f. For operations in groups 2 and 3, the vertical component is longer, and so t_f is instead solely dictated by Z_f. The 2 groups are divided according to the direction of Z_f, with climbing operations ($Z_f > 0$) in group 2 and descending operations ($Z_f < 0$) in group 3.

In group 1, while the end time $t_{f,G1}$ is primarily affected by X_f, $t_{f,G1}$ is also negatively correlated with Z_f. This is because a larger vertical displacement necessitates a higher average thrust throughout the operation, which in turn increases the horizontal acceleration of the vehicle and reduces operation time. To capture these factors, $t_{f,G1}$ is approximated as

$$t_{f,G1} = (C_{1,t_f}{X_f}^2 + C_{2,t_f}X_f + C_{3,t_f})(C_{4,t_f}{Z_f}^2 + C_{5,t_f}Z_f + C_{6,t_f}). \tag{6.1}$$

Here, C_{1,t_f} through C_{6,t_f} are constant coefficients fitted based on the reference set, and are given in Eqn. 9.3 of the Appendix 9.4. Eqn. 6.1 is found to predict the actual values closely, with an error mean of $0.01s$ (0.2%) and standard deviation of $0.12s$ (3.9%) across all reference operations in this group. In group 2 and 3, due to the vertical acceleration constraint of $\pm 2m/s$ set in Chapter 5.2, Z_f is sufficiently large that the vehicle is unable to reach the endpoint in the time predicted by Eqn. 6.1. As a result, t_f is dictated strictly by Z_f and the vertical acceleration limit magnitude $\ddot{Z}_{max} = 2$ as

$$t_{f,G2} = t_{f,G3} = \sqrt{4Z_f/\ddot{Z}_{max}} = \sqrt{|2Z_f|}, \tag{6.2}$$

which is the minimum time in which the vehicle can reach the endpoint. The predictions

for these groups again match the actual values well, with an error mean of -0.01s (-0.2%) and standard deviation of 0.04s (0.6%) for group 2, and -0.03s (-0.5%) and 0.07s (1.1%) for group 3.

With these operation groups defined, polynomials can now be derived to approximate the trajectories of the states needed for feedback control, which include $\dot{X}_t$, Θ_t, and $\dot{Z}_t$ as described in Chapter 5.2. Meanwhile, X_t and Z_t trajectories are also needed to ensure position tracking, and can be obtained by numerically integrating the corresponding velocity trajectories over the operation time. Noted that as the polynomials used to calculate t_f and the velocity trajectories are characterized separately, it is not guaranteed that the position trajectories obtained by integrating the velocities will end at the target X_f and Z_f exactly. Therefore, the position and velocity trajectories are scaled accordingly to correct for small discrepancies and ensure that the exact endpoint is reached.

6.1.2 Group 1

Regarding group 1, to capture key energy-efficient behaviors and their varying features across operations, the relevant trajectories are divided into segments for each reference operation. A sample operation for this group is shown in Fig. 6.2, which includes both the optimized target trajectory and the polynomial approximation for the operation with endpoint $X_f = 60m$, $Z_f = 20m$. The segment boundaries are marked for $\dot{X}_t$, $\dot{Z}_t$, and Θ_t.

For $\dot{X}_t$ and Θ_t, five segments are used. The first segment captures the initial forward acceleration of the vehicle, during which the vehicle pitches forward rapidly, subject to the Θ and $\ddot{\Theta}$ constraints. After reaching the Θ constraint, this pitch angle is held until the

segment end time $t_{1,X,G1}$. In segment 2, Θ starts decreasing (in magnitude), as the vehicle continues accelerating but at a slower pace until $\dot{X}$ reaches its peak value. In segment 3, the vehicle begins to decelerate gradually using body drag, as the pitch angle reduces to nearly zero. This segment ends when Θ passes -0.05 rad, which is selected rather than 0 rad to avoid fluctuations that tend to occur in the optimized Θ trajectories at around 0 rad. These fluctuations, which have limited impact on overall energy performance, are attributed to minor numerical imprecision during optimization , and would obfuscate the boundaries between segments if split across segments 3 and 4. Segments 4 and 5 capture the final deceleration behavior of the vehicle as it approaches X_f. In segment 4, Θ gradually increases to the upper limit of 0.6 rad for maximum braking, while in segment 5, Θ rapidly decreases to reach 0 precisely at the endpoint.

Similarly, $\dot{Z}$ is divided into 5 segments based on Z-axis behaviors observed across operations in this group. In the first segment, which is typically very brief, vertical acceleration is minimal. This allows for increased thrust to maximize forward acceleration once a higher pitch angle is reached without causing Z-axis overshoot. To balance forward and vertical motion, this segment increases in duration with X_f and decreases with Z_f, and hence does not appear in all operations. Next, segments 2 and 3 contain the period of vertical acceleration, which is held at the maximum limit (2 m/s^2) in segment 2. In segment 3, the vertical acceleration begins decreasing, and the vehicle continues to accelerate upwards gradually, until reaching the maximum value of $\dot{Z}$. The vehicle then decelerates vertically to stop eventually at Z_f in segments 4 and 5, which are divided by the 2 seconds mark before the end of the operation. This value was chosen to capture the behaviors observed in the reference set during the final $2s$ of operations in group 1, featuring rapidly-changing pitch angle to adjust

thrust during segment 5.

With these segments defined, the optimized trajectories for each segment of each reference operation are normalized along both the time and magnitude axes. The normalized segments are then averaged across operations, and the averages are used to fit a set of sixth-order polynomial equations. The normalized state trajectory segments and the corresponding averages for the forward velocity and pitch angle profiles in this group are shown in Fig. 6.3. The corresponding figures for the vertical velocity are given in Fig. 9.7 of Appendix 9.4, along with the coefficients for the normalized polynomials in Table 9.2.

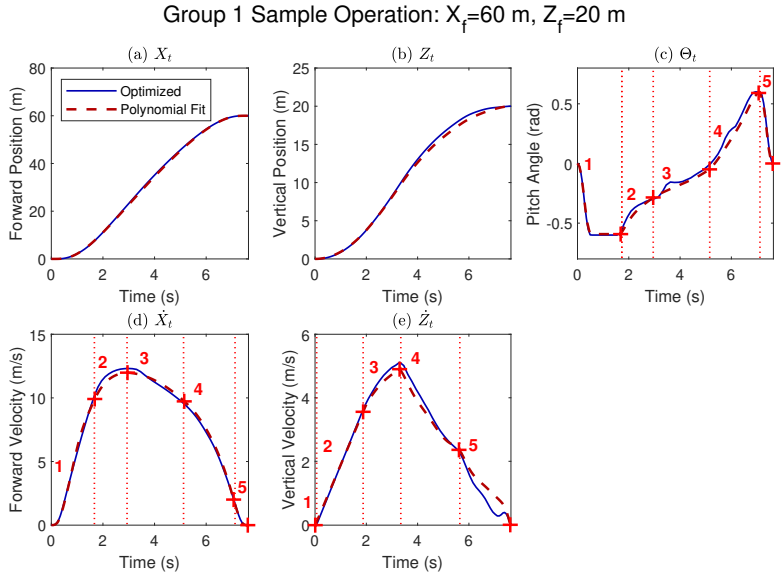

Figure 6.2: Optimized State Trajectories and Polynomial Approximations for a Sample Operation in Group 1, with Polynomial Segments Indicated; (a) Forward Position, (b) Vertical Position, (c) Pitch Angle, (d) Forward Velocity, (e) Vertical Velocity

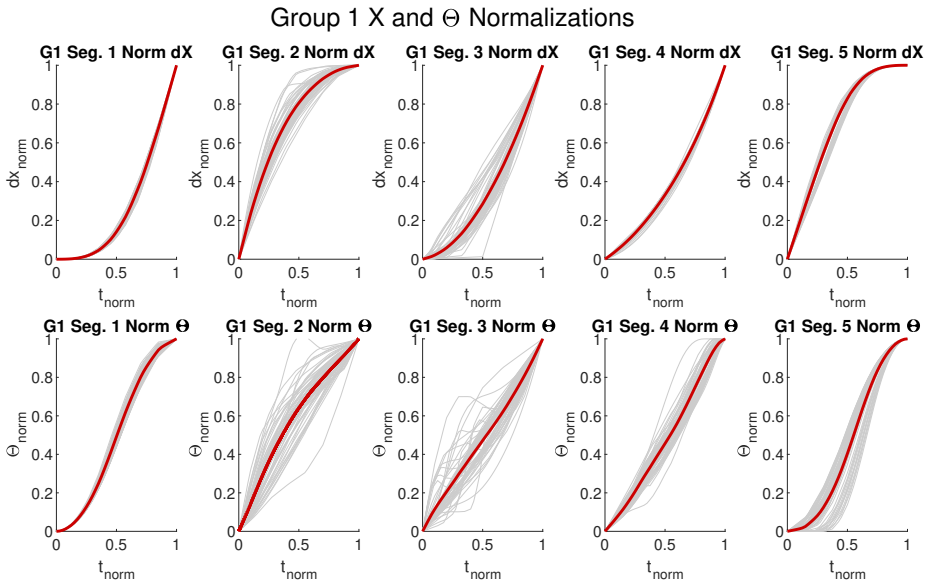

Figure 6.3: Normalized State Trajectory Segments for $\dot{X}$ and Θ for Group 1 Operations

Next, to use these polynomial approximations to generate trajectories for a given operation, equations must be defined to determine the end of each segment. Each segment end state is approximated by a linear relationship with respect to a certain combination of X_f and Z_f. The end state values of $\dot{X}$ and Θ for each operation in the group 1 reference set, as well as the corresponding linear approximations, are shown in Fig. 6.4 with equations for all group 1 segment end states given in the appendix in Eqns. 9.4 and 9.5. For example, the equations for the end times of $\dot{X}$ and Θ segments 1 through 4 in group 1 are approximated as

$$\begin{aligned} t_{1,X,G1} &= 0.1631(X_f - Z_f/2)^{0.5} + 0.5294 \\ t_{2,X,G1} &= 0.03483(X_f - Z_f/2) + 1.210 \\ t_{3,X,G1} &= t_{2,X} + 0.0004470(X_f + 0.35Z_f)^2 + 0.1921 \\ t_{4,X,G1} &= t_f - 0.5487, \end{aligned} \tag{6.3}$$

while the values of $\dot{X}$ at the end of these segments are approximated as

$$\begin{aligned}
\dot{X}_{1,G1} =& 0.9000(X_f + Z_f/2)^{0.5} + 2.5170 \\
\dot{X}_{2,G1} =& 0.9893(X_f + Z_f/2)^{0.5} + 3.8678 \\
\dot{X}_{3,G1} =& \min\{0.1039X_f + 5.7009, 9.8581\} \\
\dot{X}_{4,G1} =& 2.0362.
\end{aligned} \tag{6.4}$$

Note that the $G1$ subscripts here denote that these equations apply to group 1, and the X subscripts in Eqn. 6.3 are used to distinguish from the $\dot{Z}$ segment end times, which are instead calculated using Eqn. 9.5 in Appendix 9.4. Although these relationships were determined by fitting the reference solutions, there is typically a logical correlation underlying the obtained polynomial. For example, $t_{1,X,G1}$ and $t_{2,X,G1}$ increase with X_f due to the increased total duration of the operation, but decrease with Z_f as the increased thrust reduces the time needed for accelerating. Similarly, $\dot{X}_{1,G1}$ and $\dot{X}_{2,G1}$ increase with X_f, as higher forward velocity is required to reach the endpoint, as well as with Z_f, as more thrust is available for early acceleration to reach higher velocity. It should also be noted that some of the equations are constant, typically due to the definition of the segment (e.g. the aforementioned $\Theta_{1,G1}$, which is set to -0.6 rad), or due to the consistent behavior observed across operations. Finally, piecewise linear fits are used for certain cases, such as $\dot{X}_{3,G1}$, as it was found to increase linearly with X_f up to a maximum value at $X_f = 40m$, then remain nearly constant at an average of 9.86 m/s . Similarly, $\dot{Z}_{1,G1}$, shown in Eqn. 9.5 and Fig. 9.4 of Appendix 9.4, saturates at a maximum value of 0, and $\dot{Z}_{2,G1}$ is affected by the saturation of $\dot{Z}_{1,G1}$ as well as its own lower limit of 0.

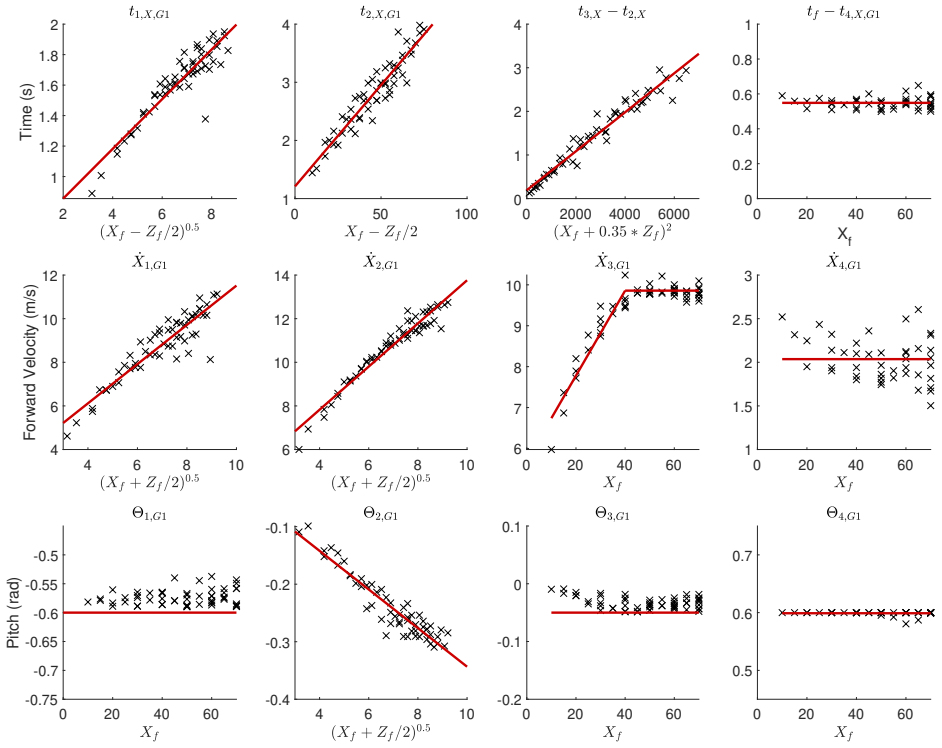

Figure 6.4: Group 1 t_X, $\dot{X}$, and Θ Segment End Values, Including Fitted Equations (Red) and Actual Values from Reference Optimized Trajectories

6.1.3 Groups 2 and 3

In groups 2 and 3, which contain operations with relatively large vertical components, t_f is dictated by Z_f and the vertical acceleration constraint as defined in Eqn. 6.2. Consequently, operations in these two groups exhibit similar behaviors, and are typically simpler than operations in group 1. Most notably, only two segments are needed for $\dot{Z}$ in these groups. As shown in Fig. 6.5, vertical acceleration is held at the positive maximum limit for the first half of the operation in group 2, and the negative maximum limit for the remainder. This behavior minimizes the time required to complete the operation, which outweighs the loss of propeller efficiency compared to a more gradual approach. The opposite behavior is

observed in group 3, where maximizing downward velocity both reduces operation duration and increases propeller efficiency.

For $\dot{X}$ and Θ, four segments are used. Segment 1 contains the initial forward acceleration period, and is similar to the equivalent segment in group 1, except that the (negative) maximum pitch limit is not reached in the cases with a small X_f value where high forward acceleration is not required. In the cases when the pitch angle limit is not reached, the segment simply ends when the pitch angle reaches its peak value. Segment 2 ends when the forward velocity reaches its maximum value, and segment 3 (deceleration) ends at the peak pitch angle, which typically does not reach the upper limit in these groups. The segment end state equations for group 2 are given as Eqn. 9.6 and shown in Fig. 9.5 of Appendix 9.4. It should be noted that all segment end state equations for segment 1 in this group use two piecewise linear segments, as the pitch angle does not always reach the limit as previously mentioned. Additionally, less data was available for group 3, primarily due to the limitations of blade element momentum theory in descending flight [64], which made the generation of optimized trajectories less accurate below $Z_f = -30m$. As a result, the polynomial approximation in group 3 tend to be less accurate, and simpler equations are used to avoid further overfitting. The segment end state equations for group 3 are given in Appendix 9.4 as Eqn. 9.7 and shown in Fig. 9.6 For both groups 2 and 3, the segment polynomial approximation coefficients are given in Table 9.3 and shown in Fig. 9.8.

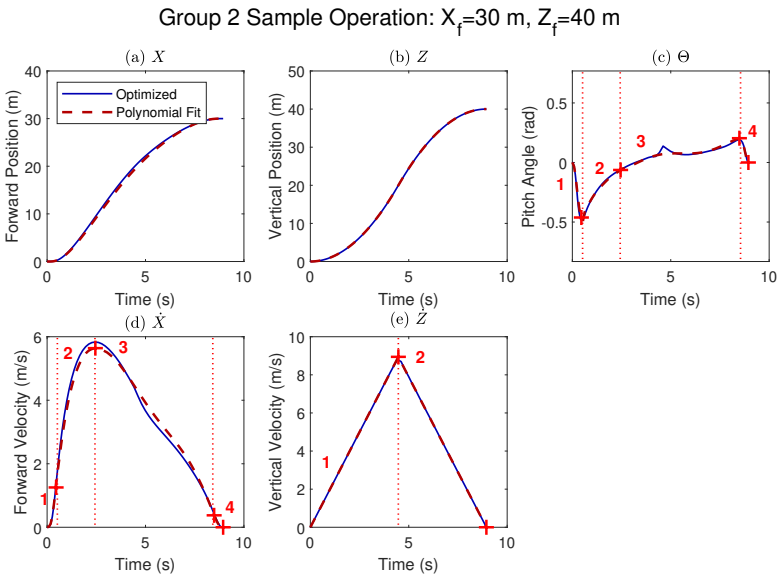

Figure 6.5: Optimized State Trajectories and Polynomial Approximations for a Sample Operation in Group 2, with Polynomial Segments Indicated; (a) Forward Position, (b) Vertical Position, (c) Pitch Angle, (d) Forward Velocity, (e) Vertical Velocity

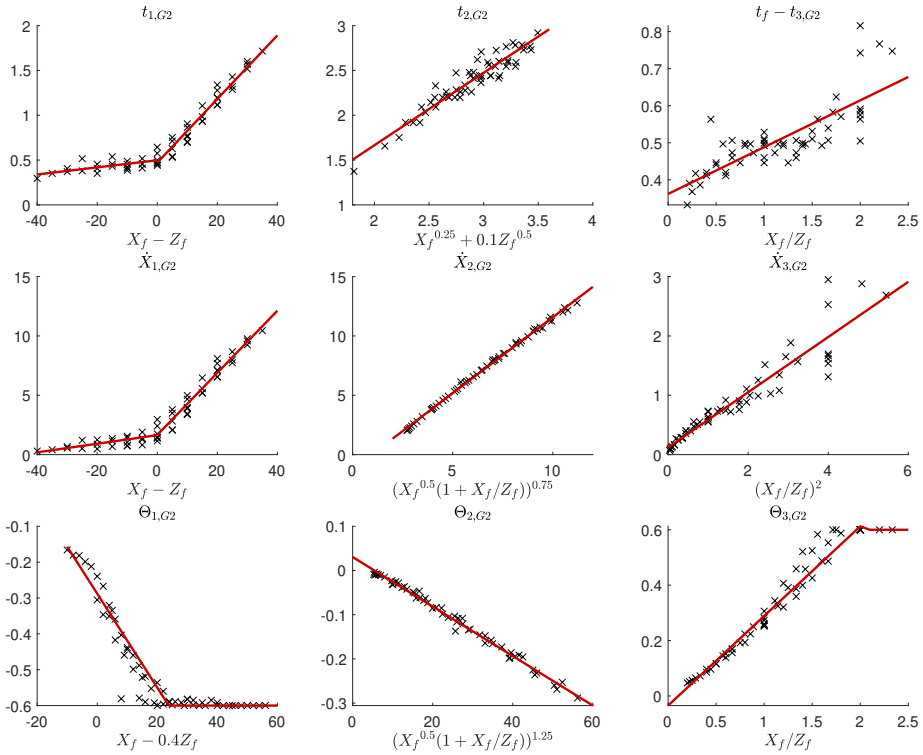

Figure 6.6: Group 2 t_X, $\dot{X}$, and Θ Segment End Values, Including Fitted Equations (Red) and Actual Values from Reference Optimized Trajectories

6.2 Performance Evaluation of Fitted Trajectories

In this section, the performance of the approximated trajectories is evaluated in simulation and real-world flight experiments, in comparison with both the originally optimized trajectories and the baseline controller.

6.2.1 Evaluation in Simulation

In order to evaluate the polynomial approximations over the full range of operations, simulations were performed similarly to those in Chapter 5.3. Specifically, the energy costs for each operation in simulated feedback control using the fitted polynomial trajectories (referred to as the polynomial trajectory following (PTF) controller) were compared to those obtained using the optimized trajectory following (OTF) controller as well as to those of the high-velocity baseline (HVB) controller. Numerical simulation results over a range of X_f and Z_f are given in Table 6.1, with summary statistics presented in Table 6.2. Additionally, the full trajectories for a sample operation with $X_f = 60m$ and $Z_f = 20m$ are shown in Fig. 6.7.

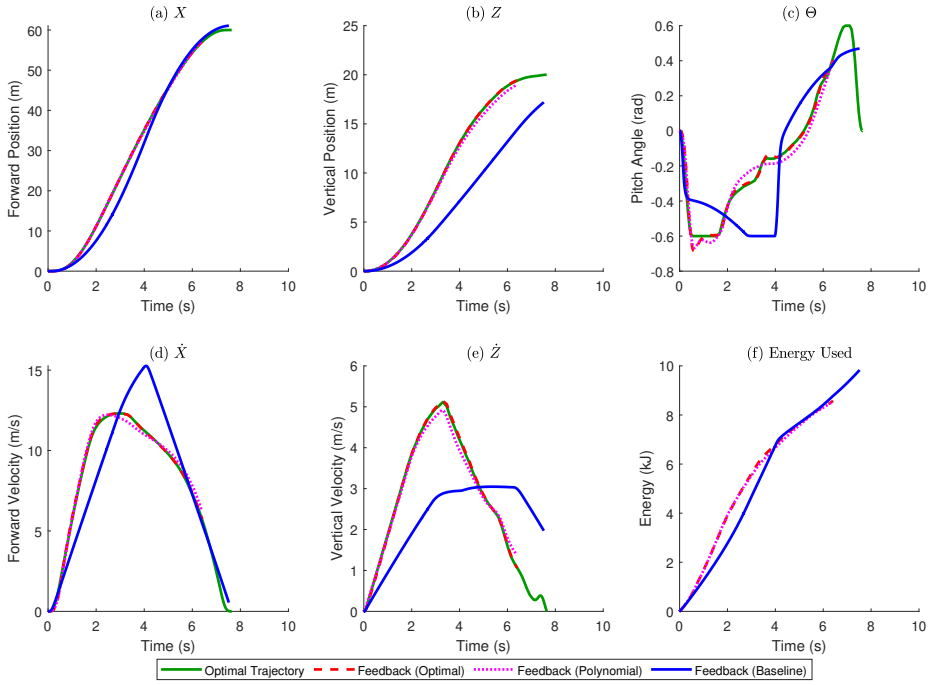

Figure 6.7: Simulation Results for a Sample Operation ($X_f = 60m$, $Z_f = 20m$), Including Optimized State Trajectories ("Optimal Trajectory") and Feedback Control Results Using Optimized Trajectories ("Feedback (Optimal)"), Polynomial Trajectories ("Feedback (Polynomial)"), and Baseline Controller ("Feedback (Baseline)"); Subplots: (a) Forward Position, (b) Vertical Position, (c) Pitch Angle, (d) Forward Velocity, (e) Vertical Velocity, (f) Energy Consumption

The fitted polynomial trajectories are shown to approximate the optimized trajectories accurately in most cases, using a slight 1.3% more energy on average than the optimized trajectories across the full operation range, with a standard deviation of 3.1%. While the energy cost is very similar between the two in most cases, the polynomial fits deviate more significantly from the optimized trajectories in descending forward flight (relative to ascending). As a result, the mean energy cost differences in groups 1 and 3 are slightly larger than the overall average, at 2.1% and 1.9% respectively. While this overall difference is small, larger discrepancies are observed for individual operations, especially at those with long descending distance (i.e. large negative values of Z_f), up to a maximum difference of

15.1% for the case of $X_f = 70m$, $Z_f = -30m$. This is again due to the limitations of the blade element momentum theory in descending flight, which tend to make the optimization results less consistent in operations with significant negative Z_f components. These limitations prevented accurate generation of optimized trajectories below $Z_f = -30m$, and so, as shown in 6.1 (a), group 3 has fewer reference operations available than groups 1 and 2. Consequently, it is more difficult to properly characterize the polynomials to achieve accurate trajectory generation for those descending flights. From the full data, it is also noted that there is a smaller cluster of operations near $X_f = 10m$, $Z_f = 0m$ where the polynomial fits perform poorly in percentage error. This is primarily due to the very short length of operations and hence low energy consumption in this range, and a small difference in energy cost would cause a large percentage difference. Finally, the best results for the polynomial trajectory approximation are achieved in group 2, with a mean difference of only 0.3%. This is attributed to the larger number of operations available for fitting in this group than in group 3, as well as the more consistent behaviors than in group 1, which contains climbing, forward, and vertical flight operations.

The results comparing the polynomial trajectory following controller to the high-velocity baseline controller are also given in Table 6.1, which demonstrate that the majority of the improvements in energy cost achieved by the original optimized trajectories are retained by the polynomial trajectories. Across the complete range of operations, the polynomial trajectories achieve an average improvement of 22.4% in energy cost relative to the baseline controller. The polynomial trajectories outperform the baseline in all groups, with average energy cost reductions of 14.7% in group 1, 21.1% in group 2, and 41.9% in group 3, respectively. Notably, the largest improvements tend to occur in operations with larger vertical

displacements. This is attributed to the ability of the optimized trajectories to better balance horizontal and vertical motion than the baseline controller, as discussed in Chapter 5, which is captured by the polynomial trajectories. Additionally, the baseline controller requires more strict (conservative) vertical velocity and acceleration constraints to ensure safe operation of the vehicle, while the trajectory-following controllers are capable of safely exploiting the operation envelop to reach the endpoint more rapidly in flights with a larger vertical component. This effect is especially significant in group 3, where the higher descending velocity also increases propeller efficiency as discussed in Chapter 4.3.

6.2.2 Experimental Validation

To validate the polynomial trajectory generation, a set of test flights were performed, with results given in Table 6.3. The PTF, OTF, and HVB controllers were tested for three operations, with endpoint coordinates (i.e., X_f and Z_f) set to 50 m forward and 0 m up for the first operation, 50 m and 20 m for the second, and 10 m and 20 m for the third. These tests largely repeated the testing procedure previously described in Chapter 5.4.2, with some adjustments noted. In particular, each operation was again run multiple times to control for variation in experimental conditions, but the operations were tested in a single direction of travel in order to better reduce variations caused by environmental effects. In addition, the vehicle's mass was reduced from 7.6 kg to 7.0 kg as a result of repairs.

From the results in Table 6.3, it is observed that the OTF and PTF controllers perform similarly across all three operations. On average, the PTF controller uses 3.1% less energy than the OTF controller for the first operation (forward 50 m), 5.3% more energy for the

second (forward 50 m and up 20 m), and 0.9% less energy for the third (forward 10 m and up 20 m). It is noted that, for all three operations, the range of results for the OTF and PTF controllers overlaps, and the average PTF energy usage is within one standard deviation of the OTF average. The reductions in energy consumption relative to the HVB controller are also of note, and are found to be consistent with simulated results. Specifically, from the experimental results, the PTF controller reduces energy consumption for the three operations by 10.5%, 7.2%, and 22.4%, respectively, as compared to 13.2%, 10.0%, and 21.6% in simulation. The equivalent values for the OTF controller were found to be 7.6%, 11.9%, and 21.7% from the experimental results and 13.2%, 9.9%, and 22.1% in simulation. While these reductions for the PTF controller in the first two operations are reduced slightly relative to the simulation results, they are sufficient to conclude that, in real-world operation, the PTF controller captures the majority of the energy savings achieved in simulation, as well as those achieved by the OTF controller.

		$X_f(m)$			
	$Z_f(m)$	10	30	50	70
HVB Energy Cost (kJ)	50	15.5	15.4	15.8	16.5
	30	10.3	10.3	10.7	11.4
	10	5.3	7.3	7.7	9.2
	-10	4.2	4.6	5.7	7.2
	-30	6.6	6.4	6.1	5.9
OTF Energy Cost (kJ) & Change from HVB (%)	50	11.9	11.9	12.1	12.8
		-23.2%	-23.3%	-23.2%	-22.3%
	30	8.2	8.3	9.0	10.5
		-20.6%	-19.5%	-16.3%	-8.0%
	10	3.8	5.1	6.7	8.4
		-27.6%	-30.5%	-12.9%	-9.4%
	-10	2.2	3.4	5.0	6.5
		-48.6%	-27.5%	-13.2%	-9.3%
	-30	4.2	3.7	3.8	5.2
		-37.0%	-42.5%	-37.9%	-11.9%
PTF Energy Cost (kJ) & Change from HVB (%)	50	11.9	11.9	12.1	12.9
		-23.0%	-23.2%	-23.3%	-22.1%
	30	8.2	8.3	9.0	10.5
		-20.4%	-19.3%	-15.8%	-8.1%
	10	3.9	5.0	6.7	8.4
		-27.2%	-31.1%	-13.4%	-8.8%
	-10	2.2	3.3	5.0	6.8
		-47.6%	-28.1%	-12.5%	-5.1%
	-30	4.1	3.8	4.1	5.9
		-38.0%	-40.4%	-33.1%	+1.5%

Table 6.1: Sample Simulation Results for Polynomial Trajectory Following (PTF), Compared to Optimized Trajectory Following (OTF) and High-Velocity Baseline (HVB) Controllers

		Total	Group 1	Group 2	Group 3
OTF v. HVB	Mean	-23.3%	-16.5%	-21.3%	-42.9%
	SD	+11.4%	+9.3%	+3.5%	+4.5%
PTF v. HVB	Mean	-22.4%	-14.7%	-21.1%	-41.9%
	SD	+11.8%	+10.2%	+3.5%	+4.6%
PTF v. OTF	Mean	+1.3%	+2.1%	+0.3%	+1.9%
	SD	+3.1%	+3.9%	+0.6%	+4.1%

Table 6.2: Summary Statistics for Comparison of Polynomial Trajectory Following (PTF), Optimized Trajectory Following (OTF), and High-Velocity Baseline (HVB) Controllers

	(50 m, 0 m)			(50 m, 20 m)			(10 m, 20 m)		
Iteration	HVB	OTF	PTF	HVB	OTF	PTF	HVB	OTF	PTF
1	5.04 kJ	4.73 kJ	4.54 kJ	7.81 kJ	7.02 kJ	6.82 kJ	5.82 kJ	4.71 kJ	4.44 kJ
2	4.89 kJ	4.62 kJ	4.49 kJ	7.78 kJ	7.01 kJ	7.18 kJ	5.72 kJ	4.46 kJ	4.70 kJ
3	5.27 kJ	4.37 kJ	4.51 kJ	7.51 kJ	7.14 kJ	7.51 kJ	6.00 kJ	4.73 kJ	4.63 kJ
4	5.05 kJ	4.97 kJ	4.58 kJ	7.82 kJ	6.08 kJ	7.19 kJ	6.15 kJ	-	4.61 kJ
Mean	5.06 kJ	4.67 kJ	4.53 kJ	7.73 kJ	6.81 kJ	7.17 kJ	5.92 kJ	4.64 kJ	4.59 kJ
		-7.6%	-10.5%		-11.9%	-7.2%		-21.7%	-22.4%

Table 6.3: Energy Consumption under 3 Experimental Flight Operations for 3 Feedback Controllers including High-Velocity Baseline (HVB), Optimized- Trajectory-Following (OTF), and Polynomial-Trajectory-Following (PTF)

Chapter 7

Mission Planning

The focus of this chapter is motion planning at the mission level, with the goal of identifying the optimal ordering of waypoints in 3D space yielding the minimum energy consumption. The work is enabled by the energy-efficient trajectory generation between waypoints developed in the previous chapters. In this chapter, the structure of the mission is first described, followed by the proposed approach for mission optimization and the baseline approaches for comparison. The optimization is performed over a large number of missions with randomized waypoint locations, and key features of the optimal waypoint ordering and energy performance improvements are identified and analyzed. In particular, it is interesting to find that the minimum-energy order is not identical to the minimum-distance order in majority of the missions due to the impact of motion on the aerodynamic efficiency of the UAV.

7.1 Problem Formulation and Optimization Approach

As shown in Fig. 7.1, a mission considered in this work consists of a set of N_W waypoints in 3D space, i.e. $\{W_i\}_{i=1}^{N_W}$, which the vehicle visits each once before returning to its starting position (origin O). The goal of mission planning is to minimize the total energy consumption

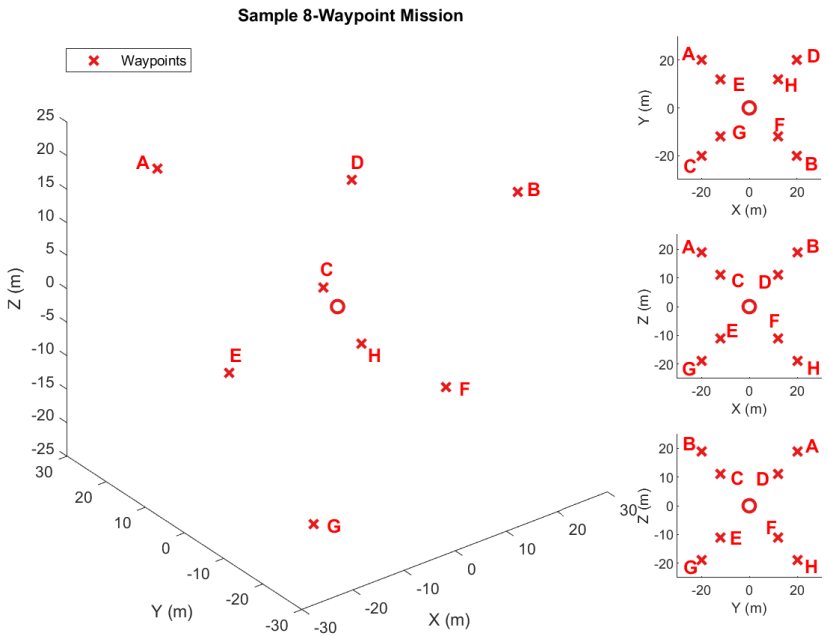

Figure 7.1: Waypoints for a Sample Mission with $N_W = 8$

over the whole mission,

$$\min_{S} E = \sum_{i}^{N_W - 1} E_{W_{s_i} \to W_{s_{i+1}}} + E_{O \to W_{s_1}} + E_{W_{s_{N_W}} \to O} \tag{7.1}$$

where the optimization variable $S = [s_1, s_2, ...s_{N_W}]$ is the order of visiting the N_W waypoints, $E_{W_{s_i} \to W_{s_{i+1}}}$ denotes the energy cost for the vehicle to move between adjacent waypoints, and $E_{O \to W_{s_1}}$ and $E_{W_{s_{N_W}} \to O}$ are the energy costs to start from and return to the origin. It is noted that the energy costs are the minimal energy consumption that can be achieved by the energy-optimal trajectory studied previously. To evaluate such energy costs, a reference table was pre-calculated using the polynomial trajectories for waypoints over a range of horizontal (X_f) and vertical (Z_f) displacements, as plotted in Fig. 7.2. In this work, interpolation from this table is used to predict the energy cost between any pair of waypoints in Eqn. (7.1). The optimization is subject to constraints on UAV dynamics, including limits on acceleration, velocity, and pitch angle among others. In addition, the vehicle needs to stop and hover at

each waypoint before proceeding to the next one. This mission structure is a realistic setting with wide real world applications, including surveillance, inspection, and delivery tasks, in which a multirotor UAV needs to stop and take images, perform measurements, or drop packages at each waypoint. It is noted that this problem is a form of the NP-hard travelling salesman problem, and solutions can be computationally difficult to find for large N_W. While it is possible to obtain the approximate solutions efficiently using heuristic approaches for large N_W [76, 44], the focus of this work is to explore the features of the optimal order, and hence we consider N_W between 6 and 10 and use enumeration to find the exact solutions.

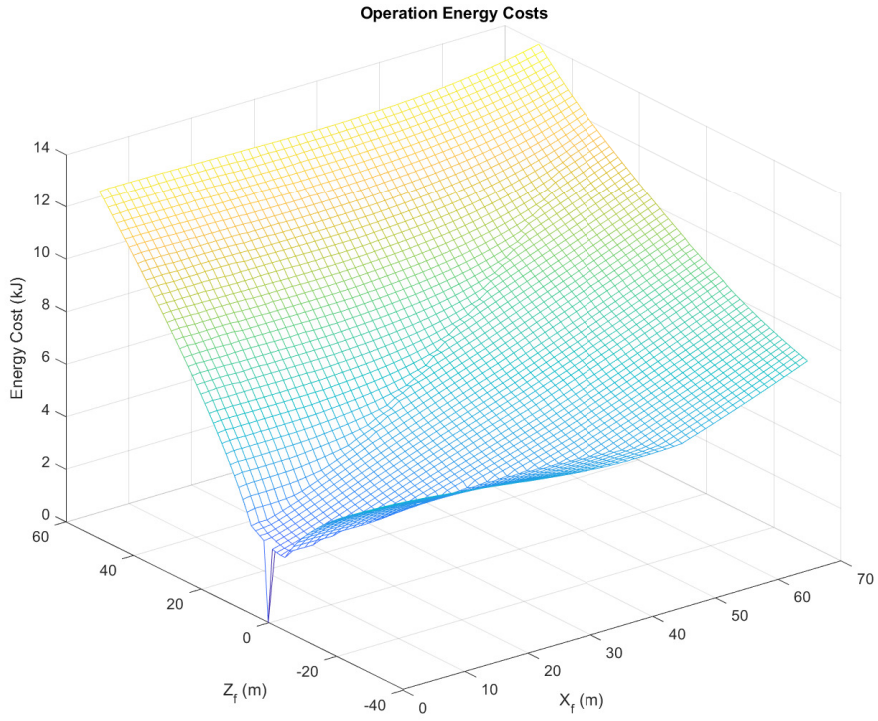

Figure 7.2: Reference Table for Optimal Energy Costs between Waypoints over a Range of Horizontal and Vertical Displacements

To demonstrate the performance improvement achieved by the energy-optimal mission planning, the minimum-distance orders of the waypoints are also determined as the base-

line for comparison, which can be more easily found without understanding the multirotor energy dynamics. Specifically, 3 types of minimum-distance orders are considered, namely those minimizing the horizontal distance X_M, vertical distance Z_M, and total distance D_M. The energy consumption of these orders are evaluated the same way as the energy-optimal order. It will be seen that by analyzing and comparing the energy consumption against these 3 orders, the underlying mechanisms of the energy-optimal order can be better understood, which are heavily dependent on the energy dynamics of the horizontal and vertical motion. Also noted that each minimum distance order can be traversed in two directions, which could have different energy implications. Additionally, for any mission with $N_W > 2$, multiple minimum vertical distance orders could exist and the one with the shortest horizontal distance X_M is chosen as the minimum order for analysis.

7.2 Optimization Results and Energy Performance Analysis

In this section, optimization is first performed for large number of missions to evaluate the energy performance of the optimal ordering, especially the statistics compared with the baseline minimum-distance ordering. To further interpret the results, two sample missions will be discussed in detail, which demonstrate the key features of the minimum energy order related to the fundamental energy dynamics of the multirotor.

7.2.1 Statistics of Mission Optimization Results

To evaluate the performance of mission planning, large numbers of missions ($500 - 5000$) with random waypoint locations are generated over a series of N_W and operation ranges. The results comparing the energy performance of the different ordering approaches are presented in Table 7.1, which shows the increase in energy consumption of the 3 min-distance orders over the min-energy order in percentage. The histogram for one combination of mission parameters (8 waypoints within range $-30m < X < 30m$, $-30m < Y < 30m$, $-25m < Z < 25m$) are given in Fig. 7.3, where the x-axis denotes the ratio of energy cost of each min-distance order to that of the min-energy order. It is seen that for majority of the missions, the minimum-distance order does not give the minimum energy consumption, as indicated by the "% Min-$D_M \neq$ Min-Energy" column in Table 7.1, e.g. in 83.3% of the missions for $N_W = 6$ and 95.8% for $N_W = 10$.

				Energy Cost Relative to Min-Energy Order							
	Range (m)		No. of	Min-X_M		Min-Z_M		Min-D_M			% Min-D_M
N_W	X&Y	Z	Missions	Mean	90$^{\text{th}}$ %ile	Mean	90$^{\text{th}}$ %ile	Mean	90$^{\text{th}}$ %ile	Max	$\neq$ Min-Energy
6	±30	±25	5000	+7.16%	+14.58%	+2.72%	+5.99%	+2.15%	+5.19%	+14.87%	83.32%
8	±20	±25	5000	+16.25%	+26.68%	+2.53%	+5.18%	+2.62%	+5.75%	+13.51%	93.70%
8	±30	±25	5000	+10.16%	+18.40%	+3.19%	+6.49%	+2.81%	+6.10%	+12.93%	91.66%
8	±40	±25	5000	+6.12%	+12.66%	+4.29%	+8.75%	+2.12%	+4.87%	+12.60%	85.72%
8	±30	±15	5000	+4.27%	+9.76%	+4.98%	+9.29%	+1.58%	+3.76%	+10.58%	84.80%
10	±30	±25	500	+12.57%	+20.18%	+3.69%	+7.08%	+3.36%	+6.55%	+13.27%	95.80%

Table 7.1: Average, Maximum, and 90$^{\text{th}}$ Percentile Energy Cost Increase over Min-Energy Order of Min-X_M, Z_M, and D_M Orders for Missions with Varying Number of Waypoints and Ranges

Furthermore, the maximum difference between the two orders is as high as 10.6-14.9%

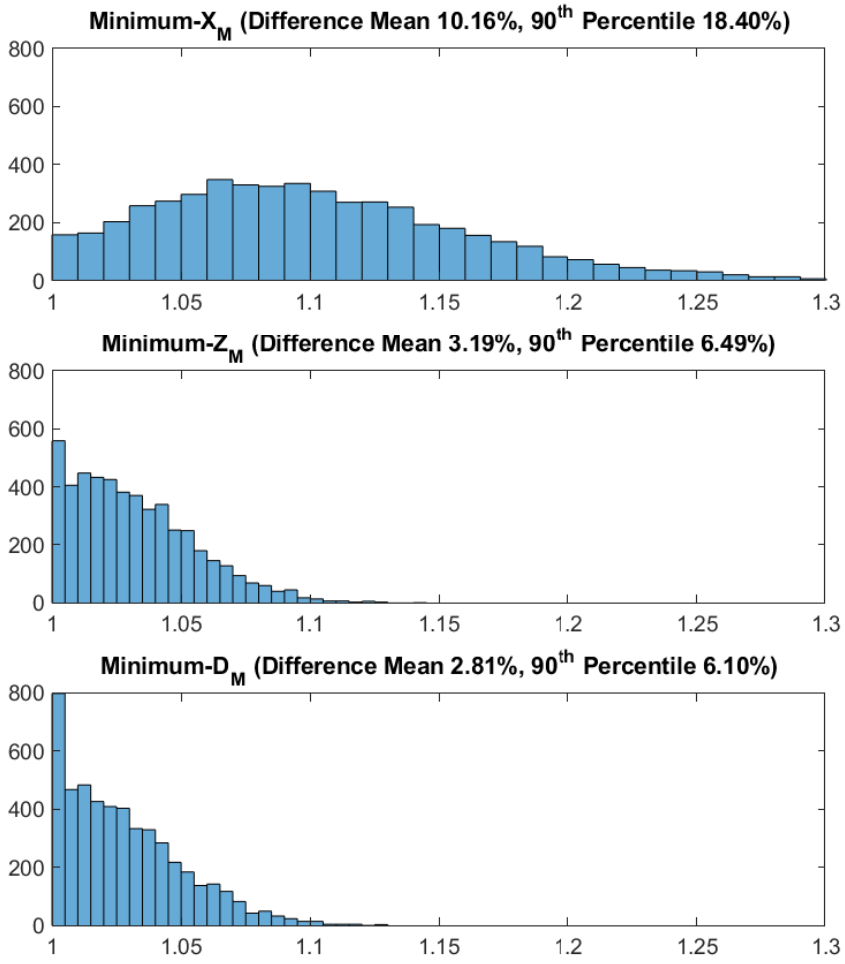

Figure 7.3: Histograms of Ratio of Energy Cost of Baseline Orders (Min-X_M, Z_M, and D_M) over Min-Energy Order for 5000 Randomized Missions, with Varying Number of Waypoints and Ranges

depending on the mission ranges and number of waypoints, with the average and 90$^{\text{th}}$ percentile difference at 1.58%-3.36% and 3.76%-6.55% respectively. These results indicate the significant energy loss when planning the mission just based on distance. Meanwhile, the improvement is more prominent when comparing the minimum-energy order with minimum-X_M and minimum Z_M orders. Specifically, minimizing Z_M results in average increase in energy consumption of 2.72%-4.98%, while minimizing X_M results in average increase of

4.27%-16.25%. Regarding the 3 baseline minimum distance ordering, although minimizing the total distance D_M uses the least energy on average, the performance is not consistent across individual missions. Specifically, minimizing Z_M is more efficient in between 34.8% and 45.6% of missions, and minimizing X_M is more efficient in between 1.6% and 5.3% of missions, again depending on mission parameters.

The key to interpret these results is to account for the stronger impact of vertical motion on energy performance compared with horizontal motion. On one hand, vertical motion contributes primarily to the perpendicular propeller inflow, which has a greater (negative) impact on propeller energy efficiency than planar inflow, as discussed in Chapter 4. On the other, the vertical velocity that can be achieved and sustained by the vehicle is typically lower than that in the horizontal axis. Additionally, while the descending portion of a mission typically reduces energy cost compared with other portion, this reduction is usually outweighed by the increased energy cost of the equivalent climbing portion, which has to be performed during the mission to bring the vehicle back to the origin. As a result, the minimum-energy order tends to have a lower total vertical distance Z_M than the minimum-D_M order. However, the minimum-energy order is typically not exactly the minimum Z_M order, as the tradeoffs between horizontal and vertical motion needs to be balanced reliably.

7.2.2 Analysis of Sample Missions

To further demonstrate and explore key features of the minimum-energy ordering, two sample missions are chosen for discussion. The waypoints of the first mission are specified in Table 7.2, along with the minimum-energy and minimum-distance orders shown in Fig. 7.4.

	A	B	C	D	E	F	G	H
X	-20	20	-12	12	-12	12	-20	20
Y	20	-20	-12	12	12	-12	-20	20
Z	19	19	11	11	-11	-11	-19	-19

Table 7.2: Waypoints of Sample Mission 1

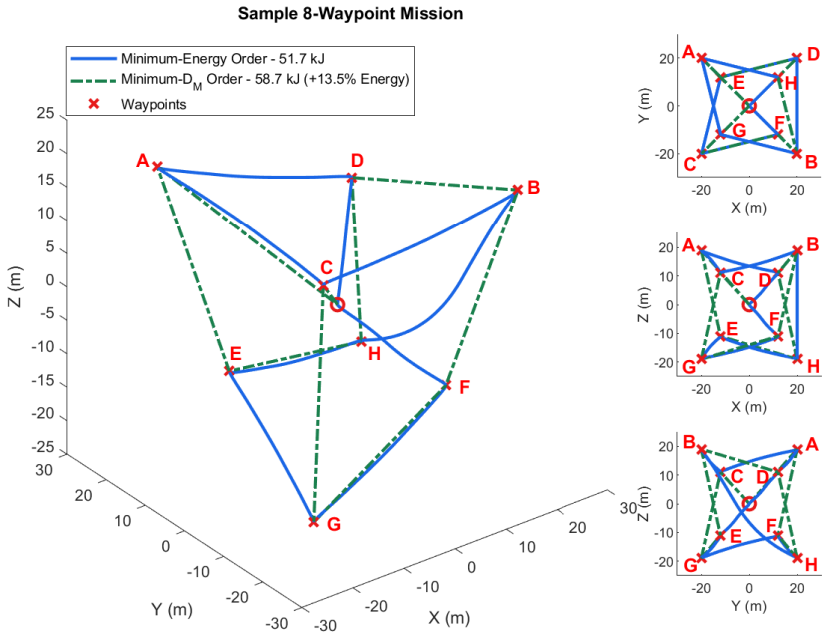

Figure 7.4: Minimum-Energy (Solid) and Minimum-Distance (Dashed) Orders for 8-Waypoint Sample Mission, Including Multiple Viewing Angles.

The energy performance of different ordering approaches is given in Table 7.3. It is seen that when using Fig. 7.2 to predict the optimal energy usage (by interpolation), the minimum-D_M order uses 13.5% more energy than the energy-optimal order for this mission, even though the total distance traveled is 5% shorter (284.4 m versus 299.3 m). Meanwhile, the min-X_M order uses 25.4% more energy, and the min-Z_M order uses either 7.0% or 5.6% more (depending on direction), than the min-energy order, but outperforms the min-D_M order even though the distance traveled is 13% longer (321.4 m versus 284.4 m).

Order	Min-Energy	Min-D_M	Min-X_M	Min-Z_M
Direction	-	Mean (1, 2)	Mean (1, 2)	Mean (1, 2)
Predicted (kJ)	51.7	58.6 (58.6, 58.6)	64.8 (64.8, 64.8)	54.9 (55.3, 54.5)
% Increase	-	+13.5% (+13.5%, +13.5%)	+25.4% (+25.4%, +25.4%)	+6.3% (+7.0%, +5.6%)
PTF (kJ)	39.7	45.8 (45.9, 45.7)	50.2 (51.4, 49.0)	43.1 (43.6, 42.5)
% Increase	-	+15.4% (+15.6%, +15.1%)	+26.6% (+29.6%, +23.5%)	+8.5% (+10.0%, +7.1%)
HVB (kJ)	55.6	70.3 (70.2, 70.3)	86.4 (86.8, 86.0)	56.0 (56.2, 55.9)
% Increase	+40.1%	+77.1% (+76.9%, +77.2%)	+117.7% (+118.6%, +116.8%)	+41.2% (+41.6%, +40.8%)
D_M (m)	299.3	284.4	311.6	321.4
(X_M, Z_M)	(271.9, 108)	(189.5, 174)	(183.2, 240)	(291.3, 76)

Table 7.3: Energy and Distance Metrics of a 8-waypoint Sample Mission under Different Ordering Approaches and Feedback Controllers

Key features of each ordering approach can be analyzed based on this sample mission. First, since vertical motion generally has a stronger (negative) impact on energy consumption than horizontal motion as discussed in Chapter 4.2, the min-energy order tends to have larger X_M but lower Z_M than the min-D_M order, and the min-X_M order performs very poorly. It is seen from Fig. 7.4 that under the min-energy order, the vehicle visits all waypoints on the lower half plane first (Waypoints F, G, E, H), and then proceeds to the top half to minimize the vertical operations. By contrast, the min-D_M order moves up and down repeatedly, and hence contains multiple vertical operations with high energy costs. Second, the min-energy order is also not identical to the min-Z_M order. In fact, the difference in Z_M between the two orders (22 m) is greater than the difference in X_M (19.4 m). This behavior reflects the complexity of the tradeoffs between horizontal and vertical motion, and the need for the physics-based energy consumption computation and optimization to balance the two motions across the waypoints. Specifically, long operations along one axis,

especially the vertical axis, are generally less efficient than diagonal operations with motion along both axes. For example, the vehicle consumes 9.0 kJ to move 50 m along X-axis while climbing 30 m along Z-axis, compared to 8.2 kJ for climbing 30 m alone and 5.8 kJ for moving 50 m forward alone. It is seen that adding horizontal motion to climbing barely increases the energy consumption, while significantly increasing the distance traveled and hence improves the overall energy efficiency. This is because moving long distance along the Z-axis requires a long operation time due to the typical lower vertical velocity limit. Therefore, motion along the other (horizontal) axis can be completed simultaneously under relatively low velocity with minimal additional thrust, and hence only slightly increases the energy consumption. In addition, a low horizontal velocity can also increase propeller efficiency due to the aerodynamic effects, as discussed in Chapter 4.2, partially offsetting the increased thrust required for diagonal motion. These factors have even more significant impacts on the less efficient high-velocity baseline controller, as the HVB controller uses 10.7 kJ for the equivalent diagonal operation, 10.3 kJ for the vertical component, and 6.7 kJ for the horizontal component. Under the minimum-energy order, the vehicle takes advantage of these behaviors by visiting all waypoints below the X-Y plane first, crossing this plane only once and minimizing the number of vertical operations required to complete the mission. Therefore, in this mission, the min-energy order is mostly the same as the min-Z_M order, except that the former commands the vehicle to climb diagonally from point H to point B, while the latter moves vertically to D and then horizontally to B. The energy saving in this motion sequence accounts for most of the advantage of the min-energy order over the min-Z_M order.

For further analysis, a simpler 3-waypoint mission, consisting of the waypoints A, B, and

C at $(0, 40, 25)$, $(40, 0, 25)$, and $(0, 0, 24)$, is shown in Fig. 7.5 for discussion. In this mission, the min-D_M order is the same as the min-X_M and Z_M orders, and, depending on direction of travel, uses either 27.1 or 28.0 kJ of energy, which is 3.9 or 7.5% more than the 26.1 kJ used by the min-energy order. Interestingly, D_M, X_M, and Z_M of the min-D_M order, which are 167.8 m, 136.6 m, and 50 m respectively, are all shorter than those of the min-energy order, which are 174.4, 160, and 52 m respectively. This result, though counterintuitive, is primarily due to the fact that the min-energy order prioritizes diagonal flight with both horizontal and vertical motion. In the min-D_M order, the vehicle climbs purely vertically from the origin to point C, using 8.29 kJ. In the min-energy order instead, it climbs diagonally to point B, using only 0.48 kJ more energy while covering a significant horizontal distance. The vehicle then travels to points C and A in two short horizontal operations before returning to the origin, while the min-D_M order replaces the motion from C to A with a longer operation from B

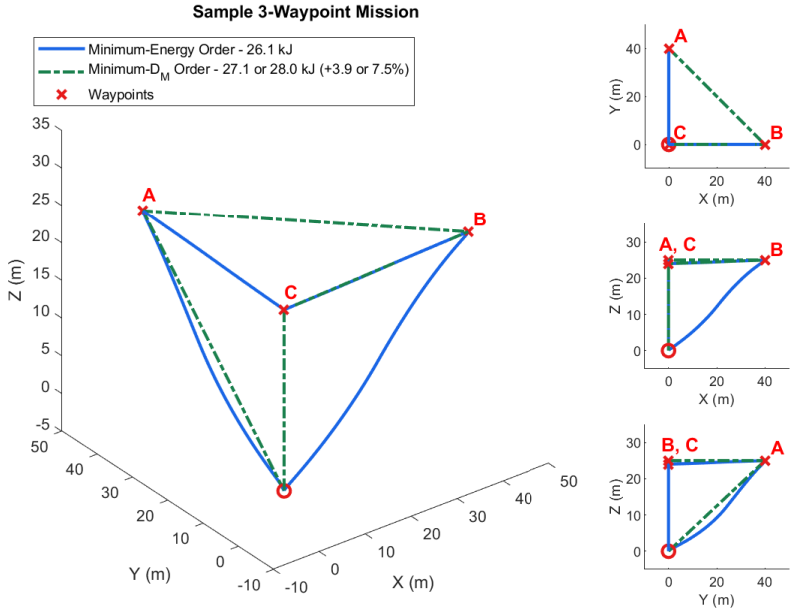

Figure 7.5: Minimum-Energy (Solid) and Minimum-Distance (Dashed) Orders of 3-Waypoint Sample Mission, Including Multiple Viewing Angles.

to A. This longer operation by the min-D_M order uses 1.50 kJ more energy, significantly outweighing the energy saved in the previous climb for a net increase of 1.02 kJ (3.9%) over the min-energy order. Meanwhile, the reverse direction of this min-D_M order uses even more energy, in part because the final descent to O is vertical (from C) rather than diagonal (from A). Interestingly, less energy is needed to descend diagonally to the origin from point A (5.01 kJ) than vertically from point C (5.62 kJ), despite the former operation being longer in distance with an additional horizontal component. To understand this effect, recall that, as discussed in Chapter 4.2, forward motion can improve propeller efficiency by increasing the propeller inflow. During simultaneous descent and forward flight, even though additional thrust is needed for the forward motion, the increase in power consumption is minimal because the propeller thrust-to-power ratio is higher at lower angular velocities (typical of descent flight due to lower thrust demand). Consequently, the improvement in propeller efficiency outweighs the increase in thrust, resulting in a net decrease of energy consumption. Combined with the previously noted energy lost by climbing diagonally rather than vertically, this min-D_M order uses a total of 0.93 kJ (3.5%) more than its reverse, for a total increase of 1.95 kJ (7.5%) relative to the minimum energy order. However, as the direction of travel of a waypoint order has no effect on the distance travelled, the min-D_M order is not able to determine which direction is more efficient, and hence reduce the energy usage.

7.3 Energy Performance Improvement by Combining Optimal Mission Planning with Trajectory Generation and Control

It is also of great interest to examine how much improvement in energy performance can be achieved by combining optimal mission planning with trajectory generation and control, which has been investigated by simulation studies. Specifically, simulations of hundreds of random missions have been performed for various combinations of mission planning approaches (including energy-optimal and minimum-distance ordering) and trajectory/flight controllers (including polynomial trajectory with feedback controller, high velocity baseline controller, and low velocity baseline controller). The performance comparison is summarized in Table 7.4. Note that the relative values for the 3 min-distance orders in this table are given as a percentage increase over the min-energy order, which enables consistent comparison of results across missions. When referenced in the text, some results are presented differently (e.g., min-energy improvement over min-distance) as appropriate.

First, it is seen that the polynomial trajectory following (PTF) controller recovers the majority of the energy saving predicted by the optimization results. Specifically, under PTF, the energy-optimal ordering approach achieves average energy reductions between 1.5% and 2.7% compared to the minimum-distance ordering, which is close to the optimization results shown in Table. 7.1. The slight difference is due in part to the interpolation error of the energy consumption Table in Fig. 7.2. Additionally, each operation in the reference table is simulated starting at hover, while each mission is simulated as a series of operations completed consecutively, with each operation continuing from the end point of the previous operation. As a result, the simulated vehicle may not stop with the exact precision by the

start of the next operation, which can introduce slight disturbances to subsequent operations within the mission, contributing to these errors.

	Energy Cost Increase Relative to Min-E + PTF (%)							
	PTF		HVB			LVB		
N_W	No. of Missions	Min-D_M	No. of Missions	Min-E	Min-D_M	No. of Missions	Min-E	Min-D_M
6	294	+1.49%	194	+39.95%	+46.74%	100	+55.96%	+59.92%
8	388	+2.11%	193	+38.64%	+47.92%	195	+57.19%	+63.66%
10	194	+2.80%	96	+37.79%	+48.35%	98	+59.38%	+67.84%

Table 7.4: Simulation Results of Average Energy Cost Increase over Minimum-Energy Order + Polynomial Trajectory Feedback (PTF) Controller for Combinations of Minimum-Energy/Minimum-D_M Orders + PTF/High-Velocity Baseline (HVB) Controllers for Randomly Generated Missions with Varying N_W and Ranges of $-30m < X < 30m$, $-30m < Y < 30m$, $-25m < Z < 25m$

The most noteworthy results are that, by combining the minimum-energy order and the polynomial trajectory following controller, large energy improvements are achieved over the baseline controllers. Specifically, the PTF controller with minimum-energy ordering achieves energy cost reductions of 31.9%-32.6% and 37.5%-40.4% over the HVB and LVB controllers with minimum-distance ordering. The features of the optimal trajectory and waypoint order discussed in previous chapters contribute to these improvements, although it is noted that the difference between baseline and PTF controllers tend to be larger for complete missions than for the average individual operation shown in Chapter 6.2. This is because, on one hand, most of the operations within the randomly-generated missions include both horizontal and vertical components, which the baseline controllers often fail to balance

efficiently. On the other, because of the range limit of the waypoints, the operations tend to be short relative to the full reference range. The baseline controllers typically perform worse in shorter operations where a larger percentage of the operation is spent accelerating and decelerating, whereas the PTF controller can enable more precise and energy-efficient motion as described in Chapter 5. These short operations also explain why the high-velocity baseline tends to perform better than the low-velocity baseline (using, on average, between 8.2% and 13.5% less energy), due to the sluggish de/acceleration of the latter. The LVB controller typically performs best in long forward cruise operations, but they rarely exist in typical missions. Short operations also mean that the mission tend not to contain flights with large simultaneous descending and forward components, therefore avoiding the area of the reference range where the polynomial fits perform worst relative to the optimized trajectories, as shown in Table 6.1.

Another important finding is that the energy-optimal ordering, although designed based on the PTF controller, could also dramatically reduce the energy consumption of the baseline controllers. Specifically, compared to the minimum-distance order, the minimum-energy order uses between 4.6% and 7.1% less energy with the HVB controller, and between 2.5% and 5.0% less energy with the LVB controller. The differences between the two ordering approaches are in fact larger for the baseline controllers than for the PTF controller, as the inefficiency of the baseline controllers and the minimum-distance ordering approach combine for a greater negative impact than each individually. This finding indicates the importance of mission planning in its own right, and its capability of improving UAV energy efficiency under general flight controllers.

Chapter 8

Summary

8.1 Main Works and Findings

In this dissertation, a multiphysical model is developed and applied to the flight control and mission planning of multirotor uncrewed aerial vehicle with the goal of improving the energy performance. First, the integrated vehicle model, which captures the dynamics of each relevant subsystem, is described. These subsystem dynamics include the aerodynamics of the propeller, the electro-mechanical dynamics of the motor-ESC assembly, the electrical dynamics of the battery, and the rigid-body dynamics of the vehicle. A laboratory test bench is used to parameterize and validate the subsystem models, and flight tests are performed to validate the complete integrated model under real-world experimental conditions. The model demonstrates a high degree of fidelity over a range of operating conditions (including hover, horizontal, climbing, and descending flight), and predicts the thrust generated as well as the power consumption with high accuracy. Specifically, the mean errors between measured and predicted discharge rate, voltage, and thrust were 0.41%, 0.56%, and 2.27% in hover, 0.82%, -0.50%, and 2.9% in vertical flight, and 0.61%, -0.29%, and 3.7% in horizontal flight. The corresponding standard deviations were 0.66%, 0.33%, and 2.50% in hover, 0.89%, 0.32%,

and 2.82% in vertical flight, and 1.34%, 0.36%, and 3.07% in horizontal flight.

The model is then used to analyze specific flight behaviors observed in experimental results, which are key to understanding the overall energy performance of the vehicle. First, the impact of battery dynamics are evaluated using simulated and test bench data. For the octorotor considered in this work, it is shown that propeller RPM, torque and thrust under a given actuation command (motor PWM input) decrease by ∼14%, ∼26%, and ∼26% respectively over the battery operating range. These results demonstrate the power constraints imposed on the vehicle by a depleting battery during flight, which can (and need to be) predicted by the model to avoid non-optimal or unsafe performance. Second, energy efficiency is evaluated for various operating conditions, with each subsystem examined to compare their relative impacts on the overall system efficiency. In particular, the propeller aerodynamics, which are often overlooked or oversimplified in existing works of UAV energy optimization, are found to have a significantly higher impact on overall energy performance than the other subsystems. Specifically, over the range of operating conditions evaluated, the thrust to power ratio varies from 0.101 N/W in hover to a minimum of 0.042 N/W (-58.4%) in climbing flight and a maximum of 0.133 N/W ($+31.7\%$) in descending flight. Finally, an analysis of the energy used per meter travelled, which is a key energy efficiency index in forward cruise, is provided, including identification of the energy-optimal and maximum cruising velocities. The results again demonstrate the vital importance of incorporating propeller aerodynamics for flight control, as failing to consider these dynamics would lead to a significant underprediction of overall energy usage at high velocities, and consequently a significant overprediction of the energy-optimal cruising velocity, resulting in 67.8% increase in energy consumption. The results under a fully-charged (25 V) and near-empty (21 V)

battery are also compared, showing that, while overall energy consumption is fairly similar, low battery energy significantly reduces the maximum cruising velocity ($\sim$11%). This analysis is also repeated under the effects of wind along and against the direction of motion, which is shown to have major impacts on the overall energy consumption.

Next, the model is used to develop an energy-efficient trajectory generation and feedback control framework for waypoint-to-waypoint operations. The results are evaluated relative to a baseline in both simulation and in real-world testing, demonstrating significant performance improvements (on average >10% reduction in energy consumption) in all flight cases. Key behaviors which contribute to these performance improvements are identified and analyzed. In general, it is demonstrated that the model-based approach enables the holistic planning of vehicle behavior along different directions and coordination of multiple vehicle states efficiently over the course of operation. For example, the framework enables the vehicle to supplement active braking with passive deceleration from air resistance, cruise near the energy-optimal velocity, and accelerate more rapidly and efficiently. The framework demonstrates similar average energy savings (10.2%) in experimental testing, despite greater variation due to real-world disturbances and uncertainties, e.g. wind effects, which are also analyzed and discussed in detail based on the experimental results.

In addition, polynomial approximations of the optimized trajectories are developed, enabling rapid and computationally efficient trajectory generation. To characterize these polynomials, optimized trajectories are generated for a range of operations. This reference set is divided into three groups (i.e., primarily forward flight, steep climbing flight, and steep descending flight). Operations in each group are further divided into segments based on key features of the vehicle state trajectories. In both simulations and experimental validation,

these approximations are shown to capture the majority of the energy performance improvements achieved by the optimization, with only a slight 1.3% increase in energy consumption on average despite significantly reduced computational complexity.

Finally, the framework is extended to study the energy-optimal planning of waypoint-based missions. Specifically, the minimum-energy order of traversing a series of waypoints in 3D space is determined and compared to the minimum-distance order as a baseline, over a large number of missions with randomized waypoint locations. It is found that the minimum-energy order differs from the minimum-distance order in majority of the cases, e.g. >95% of 500 missions with 10 waypoints. The difference in energy consumption between the two orders can be as high as 14.9%, with the average at 1.6%-3.3% and 90th percentile at 3.7%-6.5% among missions of varying ranges and number of waypoints. Several features of the minimum-energy order are identified by comparing with the minimum-distance order, and analyzed using two sample missions. For example, it is important to minimize the number and length of vertical flights in a mission due to the negative impact of vertical motion on aerodynamic efficiency. Besides, coupling vertical motion with horizontal motion can significantly promote the vehicle energy efficiency. In the climbing case, adding horizontal motion only slightly adds to the energy consumption while significantly increasing the total distance covered. In the descent case, the effect is even more prominent to the point that additional horizontal motion can actually reduce the energy consumption. These results are explained by correlating to underlying fundamental UAV energy dynamics, especially the impact of motion on the aerodynamic efficiency. It is also shown that, by combining energy-efficient mission planning with the developed trajectory generation and feedback control framework, average energy cost reductions of 37.5%-40.4% are achieved relative to minimum-

distance ordering using the high-velocity baseline controller.

8.2 Recommendations for Future Work

One possible area for expanding this work is to extend the considered hover-to-hover, waypoint-to-waypoint flights to more types of operation. For example, UAV missions could also include waypoints at which the vehicle does not need to stop, and instead maintain some velocity while passing through with reorientation of the attitude. Operations or missions could also be explored under the effect of wind, or with the presence of obstacles the vehicle must avoid. Regarding the energy-optimal trajectory generation for the new types of operation, due to the potential higher complexity of the problem, it may be desirable to explore the use of machine learning methods (e.g. reinforcement learning) to obtain the optimal trajectories as well as their computationally efficient approximation (e.g. through multi-kernel learning [77]).

Additionally, it is noted that the model-based approach investigated in this work allows thorough examination of vehicle behaviors under different scenarios of UAV applications. For example, the model would enable the analysis of the effect of varying vehicle mass on energy dynamics and performance. Changes in vehicle mass are expected in certain emerging applications such as package delivery, which require the vehicle to carry one or multiple variable payloads to one or multiple destinations/waypoints. It is of great interest to investigate how the energy-optimal planning and control should change under the changing mass, including how to determine the optimal forward velocity and associated energy consumption, optimal assignment of payloads to different UAVs, and selection of the optimal routing of delivery.

The flexibility of the model-based approach could also be used to explore applications with constraints not considered in this work. For example, noise constraints are significant limitations for emerging urban applications, including urban air mobility [32]. While acoustics were not included in this work, they could be incorporated into the appropriate subsystem models, which would enable generation of optimized trajectories which take such limitations into account.

Finally, it may be beneficial to improve the modeling of the propeller aerodynamics described in Chapter 2.1.1. Although the model was demonstrated to accurately predict overall energy performance, as discussed in Chapter 4.2, the dynamics of the propeller subsystem vary significantly under variable operating conditions, and it is therefore important to consider potential improvements to this subsystem model. For example, the model assumes that induced velocity is uniform over the propeller disk, which is not the case in all operating conditions, particularly when $v_x \neq 0$. A non-uniform inflow model, such as the Peters-He dynamic inflow model [78], could therefore be included to improve the accuracy of the model. Similarly, the interactions of the propeller flow streams with the vehicle frame, and with that of other propellers, is not fully modeled. While the scaling factors discussed in Appendix 9.3 partially compensate for such effects, a more complete model of these coupled dynamics may provide more accurate results. However, it should also be noted that such improvement in model fidelity may come with the tradeoff of increased complexity. To compensate for this, it may be beneficial to simplify the model in circumstances where computational efficiency is a significant limitation, as was done using lookup tables in Chapter 5.1 and polynomial approximations in Chapter 6. For example, data-driven modeling could be used to streamline prediction of certain energy dynamics or subsystem behaviors, and the order of the model

could be reduced in cases where individual variables add complexity but with minimal benefits. Analysis using the full order vehicle model could be used to identify cases where model complexity can be reduced, as well as to evaluate the performance of the simplified model to ensure the impact on performance is minimized.

References

[1] G. Hoffmann, H. Huang, S. Waslander, and C. Tomlin, "Quadrotor helicopter flight dynamics and control: Theory and experiment," in *AIAA Guidance, Navigation and Control Conference and Exhibit*, 2007.

[2] A. Kasliwal, N. J. Furbush, J. H. Gawron, J. R. McBride, T. J. Wallington, R. D. De Kleine, H. C. Kim, and G. A. Keoleian, "Role of flying cars in sustainable mobility," *Nature communications*, vol. 10, no. 1, p. 1555, 2019.

[3] B. Li, Q. Li, Y. Zeng, Y. Rong, and R. Zhang, "3d trajectory optimization for energy-efficient uav communication: A control design perspective," *IEEE Transactions on Wireless Communications*, pp. 1–1, 2021.

[4] V. Lambey and A. D. Prasad, "A review on air quality measurement using an unmanned aerial vehicle," *Water, Air, & Soil Pollution*, vol. 232, 2021.

[5] W. Liu, M. Sanders, D. Barit, J. Akagi, S. Harding, and S. Tadekawa, "Towards metoc uas for measuring evaporative duct profiles," in *OCEANS 2021: San Diego – Porto*, pp. 1–3, 2021.

[6] L. A. Garrow, B. J. German, and C. E. Leonard, "Urban air mobility: A comprehensive review and comparative analysis with autonomous and electric ground transportation for informing future research," *Transportation Research Part C: Emerging Technologies*, vol. 132, 2021.

[7] N. Polaczyk, E. Trombino, P. Wei, and M. Mitici, "A review of current technology and research in urban on-demand air mobility applications," in *8th Biennial Autonomous VTOL Technical Meeting and 6th Annual Electric VTOL Symposium*, pp. 333–343, 2019.

[8] C. C. Murray and A. G. Chu, "The flying sidekick traveling salesman problem: Optimization of drone-assisted parcel delivery," *Transportation Research Part C: Emerging Technologies*, vol. 54, pp. 86–109, 2015.

[9] A. Goodchild and J. Toy, "Delivery by drone: An evaluation of unmanned aerial vehicle technology in reducing co2 emissions in the delivery service industry," *Transportation Research Part D: Transport and Environment*, vol. 61, pp. 58–67, 2018.

[10] D. L. Hackenberg, "NASA aeronautics research mission directorate (ARMD) UAS and UAM research visions," 2018.

[11] W. L. Fredericks, S. Sripad, G. C. Bower, and V. Viswanathan, "Performance metrics required of next-generation batteries to electrify vertical takeoff and landing (VTOL) aircraft," *ACS Energy Letters*, vol. 3, no. 12, pp. 2989–2994, 2018.

[12] L. Bauersfeld and D. Scaramuzza, "Range, endurance, and optimal speed estimates for multicopters," *IEEE Robotics and Automation Letters*, vol. 7, no. 2, pp. 2953–2960, 2022.

[13] O. Gur and A. Rosen, "Optimizing electric propulsion systems for unmanned aerial vehicles," *Journal of aircraft*, vol. 46, no. 4, pp. 1340–1353, 2009.

[14] K. Karydis and V. Kumar, "Energetics in robotic flight at small scales," *Interface focus*, vol. 7, no. 1, p. 20160088, 2017.

[15] C. Di Franco and G. Buttazzo, "Energy-aware coverage path planning of UAVs," in *2015 IEEE International Conference on Autonomous Robot Systems and Competitions*, pp. 111–117, IEEE, 2015.

[16] F. Morbidi, R. Cano, and D. Lara, "Minimum-energy path generation for a quadrotor UAV," in *2016 IEEE International Conference on Robotics and Automation (ICRA)*, pp. 1492–1498, IEEE, 2016.

[17] J. M. Bradley and E. M. Atkins, "Cyber–physical optimization for unmanned aircraft systems," *Journal of Aerospace Information Systems*, vol. 11, no. 1, pp. 48–60, 2014.

[18] V. Viswanathan, A. H. Epstein, Y.-M. Chiang, E. Takeuchi, M. Bradley, J. Langford, and M. Winter, "The challenges and opportunities of battery-powered flight," *Nature*, vol. 601, pp. 519–525, 01 2022.

[19] N. Kreciglowa, K. Karydis, and V. Kumar, "Energy efficiency of trajectory generation methods for stop-and-go aerial robot navigation," in *2017 International Conference on Unmanned Aircraft Systems (ICUAS)*, pp. 656–662, IEEE, 2017.

[20] T. Han, Q. Hu, and M. Xin, "Three-dimensional approach angle guidance under varying velocity and field-of-view limit without using line-of-sight rate," *IEEE Transactions on Systems, Man, and Cybernetics: Systems*, pp. 1–12, 2022.

[21] A. Tagliabue, X. Wu, and M. W. Mueller, "Model-free online motion adaptation for optimal range and endurance of multicopters," in *2019 International Conference on Robotics and Automation (ICRA)*, pp. 5650–5656, 2019.

[22] X. Wu and M. W. Mueller, "In-flight range optimization of multicopters using multivariable extremum seeking with adaptive step size," in *2020 IEEE/RSJ International Conference on Intelligent Robots and Systems (IROS)*, pp. 1545–1550, IEEE, 2020.

[23] X. Wu, J. Zeng, A. Tagliabue, and M. W. Mueller, "Model-free online motion adaptation for energy efficient flights of multicopters," *CoRR*, vol. abs/2108.03807, 2021.

[24] A. Gong and D. Verstraete, "Experimental testing of electronic speed controllers for uavs," in *53rd AIAA/SAE/ASEE Joint Propulsion Conference*, 07 2017.

[25] A. Gong, R. MacNeill, and D. Verstraete, "Performance testing and modeling of a brushless dc motor, electronic speed controller and propeller for a small uav application," in *2018 Joint Propulsion Conference*, 2018.

[26] C. R. Green and R. A. McDonald, "Modeling and test of the efficiency of electronic speed controllers for brushless dc motors," in *15th AIAA Aviation Technology, Integration, and Operations Conference*, American Institute of Aeronautics and Astronautics, 2015.

[27] Y. Lei, Y. Li, and J. Wang, "Aerodynamic analysis of an orthogonal octorotor uav considering horizontal wind disturbance," *Aerospace*, vol. 10, no. 6, 2023.

[28] Z. Liu, A. Kurzhanskiy, and R. Sengupta, "An energy-based optimal control problem for unmanned aircraft systems flight planning," in *2017 56th Annual Conference of the Society of Instrument and Control Engineers of Japan (SICE)*, pp. 1320–1325, 2017.

[29] X. T. P. She, X. Lin, and H. Lang, "A data-driven power consumption model for electric uavs," in *2020 American Control Conference (ACC)*, pp. 4957–4962, 2020.

[30] Z. Liu, R. Sengupta, and A. Kurzhanskiy, "A power consumption model for multi-rotor small unmanned aircraft systems," in *2017 International Conference on Unmanned Aircraft Systems (ICUAS)*, pp. 310–315, IEEE, 2017.

[31] Z. Liu and R. Sengupta, "An energy-based flight planning system for unmanned traffic management," in *2017 Annual IEEE International Systems Conference (SysCon)*, pp. 1–7, IEEE, 2017.

[32] N. C. Orndorff, D. Sarojini, L. Scotzniovsky, H. Gill, S. Lee, Z. Cheng, S. Zhao, C. Mi, and J. T. Hwang, "Air-taxi transition trajectory optimization with physics-based models," in *AIAA SCITECH 2023 Forum*, 01 2023.

[33] F. Morbidi and D. Pisarski, "Practical and Accurate Generation of Energy-Optimal Trajectories for a Planar Quadrotor," in *IEEE International Conference on Robotics and Automation*, (Xi'an, China), May 2021.

[34] F. Morbidi, D. Bicego, M. Ryll, and A. Franchi, "Energy-efficient trajectory generation for a hexarotor with dual- tilting propellers," in *2018 IEEE/RSJ International Conference on Intelligent Robots and Systems (IROS)*, pp. 6226–6232, 2018.

[35] Y. Fouad, N. Rizoug, O. Bouhali, and M. Hamerlain, "Optimization of energy consumption for quadrotor UAV," in *International Micro Air Vehicle Conference and Flight Competition (IMAV)*, 09 2017.

[36] F. Yacef, N. Rizoug, L. Degaa, and M. Hamerlain, "Energy-efficiency path planning for quadrotor uav under wind conditions," in *2020 7th International Conference on Control, Decision and Information Technologies (CoDIT)*, vol. 1, pp. 1133–1138, 2020.

[37] F. Yacef, N. Rizoug, L. Degaa, O. Bouhali, and M. Hamerlain, "Energy efficiency path planning for a quadrotor aerial vehicle," *Transactions of the Institute of Measurement and Control*, 2021.

[38] M. Podhradskỳ, C. Coopmans, and A. Jensen, "Battery state-of-charge based altitude controller for small, low cost multirotor unmanned aerial vehicles," *Journal of Intelligent & Robotic Systems*, vol. 74, no. 1-2, pp. 193–207, 2014.

[39] R. Schacht-Rodríguez, J.-C. Ponsart, C.-D. García-Beltrán, C.-M. Astorga-Zaragoza, D. Theilliol, and Y. Zhang, "Path planning generation algorithm for a class of uav multirotor based on state of health of lithium polymer battery," *Journal of Intelligent & Robotic Systems*, vol. 91, no. 1, pp. 115–131, 2018.

[40] R. Schacht-Rodríguez, J. C. Ponsart, C. D. García-Beltrán, C. M. Astorga-Zaragoza, and D. Theilliol, "Mission planning strategy for multirotor uav based on flight endurance estimation," in *2019 International Conference on Unmanned Aircraft Systems (ICUAS)*, pp. 778–786, 2019.

[41] Y. Bouzid, Y. Bestaoui, and H. Siguerdidjane, "Quadrotor-uav optimal coverage path planning in cluttered environment with a limited onboard energy," in *2017 IEEE/RSJ International Conference on Intelligent Robots and Systems (IROS)*, pp. 979–984, IEEE, 2017.

[42] M. Wei and V. Isler, "Coverage path planning under the energy constraint," in *2018 IEEE International Conference on Robotics and Automation (ICRA)*, pp. 368–373, IEEE, 2018.

[43] P. Oberlin, S. Rathinam, and S. Darbha, "Today's traveling salesman problem," *Robotics & Automation Magazine, IEEE*, vol. 17, pp. 70 – 77, 01 2011.

[44] Y. Xu and C. Che, "A brief review of the intelligent algorithm for traveling salesman problem in uav route planning," in *2019 IEEE 9th International Conference on Electronics Information and Emergency Communication (ICEIEC)*, pp. 1–7, 2019.

[45] A. Sathyan, N. Boone, and K. Cohen, "Comparison of approximate approaches to solving the travelling salesman problem and its application to uav swarming," *International Journal of Unmanned Systems Engineering.*, vol. 3, no. 1, p. 1, 2015.

[46] N. Mathew, S. L. Smith, and S. L. Waslander, "Planning paths for package delivery in heterogeneous multirobot teams," *IEEE Transactions on Automation Science and Engineering*, vol. 12, no. 4, pp. 1298–1308, 2015.

[47] J. Xie and J. Chen, "Multiregional coverage path planning for multiple energy constrained uavs," *IEEE Transactions on Intelligent Transportation Systems*, vol. 23, no. 10, pp. 17366–17381, 2022.

[48] J. Modares, F. Ghanei, N. Mastronarde, and K. Dantu, "Ub-anc planner: Energy efficient coverage path planning with multiple drones," in *2017 IEEE international conference on robotics and automation (ICRA)*, pp. 6182–6189, IEEE, 2017.

[49] K. Yu, J. M. O'Kane, and P. Tokekar, "Coverage of an environment using energy-constrained unmanned aerial vehicles," in *2019 international conference on robotics and automation (ICRA)*, pp. 3259–3265, IEEE, 2019.

[50] A. S. Prasetia, R.-J. Wai, Y.-L. Wen, and Y.-K. Wang, "Mission-based energy consumption prediction of multirotor uav," *IEEE Access*, vol. 7, pp. 33055–33063, 2019.

[51] J. Diller and Q. Han, "Energy-aware uav path planning with adaptive speed," in *Proceedings of the 2023 International Conference on Autonomous Agents and Multiagent Systems*, AAMAS '23, (Richland, SC), p. 923–931, International Foundation for Autonomous Agents and Multiagent Systems, 2023.

[52] Z. Wu and R. Zhang, "Energy and time-efficient trajectory planning and geometric control for quadrotor waypoints flight," in *2023 9th International Conference on Control, Automation and Robotics (ICCAR)*, pp. 273–278, 2023.

[53] C. Di Franco and G. Buttazzo, "Coverage path planning for uavs photogrammetry with energy and resolution constraints," *Journal of Intelligent & Robotic Systems*, vol. 83, 09 2016.

[54] T. M. Cabreira, P. R. Ferreira, C. D. Franco, and G. C. Buttazzo, "Grid-based coverage path planning with minimum energy over irregular-shaped areas with uavs," in *2019 International Conference on Unmanned Aircraft Systems (ICUAS)*, pp. 758–767, 2019.

[55] T. M. Cabreira, C. D. Franco, P. R. Ferreira, and G. C. Buttazzo, "Energy-aware spiral coverage path planning for uav photogrammetric applications," *IEEE Robotics and Automation Letters*, vol. 3, no. 4, pp. 3662–3668, 2018.

[56] X. Lin, H. E. Perez, S. Mohan, J. B. Siegel, A. G. Stefanopoulou, Y. Ding, and M. P. Castanier, "A lumped-parameter electro-thermal model for cylindrical batteries," *Journal of Power Sources*, vol. 257, pp. 1–11, 2014.

[57] X. Lin, Y. Kim, S. Mohan, J. B. Siegel, and A. G. Stefanopoulou, "Modeling and estimation for advanced battery management," *Annual Review of Control, Robotics, and Autonomous Systems*, vol. 2, pp. 393–426, 2019.

[58] N. Michel, A. K. Sinha, Z. Kong, and X. Lin, "Multiphysical modeling of energy dynamics for multirotor unmanned aerial vehicles," in *2019 International Conference on Unmanned Aircraft Systems (ICUAS)*, pp. 738–747, 2019.

[59] N. Michel, P. Wei, Z. Kong, A. K. Sinha, and X. Lin, "Modeling and validation of electric multirotor unmanned aerial vehicle system energy dynamics," *eTransportation*, vol. 12, p. 100173, 2022.

[60] N. Michel, Z. Kong, and X. Lin, "Optimal control of a multirotor unmanned aerial vehicle based on a multiphysical model," in *Dynamic Systems and Control Conference*, vol. 84287, p. V002T36A004, American Society of Mechanical Engineers, 2020.

[61] N. Michel, P. Wei, Z. Kong, and X. Lin, "Energy-Optimal Unmanned Aerial Vehicles Motion Planning and Control Based on Integrated System Physical Dynamics," *Journal of Dynamic Systems, Measurement, and Control*, vol. 145, p. 041002, 01 2023.

[62] K. Dorling, J. Heinrichs, G. G. Messier, and S. Magierowski, "Vehicle routing problems for drone delivery," *IEEE Transactions on Systems, Man, and Cybernetics: Systems*, vol. 47, no. 1, pp. 70–85, 2016.

[63] N. Michel, Z. Kong, and X. Lin, "Energy-efficient uav trajectory generation based on system-level modeling of multi-physical dynamics," in *American Control Conference*, 2022.

[64] W. Johnson, *Helicopter Theory*. New York, NY: Dover Publications, 1994.

[65] A. P. Thurlbeck and Y. Cao, "Analysis and modeling of uav power system architectures," in *2019 IEEE Transportation Electrification Conference and Expo (ITEC)*, pp. 1–8, IEEE, 2019.

[66] X. Lin, "Theoretical analysis of battery soc estimation errors under sensor bias and variance," *IEEE Transactions on Industrial Electronics*, vol. 65, no. 9, pp. 7138–7148, 2018.

[67] X. Lin, "Analytic analysis of the data-dependent estimation accuracy of battery equivalent circuit dynamics," *IEEE Control Systems Letters*, vol. 1, no. 2, pp. 304–309, 2017.

[68] C. Powers, D. Mellinger, and V. Kumar, *Quadrotor Kinematics and Dynamics*, pp. 307–328. Dordrecht: Springer Netherlands, 2015.

[69] D. Lundström, K. Amadori, and P. Krus, "Validation of models for small scale electric propulsion systems," in *48th AIAA Aerospace Sciences Meeting Including the New Horizons Forum and Aerospace Exposition*, AIAA, 2010.

[70] D. Lawrence and K. Mohseni, "Efficiency analysis for long duration electric mavs," in *Infotech@Aerospace*, AIAA, 2005.

[71] X. Lin, H. E. Perez, J. B. Siegel, A. G. Stefanopoulou, Y. Li, R. D. Anderson, Y. Ding, and M. P. Castanier, "Online parameterization of lumped thermal dynamics in cylindrical lithium ion batteries for core temperature estimation and health monitoring," *IEEE Transactions on Control Systems Technology*, vol. 21, no. 5, pp. 1745–1755, 2013.

[72] X. Lin, H. Fu, H. E. Perez, J. B. Siege, A. G. Stefanopoulou, Y. Ding, and M. P. Castanier, "Parameterization and observability analysis of scalable battery clusters for onboard thermal management," *Oil & Gas Science and Technology–Revue d'IFP Energies nouvelles*, vol. 68, no. 1, pp. 165–178, 2013.

[73] *Series 1580 Test Stand Datasheet*, 2021.

[74] S. Whiteside, N. Zawodny, X. Fei, N. A. Pettingill, M. D. Patterson, and P. Rothhaar, "An exploration of the performance and acoustic characteristics of uav-scale stacked rotor configurations," in *AIAA Scitech 2019 Forum*, AIAA, 2019.

[75] C. Thipyopas, R. Barènes, and J.-M. Moschetta, "Aerodynamic analysis of a multimission short-shrouded coaxial uav: Part ii - translation flight," in *Collection of Technical Papers - AIAA Applied Aerodynamics Conference*, 08 2008.

[76] G. Laporte, "The traveling salesman problem: An overview of exact and approximate algorithms," *European Journal of Operational Research*, vol. 59, no. 2, pp. 231–247, 1992.

[77] M. Gönen and E. Alpaydın, "Multiple kernel learning algorithms," *The Journal of Machine Learning Research*, vol. 12, pp. 2211–2268, 2011.

[78] D. A. Peters and C. J. He, "Finite state induced flow models. ii - three-dimensional rotor disk," *Journal of Aircraft*, vol. 32, no. 2, pp. 323–333, 1995.

Chapter 9

Appendix

9.1 Three-Dimensional Rigid-Body Vehicle Model Equations

To calculate the vehicle (octorotor) motion in three dimensions, the following system of equations is used:

$$
\begin{aligned}
\begin{pmatrix} \dot{X} \\ \dot{Y} \\ \dot{Z} \end{pmatrix} &= \begin{pmatrix} \cos\Theta\cos\Psi & \begin{matrix}\sin\Phi\sin\Theta\cos\Psi \\ -\cos\Phi\sin\Psi\end{matrix} & \begin{matrix}\cos\Phi\sin\Theta\cos\Psi \\ +\sin\Phi\sin\Psi\end{matrix} \\ \cos\Theta\sin\Psi & \begin{matrix}\sin\Phi\sin\Theta\sin\Psi \\ +\cos\Phi\cos\Psi\end{matrix} & \begin{matrix}\cos\Phi\sin\Theta\sin\Psi \\ -\sin\Phi\cos\Psi\end{matrix} \\ -\sin\Theta & \sin\Phi\cos\Theta & \cos\Phi\cos\Theta \end{pmatrix} \begin{pmatrix} \dot{x} \\ \dot{y} \\ \dot{z} \end{pmatrix} \\
\begin{pmatrix} \ddot{x} \\ \ddot{y} \\ \ddot{z} \end{pmatrix} &= \begin{pmatrix} \dot{\Psi}_B\dot{y} - \dot{\Theta}_B\dot{z} \\ \dot{\Theta}_B\dot{z} - \dot{\Psi}_B\dot{x} \\ \dot{\Theta}_B\dot{x} - \dot{\Theta}_B\dot{y} \end{pmatrix} + \frac{1}{m}\begin{pmatrix} \begin{matrix}D_X\cos\Theta\cos\Phi \\ +D_Y\cos\Theta\sin\Psi \\ -mg\sin\Theta\end{matrix} \\ \begin{matrix}D_X(\sin\Phi\sin\Theta\cos\Psi-\cos\Phi\sin\Psi) \\ +D_Y(\sin\Phi\sin\Theta\sin\Psi+\cos\Phi\cos\Psi) \\ -mg\cos\Theta\sin\Phi\end{matrix} \\ \begin{matrix}D_X(\cos\Phi\sin\Theta\cos\Psi+\sin\Phi\sin\Psi) \\ +D_Y(\cos\Phi\sin\Theta\sin\Psi-\sin\Phi\cos\Psi) \\ -mg\cos\Theta\cos\Phi-\Sigma T_j\end{matrix} \end{pmatrix} \\
\begin{pmatrix} \dot{\Phi} \\ \dot{\Theta} \\ \dot{\Psi} \end{pmatrix} &= \begin{pmatrix} 1 & \sin\Phi\tan\Theta & \cos\Phi tan\Theta \\ 0 & \cos\Phi & -\sin\Phi \\ 0 & \frac{\sin\Phi}{\cos\Theta} & \frac{\cos\Phi}{\cos\Theta} \end{pmatrix} \begin{pmatrix} \dot{\Phi}_B \\ \dot{\Theta}_B \\ \dot{\Psi}_B \end{pmatrix} \\
\begin{pmatrix} \ddot{\Phi}_B \\ \ddot{\Theta}_B \\ \ddot{\Psi}_B \end{pmatrix} &= \begin{pmatrix} \frac{J_{Theta}-J_{Psi}}{J_{Phi}}\dot{\Theta}_B\dot{\Psi}_B \\ \frac{J_{Psi}-J_{Phi}}{J_{Theta}}\dot{\Phi}_B\dot{\Psi}_B \\ \frac{J_{Phi}-J_{Theta}}{J_{Psi}}\dot{\Phi}_B\dot{\Theta}_B \end{pmatrix} + \begin{pmatrix} \frac{1}{J_{Phi}}\tau_\Phi \\ \frac{1}{J_{Theta}}\tau_\Theta \\ \frac{1}{J_{Psi}}\tau_\Psi \end{pmatrix}
\end{aligned}
\tag{9.1}
$$

Here, X, Y, and Z are the vehicle positions in the three reference-frame axes, while $\dot{x}$, $\dot{y}$, and $\dot{z}$ are the corresponding velocities in the body-fixed frame. Similarly, Φ, Θ, and Ψ are the vehicle's Euler roll, pitch, and yaw angles, while $\dot{\Phi}_B$, $\dot{\Theta}_B$, and $\dot{\Psi}_B$ are the equivalent angular rates in the body-fix frame. D_X and D_Y are the drag forces in the X and Y axes, while τ_Φ, τ_Θ, and τ_Ψ are the total torques along each rotational axis. These terms are calculated as follows:

$$\begin{aligned}
D_x =& - C_{BD}\dot{x}\sqrt{\dot{x}^2+\dot{y}^2} \\
D_y =& - C_{BD}\dot{y}\sqrt{\dot{x}^2+\dot{y}^2} \\
\tau_\Phi =& (T_7+T_6-T_3-T_8)L\cos(\pi/8)/J \\
&+ (T_5+T_2-T_1-T_4)L\sin(\pi/8)/J \\
\tau_\Theta =& (T_1+T_5-T_2-T_4)L\cos(\pi/8)/J \\
&+ (T_3+T_7-T_6-T_8)L\sin(\pi/8)/J \\
\tau_\Psi =& - T_1-T_2+T_3+T_4 \\
&+ T_5+T_6-T_7-T_8
\end{aligned} \tag{9.2}$$

9.2 Battery Model RC Pair Parameters

The resistance R_k and capacitance C_k values for the battery model, identified as described in Chapter 3.1.3 for the three RC pairs, are given here in Fig. 9.1.

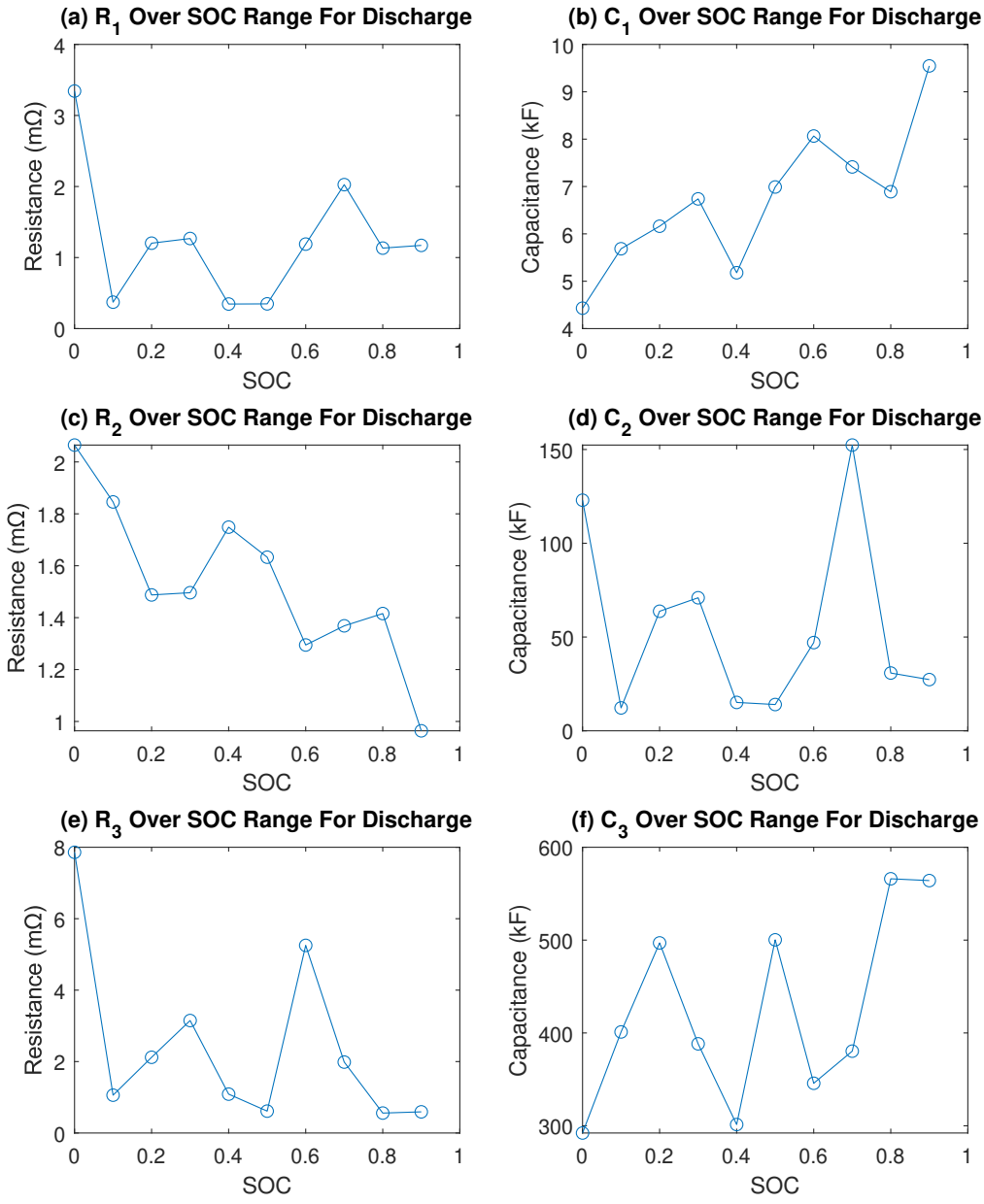

Figure 9.1: Identified (a) R_1, (b) C_1, (c) R_2, (d C_2, (e) R_3, and (f) C_3, versus SOC

9.3 Identification of Inflow Scaling Factors

To obtain the scaling correction factors for v_x and v_z, thrust was predicted for each time step in the experimental data collected in Chapter 3.2.2 using the full model as well as using a version of the model which does not consider propeller inflow. As shown in Fig. 9.2, the errors between the predicted and the measured thrusts were then plotted over the range of vehicle perpendicular velocities, planar velocities, and pitch angles in the data set, with the errors averaged at increments over multiple data points. As shown in Table 3.1, while there is relatively little correlation between thrust error and x-axis velocity, stronger correlations were observed between thrust error and the other two terms, with the no-inflow and full-inflow models having inverse signs in all three cases. Various combinations of scaling factors were tested, and the combination which minimized the root-mean-square thrust error over the full data set was selected.

	z-Axis Velocity	x-Axis Velocity	Θ
No Inflow	0.87	-0.09	0.89
Full Inflow	-0.88	0.2	-0.95
Partial Inflow	0.51	-0.31	-0.12

Table 9.1: Correlation Coefficients for Thrust Prediction Error versus Perpendicular Velocity, Planar Velocity, and Pitch Angle, with Model-Predicted Thrust Calculated under No Inflow, Full Inflow, and Partial Inflow

9.4 Polynomial-Fit Coefficients

In this section, the full equations for the polynomial-fit trajectories described in Chapter 6 are given along with all associated constants. First, the group 1 end time for a given X_f and

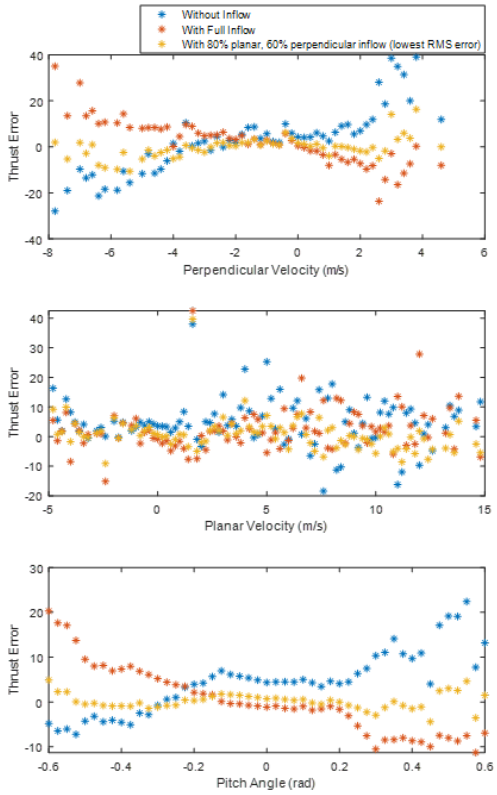

Figure 9.2: Thrust Prediction Error versus Perpendicular Velocity, Planar Velocity, and Pitch Angle, with Model-Predicted Thrust Calculated under No Inflow, Full Inflow, and Partial Inflow

Z_f pair can be calculated as

$$
\begin{aligned}
t_{f,G1} &= (C_{1,t_f}{X_f}^2 + C_{2,t_f}X_f + C_{3,t_f})(C_{4,t_f}{Z_f}^2 + C_{5,t_f}Z_f + C_{6,t_f}) \\
C_{1,t_f} &= 3.57049\times10^{-4}; \quad C_{2,t_f} = 5.85449\times10^{-2}; \quad C_{3,t_f} = 3.05095; \\
C_{4,t_f} &= 2.81828\times10^{-5}; \quad C_{5,t_f} = -2.74942\times10^{-3}; \quad C_{6,t_f} = 1.01356.
\end{aligned}
\tag{9.3}
$$

Recall from Chapter 6.1.1 that an operation is considered part of group 1 if $t_{f,G1}$ is calculated to be greater than $\sqrt{|2Z_f|}$. In this group, the values of time (t_X), forward velocity ($\dot{X}$), and

pitch angle (Θ) at the end of each segment can then be calculated as

$$
\begin{aligned}
t_{1,X,G1} =& 0.1631(X_f - Z_f/2)^{0.5} + 0.5294 \\
t_{2,X,G1} =& 0.03483(X_f - Z_f/2) + 1.210 \\
t_{3,X,G1} =& t_{2,X} + 0.0004470(X_f + 0.35Z_f)^2 + 0.1921 \\
t_{4,X,G1} =& t_f - 0.5487 \\
\dot{X}_{1,G1} =& 0.9000(X_f + Z_f/2)^{0.5} + 2.5170 \\
\dot{X}_{2,G1} =& 0.9893(X_f + Z_f/2)^{0.5} + 3.8678 \\
\dot{X}_{3,G1} =& \min\{0.1039X_f + 5.7009, 9.8581\} \\
\dot{X}_{4,G1} =& 2.0362 \\
\Theta_{1,G1} =& -0.6 \\
\Theta_{2,G1} =& -0.0336(X_f + Z_f/2)^{0.5} - 0.079 \\
\Theta_{3,G1} =& -0.05 \\
\Theta_{4,G1} =& 0.5989.
\end{aligned}
\tag{9.4}
$$

The equivalent terms for the vertical velocity ($\dot{Z}$) segments are calculated as

$$\begin{aligned}
t_{1,Z,G1} =& \max\{0, -0.4557 Z_f/X_f + 0.1588\} \\
t_{2,Z,G1} =& \max\{0, 3.1123 Z_f/X_f + 0.6215, 9.9776 Z_f/X_f - 1.4516\} \\
t_{3,Z,G1} =& 0.7062 |Z_f|^{0.5} + 0.1394 \\
t_{4,Z,G1} =& t_f - 2 \\
\dot{Z}_{1,G1} =& \min\{0, 0.9173 Z_f/X_f - 0.3168\} \\
\dot{Z}_{2,G1} =& \max\{0, 8.4286 Z_f/X_f + 0.2524, 21.6746 Z_f/X_f - 3.6139\} \\
\dot{Z}_{3,G1} =& 1.4115 |Z_f|^{0.5} - 1.3390 \\
\dot{Z}_{4,G1} =& 7.9643 |Z_f/X_f| - 0.2595.
\end{aligned} \tag{9.5}$$

Recall also that some of these terms are constant, either due to the definitions of each segment (i.e. $\Theta_{3,G1}$, as the third segment for Θ in group 1 is defined to end as this term increases above -0.05) or in cases with minimal variation between operations (i.e. $\dot{X}_{4,G1}$, where no significant trend could be identified). For certain other terms, a simple linear relationship is insufficient to accurately describe the observed behavior, and so a piecewise combination of linear expressions and constant limits are used. For example, $\dot{X}_{3,G1}$ is linear with respect to X_f, but is limited to a maximum value of 9.8581 s. The individual values from the optimized results of each reference trajectory used to fit these equations are plotted alongside the equations themselves in Fig. 9.3 for t_X, $\dot{X}$, and Θ, and in Fig. 9.4 for t_Z and $\dot{Z}$.

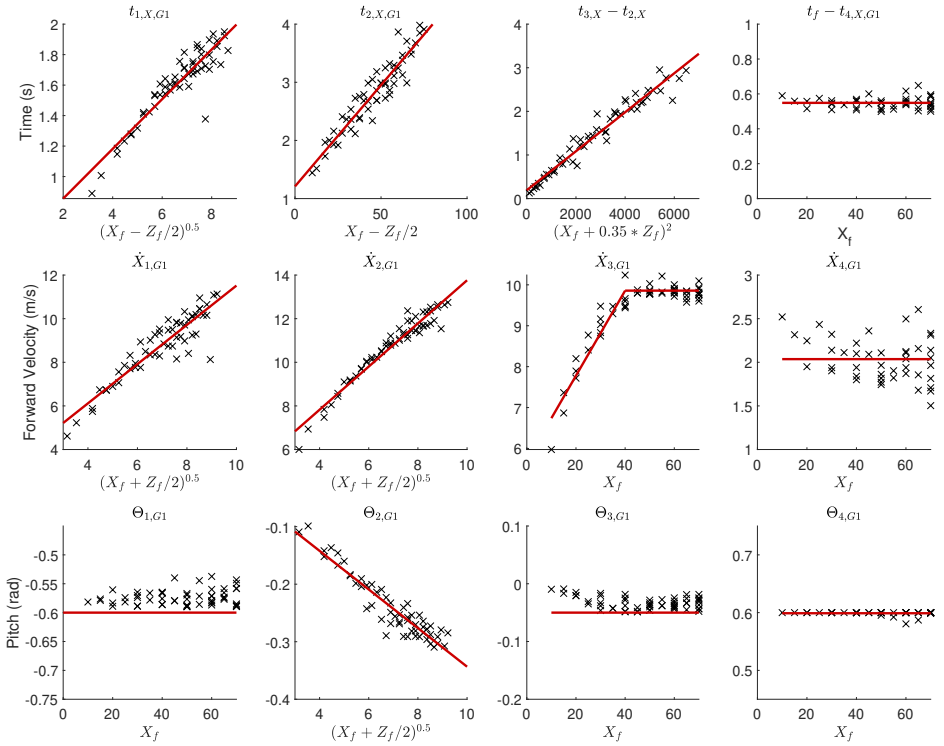

Figure 9.3: Group 1 t_X, $\dot{X}$, and Θ Segment End Values, Including Fitted Equations (Red) and Individual Values from Reference Optimized Trajectories

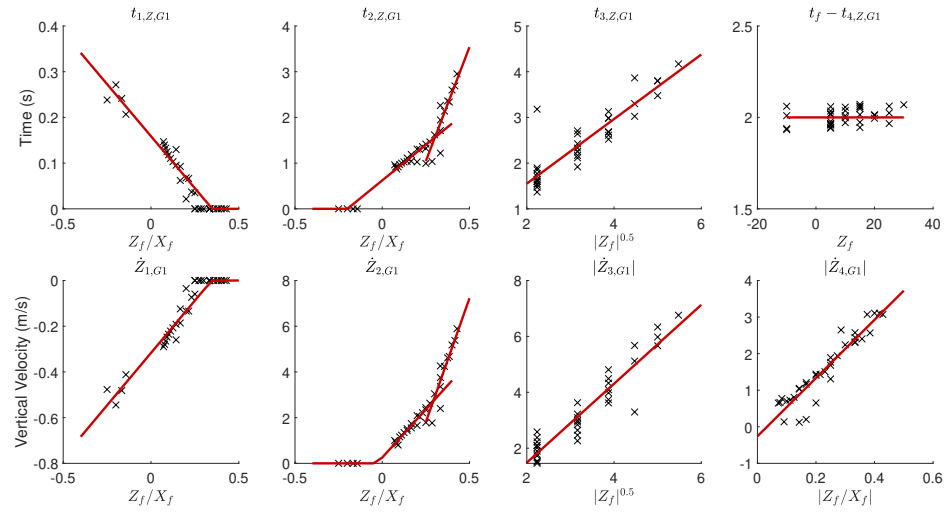

Figure 9.4: Group 1 t_Z and $\dot{Z}$ Segment End Values, Including Fitted Equations (Red) and Individual Values from Reference Optimized Trajectories

Similarly, for groups 2 and 3, the equations for t_X, $\dot{X}$, and Θ at the end of each segment

are given as

$$
\begin{aligned}
t_{1,X,G2} =& \max\{0.0355(X_f - Z_f) + 0.4712, 0.0040(X_f - Z_f) + 0.4976\} \\
t_{2,X,G2} =& 0.8080({X_f}^{0.25} + 0.1{Z_f}^{0.5}) + 0.0502 \\
t_{3,X,G2} =& t_f - 0.1263(X_f/Z_f) - 0.3619 \\
\dot{X}_{1,G2} =& \max\{0.2616(X_f - Z_f) + 1.6597, 0.0362(X_f - Z_f) + 1.6410\} \\
\dot{X}_{2,G2} =& 1.2786(X_f^{0.5}(1 + X_f/Z_f))^{0.75} - 1.2112 \\
\dot{X}_{3,G2} =& 0.4649(X_f/Z_f)^2 + 0.1221 \\
\Theta_{1,G2} =& \max\{-0.6, -0.0131(X_f - 0.4Z_f) - 0.2879\} \\
\Theta_{2,G2} =& -0.0056(X_f^{0.5}(1 + X_f/Z_f))^{1.25} + 0.0305 \\
\Theta_{3,G2} =& \min\{0.6, 0.3236(X_f/Z_f) - 0.0346\}
\end{aligned}
\tag{9.6}
$$

for group 2 and

$$
\begin{aligned}
t_{1,X,G3} =& \min\{1.4, \max\{-0.2131(X_f/Z_f) + 0.2794, -1.9242(X_f/Z_f) - 2.1010\}\} \\
t_{2,X,G3} =& -0.0979Z_f + 1.5011 \\
t_{3,X,G3} =& t_f + 0.1196(X_f/Z_f) - 0.2857 \\
\dot{X}_{1,G3} =& \min\{5.5, \max\{-1.6626(X_f/Z_f) - 0.7813, -9.6982(X_f/Z_f) - 11.8592\}\} \\
\dot{X}_{2,G3} =& \max\{0, -3.1698(X_f/Z_f) + 2.2339\} \\
\dot{X}_{3,G3} =& \max\{0, -1.2129(X_f/Z_f) - 0.4345\} \\
\Theta_{1,G3} =& \min\{0, \max\{0.5423(X_f/Z_f) + 0.1597, -0.6\}\} \\
\Theta_{2,G3} =& -0.0311(X_f/Z_f)^2 - 0.0230 \\
\Theta_{3,G3} =& \max\{0, -0.2962(X_f/Z_f) + 0.0039\}
\end{aligned}
\tag{9.7}
$$

for group 3. Recall that, in these groups, $\dot{Z}$ is simply split into two equal segments, with

vertical acceleration maximized in one and minimized in the other to minimize the time required to reach Z_f. The equations for each of these terms, including the individual values from the optimized results of each reference operation used to fit these equations, are shown in Fig. 9.5 for group 2 and Fig. 9.6 for group 3.

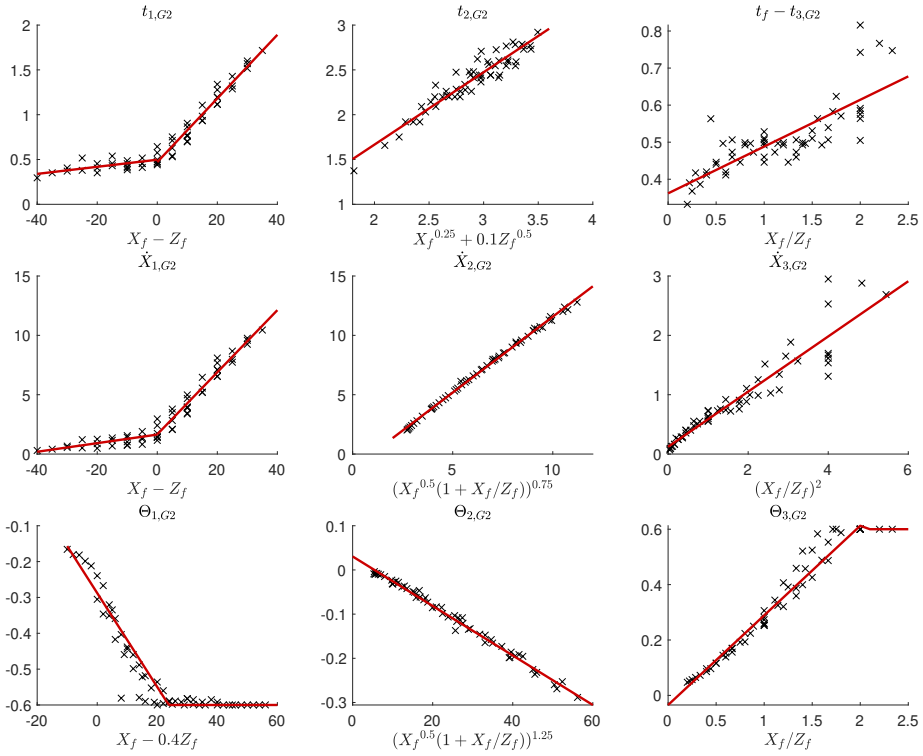

Figure 9.5: Group 2 State Segment End Values, Including Fitted Equations (Red) and Individual Values from Reference Optimized Trajectories

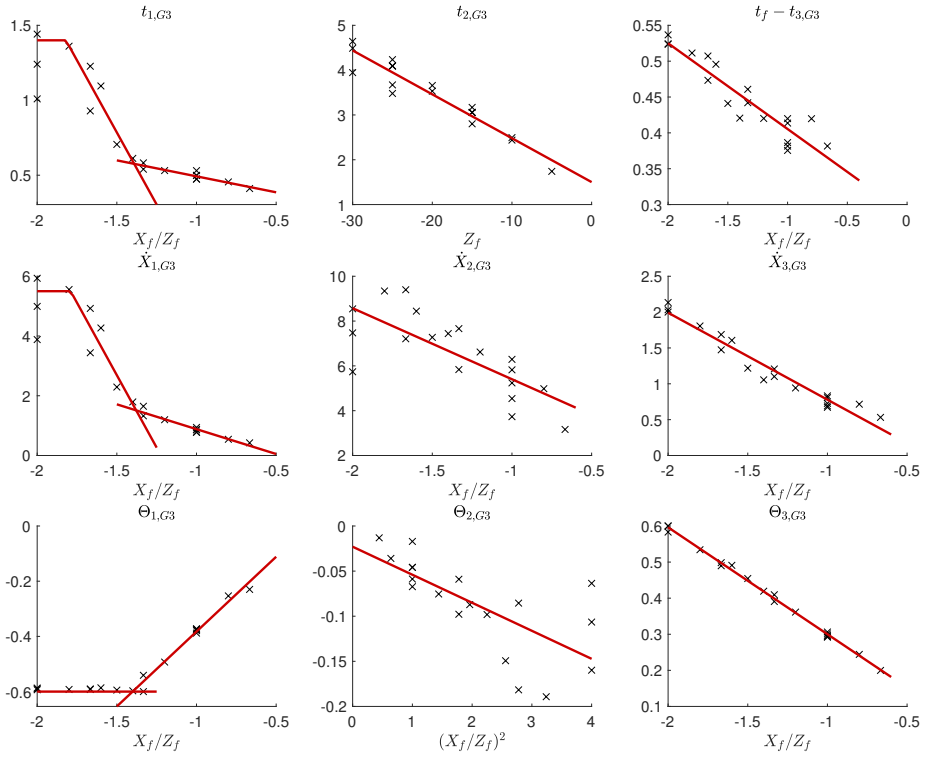

Figure 9.6: Group 3 State Segment End Values, Including Fitted Equations (Red) and Individual Values from Reference Optimized Trajectories (Black)

Polynomial equations are also defined to approximate the states within each segment. These equations are given as

$$\overline{S} = \sum_{n=1}^{7} C_n \bar{t}^{(7-n)}, \tag{9.8}$$

where $\overline{S}$ and $\bar{t}$ are the segment state and time, respectively normalized to $\overline{S} = \bar{t} = 0$ at the start of the segment, and $\overline{S} = \bar{t} = 1$ at the end of the segment. The seven coefficients C_1 through C_7 which define each sixth-order polynomial for the normalized state are given in Tables 9.2 and 9.3, and these equations are plotted alongside the normalized segments from each individual reference operation in Fig. 9.7 for group 1 and in Fig. 9.8 for groups 2 and 3.

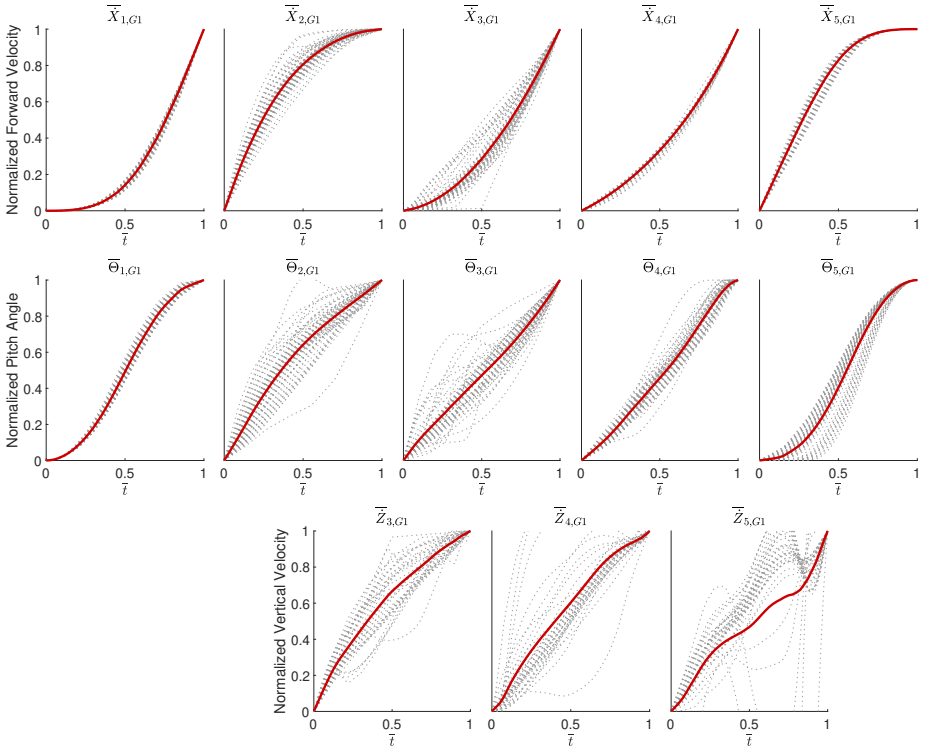

Figure 9.7: Group 1 Normalized State Segments, Including Individual Segments from Reference Optimized Trajectories (Dotted Black Lines) and Fitted Equations (Solid Red Lines)

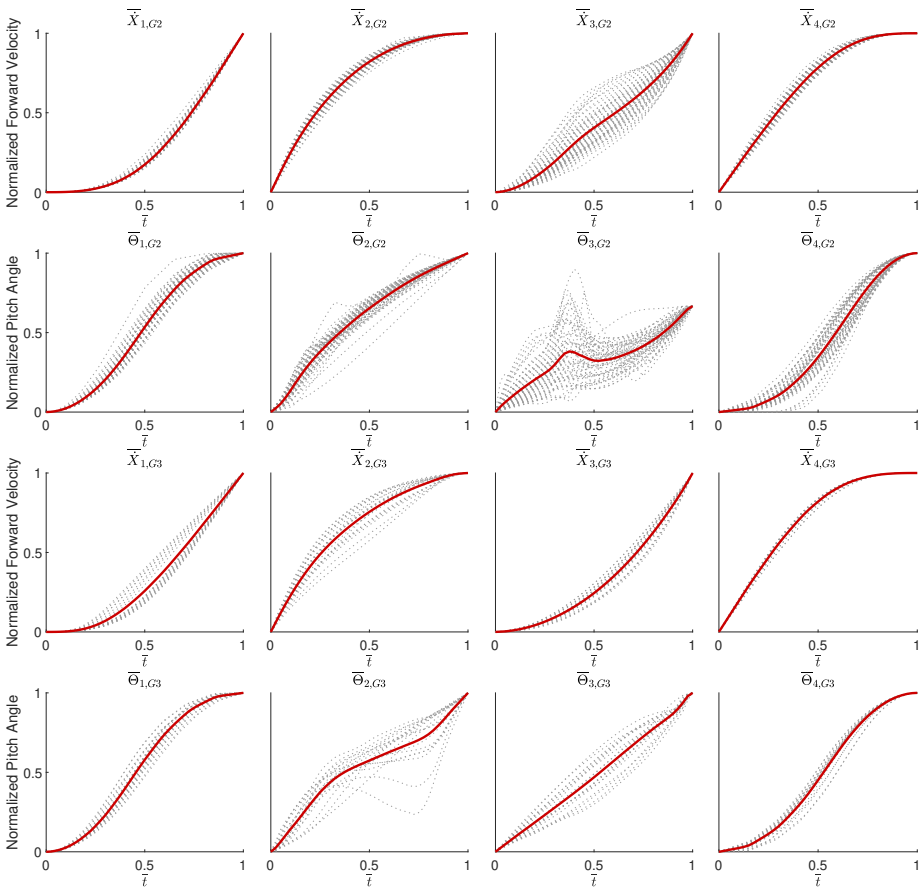

Figure 9.8: Group 2 and Group 3 Normalized State Segments, Including Individual Segments from Reference Optimized Trajectories (Dotted Black Lines) and Fitted Equations (Solid Red Lines)

			C_1	C_2	C_3	C_4	C_5	C_6	C_7
1	$\dot{X}$	1	1.7881	-6.4606	7.2295	-2.0965	0.5776	-0.0385	0.0005
		2	1.1012	-3.6892	4.4504	-1.6263	-1.7921	2.5561	-0.0012
		3	-1.0693	3.3351	-3.8968	2.0202	0.4634	0.1476	0.0002
		4	-0.3593	1.0745	-1.0023	0.4914	0.3705	0.4252	0.0002
		5	-4.2580	13.2709	-13.6797	4.4489	-0.6808	1.8990	-0.0005
	Θ	1	0.0859	4.5814	-11.6585	7.6919	0.1399	0.1612	-0.0020
		2	1.4993	-5.6116	8.6333	-6.3039	1.4017	1.3819	-0.0002
		3	-3.4188	10.6443	-12.6089	7.5627	-2.5002	1.3204	-0.0004
		4	-5.2413	10.6889	-6.2951	0.1132	1.1349	0.5952	0.0022
		5	6.7611	-14.7489	6.9439	1.6440	0.3214	0.0810	0.0003
	$\dot{Z}$	1	0	0	0	0	0	1	0
		2	0	0	0	0	0	1	0
		3	-7.6386	24.2387	-29.7519	18.0730	-6.3520	2.4330	-0.0044
		4	21.7433	-64.8178	71.9480	-36.5378	7.8906	0.7786	-0.0030
		5	29.1783	-83.4763	91.2184	-46.1078	9.6384	0.5729	-0.0010

Table 9.2: Table of Coefficients for Group 1 Normalized State Equations

			C_1	C_2	C_3	C_4	C_5	C_6	C_7
2	$\dot{X}$	1	-2.0082	7.5597	-11.1813	7.3176	-0.7279	0.0401	-0.0003
		2	0.0476	-0.6259	0.4227	1.5019	-2.9338	2.5902	-0.0016
		3	0.9784	-2.7525	3.0487	-1.5555	1.2855	-0.0057	0.0006
		4	-1.7572	5.6315	-5.4502	1.0201	-0.4305	1.9871	-0.0007
	Θ	1	-5.6150	21.5083	-28.9170	14.0373	-0.2150	0.2027	-0.0023
		2	2.6858	-13.7299	25.1964	-19.2120	4.9557	1.1122	-0.0022
		3	5.0671	-12.7897	11.4434	-4.2141	0.5954	0.9045	0.0006
		4	4.3200	-7.6319	0.0287	3.9745	0.1264	0.1847	0.0005
3	$\dot{X}$	1	1.6923	-5.0621	4.2609	-0.1183	0.2387	-0.0112	0.0001
		2	0.4447	-0.9569	0.1583	1.5996	-3.0308	2.7867	-0.0012
		3	-8.0879	22.7936	-20.7083	5.1866	1.7685	0.0438	0.0006
		4	-0.6396	3.0315	-3.8669	1.0075	-0.3236	1.7919	-0.0005
	Θ	1	-1.3543	9.4402	-17.1535	9.8320	0.0566	0.1810	-0.0023
		2	12.6376	-40.2634	48.9982	-27.9088	6.5147	1.0310	-0.0056
		3	1.3406	-22.5016	51.8029	-41.9537	11.8277	0.4504	0.0268
		4	5.7613	-15.5710	11.9479	-2.1608	0.9829	0.0380	0.0017

Table 9.3: Table of Coefficients for Group 2 and Group 3 Normalized State Equations